Dynamic Imaging of Tissue Perfusion Using Ultrasound Contrast Agents

A DISSERTATION
SUBMITTED TO THE FACULTY OF THE GRADUATE SCHOOL
OF THE UNIVERSITY OF MINNESOTA
BY

Juan Du

IN PARTIAL FULFILLMENT OF THE REQUIREMENTS
FOR THE DEGREE OF
Doctor of Philosophy

Dr. Emad S. Ebbini

September, 2016

Acknowledgements

I would like to express my sincere and deepest gratitude to my PhD advisor, Dr. Emad S. Ebbini. During my six-year PhD study, Dr. Ebbini provided me continuous and significant guidance, encouragement and support. Dr. Ebbini helped me successfully transform into a scientist, who is willing to learn and discover, confident to express personal opinions and communicate professionally with peers. My deepest gratitude goes to Dr. Ebbini.

I would also like to thank Dr. Keshab K. Parhi, Dr. Jarvis D. Haupt, Dr. John C. Bischof and Dr. Soheil Mohajer for serving on my defense committee, reviewing my thesis as well as providing helpful comments and feedbacks.

Many thanks to my colleagues, Dr. Dalong Liu, Dr. John Ballard and Dr. Alyona Haritonova for helping me get started in the lab, answering all my questions and inspiring me during my PhD study. My thanks also go to my colleagues Mr. Parker O'Brien, Mr. Brogan McWilliams, Mr. Aditya Karandikar and Mr. Hasan Aldiabat for valuable discussions and help. I would also like to thank my collaborators, Mr. Michael Tradewell and Mr. Daniel Xinran Lu for the sickle cell disease research, data acquisition and helpful discussions. My thanks also go to Dr. Marc D. Schulz, who is always with me and inspiring me during my study.

A special thanks to National Institutes of Health and the University of Minnesota for funding my research.

Last but not least, my deepest appreciation goes to my parents who are always on my side and support me.

Dedication

To my parents and all my mentors

Abstract

Tissue perfusion is an important indicator of the health and vitality of organs such as liver and kidney. Imaging tissue perfusion has significant clinical applications such as myocardial infarction. Contrast-enhanced ultrasound (CEUS) has been clinically used in imaging myocardial perfusion since the 1990s. It was realized, however, that standard B-mode imaging did not have the specificity required to image tissue perfusion in other clinical applications, e.g. tumor perfusion. Microbubble ultrasound contrast agents (UCA) composed of an elastic shell and inert gas content are able to generate nonlinear harmonics. Therefore, nonlinear methods such as harmonic, subharmonic and multipulse imaging were proposed to improve the sensitivity and specificity of perfusion imaging. In this dissertation, a novel method to image the nonlinear response of UCA is investigated by extracting the signal using an adaptive third-order Volterra filter (TVF).

Unlike harmonic and sub-harmonic imaging methods, the TVF separates the linear, quadratic and cubic components from the beamformed pulse-echo data to capture polynomial nonlinearities throughout the system bandwidth. This allows for imaging using broadband pulse transmission to preserve the axial resolution and the signal to noise ratio (SNR). In addition, the quadratic and cubic kernels of the TVF inherently suppress additive Gaussian noise, which lowers the noise floor and improves the detection of UCA activity in low-perfusion regions. Results from *in vitro* and *in vivo* imaging experiments have demonstrated the significance of the advantage of the post-beamforming VF in imaging UCA activity.

Under microflow conditions (as in blood microcirculation), the echogenicity of the UCA microbubbles exhibit temporal dynamics different from the surrounding tissue. For example, the temporal variance of the echogenicity in the presence of UCA is typically higher than that of the same tissue in the absence of UCA. We introduced the temporal perfusion index (TPI) to capture UCA dynamic activity under microflow conditions. The TPI is a spatial measurement that rewards temporal variance at a given image pixel and penalizes the average image intensity over a small spatial mask. An appropriate selection of dynamic range reduces the sensitivity of the TPI to noise and improves the specificity to temporal contrast variations. This approach for finding the "threshold

dynamic range" is extended to account for the breathing motion when the method is applied to *in vivo* data.

The VF and TPI methods were applied to a variety of data sets collected from *in vitro* and *in vivo* imaging targets. These include micro channels embedded in tissue-mimicking phantoms, subcutaneous tumors *in vivo* and brain tissue *in vivo* with and without UCA. The results clearly demonstrate the advantages of the proposed methods in imaging UCA activity under microflow conditions and show the way towards quantitative noninvasive perfusion imaging using pulse-echo ultrasound.

Contents

List of Tables

List of Figures

Chapter 1

Introduction

1.1 Historical Review: Tissue Perfusion Imaging

Tissue perfusion imaging in microvessels has many important clinical applications, such as analyzing and monitoring organ viability and function [1], detecting of tumors and rejected transplanted organs [2], etc. Perfusion is classified as microflow at the capillary or microvessel level and occurs on the scale of 1 - 100μm. Except for optical methods, no imaging modality has inherent specificity to perfusion [3]. However, optical methods are limited by the low penetration depth due to their short wavelength and high attenuation. To bridge the gap, the idea of using contrast agents to improve perfusion imaging quality was introduced.

The earliest forms of contrast agents were radioactive microspheres, which were used to determine the distribution of regional blood flow and measure the distribution of cardiac output and fractional shunting of blood through arteriovenous anastomoses in the early stage [4]. The promise of the method was to determine the blood flow by injecting suitable indicators, such as albumin microspheres, and then measure their distributions with the aid of x-ray.

Contrast-enhanced perfusion imaging has been performed using different imaging modalities, including computed tomography (CT) perfusion imaging [5, 6, 7, 8], xenon CT, computerized axial tomography (CAT), single photon emission CT (SPECT), positron emission tomography (PET) and so on. For all the methods mentioned above, wash-in or wash-out kinetics of exogenously administered diffusible tracers have been

used [1], which leaves patients exposed to large doses of radiation.

Magnetic resonance (MR) is another important imaging modality. MR perfusion imaging is an emerging tool in assessing regional cerebral hemodynamics and has the potential for diagnosing and treating of cerebrovascular disease, neoplasms and other disorders [9]. MR perfusion has high imaging resolution, but it requires the intravenous (IV) injection of gadolinium-based contrast agents [10]. In [1], Detre *et al* proposed to use ^1H NMR imaging to generate perfusion maps noninvasively in the rat brain. This technique was later developed as Arterial spin-labeled (ASL) perfusion MRI [11]. ASL does not require contrast injection or inhalation and has clinical applications such as the diagnosis of stroke, cerebrovascular disease, brain tumor, etc. However, MR perfusion technology is still limited by its high cost and slow data acquisition.

Compared to the methods mentioned above, ultrasound is a real-time imaging modality with low cost, safe and easy operation, and a good depth of penetration. Microbubble ultrasound contrast agents (UCA) are commonly used to improve the microvessel perfusion imaging due to their nonlinear oscillation and capability of generating harmonic energy [12]. Microbubble UCAs and current ultrasound perfusion imaging methods and challenges will be introduced next.

1.2 Ultrasound Contrast Agents: Current Research and Challenges on Perfusion Imaging

In this section, we will detail different aspects of UCA, the state of the art and common challenges in contrast-enhanced perfusion imaging to be addressed by the thesis research.

1.2.1 Microbubble Ultrasound Contrast Agents

Microbubble UCAs offer a significant promise in a variety of diagnostic and therapeutic applications [13, 14, 15, 16, 17, 18]. Microbubbles are composed of a shell (Albumin, Lipid, polymers, etc.) and gas content (air, Perfluorocarbon, Nitrogen, etc.) [19]. Because of the high acoustic impedance mismatch between the microbubble itself and the surrounding tissue, microbubbles can be used to improve perfusion imaging quality. Contrast-enhanced ultrasound (CEUS) has been clinically used since the 1990s, though,

it was realized early on that standard B-mode imaging does not have the specificity required to image perfusion [12]. The dominant nature of the echoes from the surrounding tissue relative to the UCA echo components represents a major challenge for realizing high-specificity perfusion imaging. Later on it was recognized that gas-filled microbubbles were efficient nonlinear resonators capable of generating strong harmonic response relative to tissue. Therefore, microbubble nonlinear behavior has been widely studied both theoretically and experimentally. One classic model of microbubble oscillation is given as the Rayleigh-Plesset equation [20]. The model was simplified under the condition that the bubble was dissolved in an incompressible liquid. Later in [21], the developed model was presented based on the modified Herring equation,

$$\rho_l(R\ddot{R} + \frac{3}{2}\dot{R}) = P + \frac{R}{c}\dot{P} - (P_o + P(t)), \tag{1.1}$$

where, c is the speed of sound, ρ_l is the surrounding liquid equilibrium, R is microbubble instantaneous radius, and $\dot{R}$ and $\ddot{R}$ are the first and second time derivatives of R. The pressures P_o and $P(t)$ are the liquid hydrostatic pressure and the driving acoustic pressure, respectively. In [22], the acoustic model with microbubble UCA was simulated using the Field II program. The feasibility of separating linear and nonlinear components using a Volterra filter was validated by analyzing UCA backscattered echoes.

1.2.2 Current Ultrasound Perfusion Imaging Methods and Challenges

The nonlinear response of the microbubbles plays an important role in determining the sensitivity and the specificity in perfusion imaging. This led to the development of several harmonic imaging methods with transmit-pulse shaping and echo-filtering strategies designed to:

- Minimize the transmit energy components outside the fundamental band.
- Achieve maximum suppression of the fundamental band from the received echo components.

Several harmonic imaging methods exploiting the nonlinear oscillations of microbubbles, together with the use of low mechanical index (MI) to minimize tissue nonlinearity, have been developed [23, 24, 25]. These methods include (second) harmonic imaging, subharmonic imaging (SHI), and multipulse imaging.

Second harmonic imaging has shown better clutter rejection and transmit focusing but worse signal-to-noise-ratio (SNR) as compared to that achieved with fundamental imaging [26]. Haider *et al* [26] proposed using higher harmonic components to improve SNR and preserve tissue information. Odd order components exhibited better performance due to spectral folding. Compared to harmonic imaging, SHI shows better lateral resolution when imaging deep-lying structures [27]. However, the implementation of SHI is limited by the requirement for narrow-band insonation signals to achieve good harmonic separation [28, 29].

Multipulse is another way to capture UCA nonlinearity. One multipulse approach is amplitude modulation (AM) proposed in [30], and later extended to phase and amplitude modulation [26] which can increase the SNR and sensitivity to UCA activities. Another multipulse method is pulse inversion (PI) which was introduced in [31]. Later, a combined PI and AM (PIAM) approach was proposed in [32] to improve the preservation of harmonic signals. More recently, the PI Doppler method has been demonstrated using high-speed plane-wave imaging [33]. This approach enables the simultaneous imaging of perfusion and flow, which addresses an important clinical limitation of previously proposed UCA perfusion imaging methods.

Multipulse Methods: Advantages and Limitations: Multipulse methods such as PI are perfusion imaging methods which are familiar to the medical ultrasound community. The principle of PI is to transmit two pulses with opposite polarity and then sum the echoes from these two transmissions. One advantage of this scheme is the absence of limitation in transmitting bandwidth. An illustration of the PI principle is shown in Figure 1.1. The idea is to cancel out linear components while preserving even harmonics.

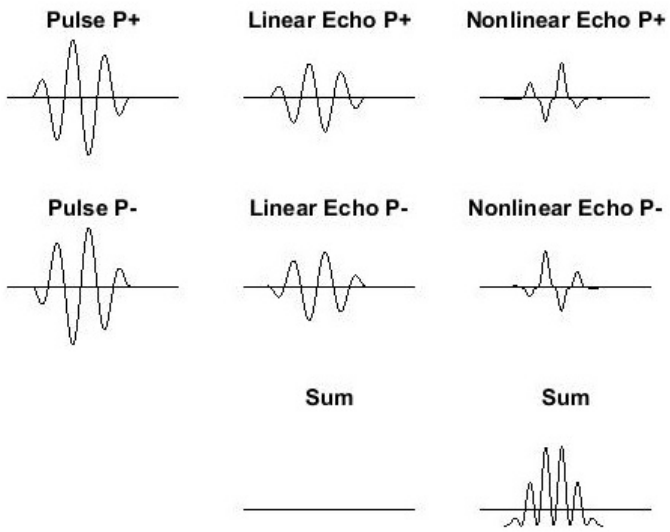

Figure 1.1: An illustration of the pulse inversion principle.

It was recognized that multipulse methods require multiple pulse transmissions for acquisition of each image line. For example, PI requires one positive and one negative pulse to acquire an image line. Consequently, this requirement reduces the frame rate. In addition, there are some other limitations:

First, PI has a limitation on imaging spatial specificity. In [34], the spatial extent of the UCA channel in both axial and lateral directions was $\geq$ 1mm, while the UCA microflow was confined within the 200μm cellulose tube during the experiment. Meanwhile, the PI image exhibited much larger spatial extent than the RF B-mode image, especially in the axial direction.

Second, a large residual tissue component may be retained [35, 36]. PI relies on perfect cancellation between successive positive and negative pulses. This condition can be achieved near the focal zone. However, in the region away from focus beams perfect cancellation cannot be fulfilled due to the side lobes, grating lobes, etc, thus resulting in residual tissue component.

1.3 Ultrasound Imaging Systems

Pulse-echo Ultrasound and Beamforming: In general, diagnostic ultrasound transducers adopt the pulse-echo technique for imaging. The principle is to image and diagnose the region to be studied by sending short ultrasound pulses and capturing their reflections. The axial depth of the reflector z_i is identified as

$$z_i = \frac{c\tau_i}{2}, \tag{1.2}$$

where c is the speed of sound and τ_i is the delay between the transmission of the pulse and the reception of the echo. Equation 1.2 assumes a homogeneous medium and constant propagation speed in the medium.

Figure 1.2 provides a schematic of a 2D linear array system model. The x-z (lateral and axial) image plane uses the Cartesian coordinate system. Each image line, which is referred to as an A-line, is formed by beamforming of the backscattered echoes received by N sub-elements. The standard beamforming method for image reconstruction is delay-and-sum beamforming [37].

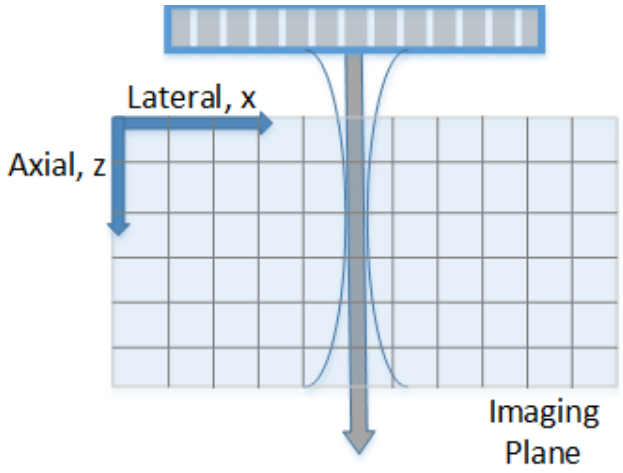

Figure 1.2: A schematic of a 2D linear array system model.

Synthetic Aperture Beamforming: The DMUA adopts a synthetic aperture (SA) beamforming method. The idea of SA imaging is to excite one transmit element each time and receive echoes by all elements in order to provide uniform excitation and high

quality images. The image intensity at pixel $P(x_p, z_p)$ can be expressed as [38]

$$I(x_p, z_p) = \sum_{i=1}^{N} \sum_{j=1}^{N} A_i \cdot B_j \cdot s_{i,j} \cdot \frac{R_{ip} + R_{jp}}{c} \cdot D(\theta_i) \cdot D(\theta_j), \tag{1.3}$$

where A_i and B_j are the transmit and receive apodization weights, respectively. R_{ip} and R_{jp} are the distances between the pixel P and transmitting element i and receiving element j. The parameter $s_{i,j}$ is the echo received by this pair of transmitting and receiving elements. N is the total number of array elements, which is 32 used for experiments presented in this dissertation. $D(\theta)$ is the element directivity weighting function which is given as

$$D(\theta) = \frac{\sin[kd\sin(\theta)/2]}{kd\sin(\theta)/2}, \tag{1.4}$$

where $k = \dfrac{2\pi}{\lambda}$, λ is the wavelength, d is the element width, and θ is the angle between the vector from the element to the pixel $P(x_p, z_p)$.

Two different ultrasound imaging systems were used to acquire the echo data presented in this dissertation. They are briefly described in this section.

1.3.1 Sonix RP with Clinical Linear Transducers

The Sonix RP (Ultrasonix, Richmond, BC Canada) was used for collecting the RF data through its research interface. The sampling frequency was 40 MHz. The data sets were collected while the system was in the research mode. The transmitter settings were fixed in the clinical mode and they were not changed during acquisition.

Two clinical linear transducers were used: LA14-5/38 and HST15-8/20, both having 128 elements. LA14-5/38 had a frequency range of 5-14 MHz with a center frequency of 7.2MHz. Its main applications include abdominal, musculoskeletal and pediatric imaging. HST15-8/20 had a frequency range of 8-15 MHz with a center frequency of 10MHz. Its main applications include pediatric and peripheral vascular imaging.

The imaging pulses used were standard for the linear probe designed to cover the full bandwidth. No special pulses with shifted center frequency were used to excite the microbubbles in harmonic or subharmonic modes. In some cases, pulse inversion mode was acquired for comparison purposes.

1.3.2 Dual-mode Ultrasound Array and Its Imaging System

The idea of a dual-mode ultrasound array (DMUA) was proposed in [38]. The array, designed for image-guided surgery, is able to perform both ultrasound imaging and therapy. An example DMUA prototype is shown in Figure 1.3. It has 64 elements, composed of two rows on a spherical surface with a radius of curvature of 40 mm. The center frequency is approximately 3.5 MHz. Real-time DMUA imaging is performed on a GPU-based platform. More details on the DMUA imaging system can be found in [39].

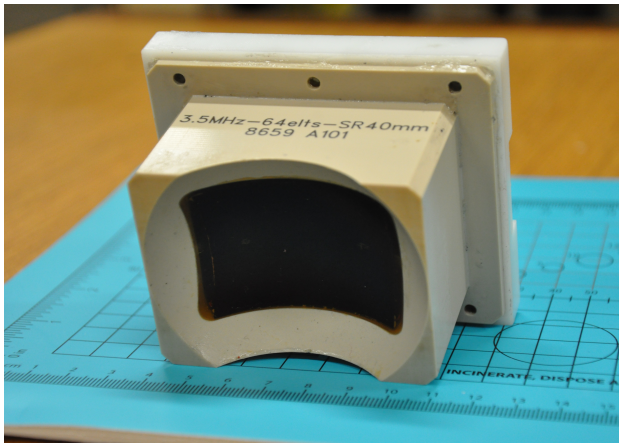

Figure 1.3: An image of the dual-mode ultrasound array (DMUA).

1.4 Contributions

This dissertation is based on two main contributions. First, the advantages of using the Volterra filter (VF) in terms of improved spatial specificity and contrast-to-tissue ratio (CTR) has been experimentally demonstrated. Second, the concept of temporal perfusion index (TPI) has been brought in to qualitatively measure the perfusion density by accounting for UCA dynamics due to pulsation and blood circulation.

Volterra Filters

Volterra filters are adopted to improve UCA imaging quality by capturing UCA nonlinearity. The concept of post-beamforming nonlinear filtering of ultrasound echo data for

separating the linear and nonlinear components using the Volterra filter is introduced. This can be achieved without the need for multipulse transmissions, which addresses the motion sensitivity problem. Furthermore, it does not require bandlimiting the transmit pulses to simplify the separation of the linear and nonlinear components [40]. The VF can therefore be designed to extract nonlinear echo components (e.g. quadratic, cubic, etc.) throughout the spectrum of the echo data, not just at the expected bands (such as 2nd harmonic, subharmonics, or ultraharmonics). This allows for the use of standard imaging pulses designed to provide the best possible resolution and SNR in the fundamental (B-)mode by utilizing the full bandwidth of the imaging probe.

Experimentally, *in vitro* quadratic and cubic images, referred to as QB-mode and CB-mode, produced higher mean CTR values than B-mode, which showed improved sensitivity. Compared to PI they produced similar or higher mean CTR values with greater spatial specificity. *In vivo* results from imaging UCA activity in an implanted LNCaP tumor with heterogeneous perfusion were reported. The *in vivo* measurements behaved consistently with the corresponding calculations obtained under microflow conditions *in vitro*. Specifically, the nonlinear VF components produced larger increases in the temporal mean and standard deviation values compared to B-mode in regions with low to relatively high perfusion. These results showed that polynomial filters such as the VF can provide an important tool for imaging UCA activity in regions with heterogeneous perfusion.

Temporal Perfusion Index

Temporal perfusion index (TPI) is introduced to improve UCA perfusion imaging quality by accounting for different "UCA events" due to pulsation and blood circulation. Microbubbles entering and leaving the imaging slice represent an independent UCA event. The TPI is a spatial measurement which rewards temporal variance at a given image pixel and penalizes the average image intensity in the neighborhood of the pixel. It utilizes UCA dynamic activity to preserve UCA signals while eliminating the effect of tissue/breathing motion. It is capable of separating UCA activity from surrounding tissue and high specular reflectors, resulting in high-quality perfusion imaging. The TPI can be extended to motion-triggered TPI, by taking the animal's breathing motion into consideration.

Experimentally, TPI values computed using both *in vitro* and *in vivo* data showed sensitivity and specificity to perfusion imaging. *In vitro* results from imaging UCA activity in 200μm microflow channels with different UCA concentrations were reported. The results demonstrated that the TPI is capable of providing a qualitatively measure of perfusion density. The *in vivo* transcranial data behaved consistently with the results obtained under microflow conditions *in vitro*. Motion-triggered TPI was applied to *in vivo* transcranial data with pronounced breathing motion present and the results showed that it can further suppress the tissue motion by accounting for the animal's breathing motion.

1.5 Organizations of this Thesis

In addition to this introductory chapter, the dissertation is organized into the following chapters:

- Chapter 2 introduces the FIR third-order Volterra filter (TVF) as a post-beamforming method for separating linear and nonlinear components. The adaptive recursive least squares (RLS) algorithm is adopted to derive the filter coefficients. The differences of quadratic kernels derived by a second-order and a third-order Volterra filter will be discussed.

- Chapter 3 defines temporal perfusion index (TPI) as a dynamic statistical method to qualitatively measure perfusion density. The dynamic range to compute TPI is determined by the variation of probability distribution function over frames. Motion-triggered TPI is introduced by accounting for the animal's breathing motion.

- Chapter 4 presents results of various fundamental *in vitro* validation studies. Firstly, spatial and temporal characterization of microflow using TVF and TPI is provided. The data were acquired from 200μm cellulose tube(s) embedded in tissue-mimicking phantoms. Secondly, a spatial heterogeneous perfusion and flow imaging study is presented. The data were acquired from a 6mm flow channel embedded in a tissue-mimicking phantom. In the end, two preliminary studies

on combined flow and microflow imaging, and longitudinal perfusion imaging are briefly introduced.

- Chapter 5 provides the results of *in vivo* heterogeneous tumor perfusion imaging, which is one of the most significant applications. Heterogeneous tumor perfusion imaging employing TVF and TPI is performed using a clinical linear transducer. The results demonstrate high resolution imaging of tumor perfusion over a high dynamic range using standard diagnostic probes and clinically-relevant concentrations of UCA.

- Chapter 6 is focused on transcranial perfusion imaging with the presence of the skull using the DMUA. Firstly, an *in vitro* validation study on microflow perfusion imaging is provided. The data were acquired from 200μm cellulose channels embedded in a tissue-mimicking phantom with a rat's skull present. Following that, the results of two *in vivo* experiments are presented, without and with accounting for animal's breathing motion.

- Chapter 7 provides a preliminary study on perfusion imaging using a 15μm microchannel embedded in a micro-fluid device, which was used to mimic sickle cell disease environment. The study demonstrates the potential to diagnose and treat SCD using ultrasound and UCA.

- Chapter 8 draws conclusions and gives suggestions for future studies.

Chapter 2

Volterra Filters

2.0 Introduction

Ultrasound perfusion imaging relies on nonlinear responses of microbubble contrast agents to improve the imaging specificity and sensitivity. Nonlinear filters are therefore required as a post-beamforming method for separating linear and nonlinear components of the ultrasound backscattered signal.

Volterra filters (VFs) are adopted to capture the microbubbles' nonlinearity. VFs can model a large class of nonlinear systems and are capable of capturing nonlinear signals. Another advantage is that VFs can be structured linearly to simplify their implementation.

2.1 System Model

2.1.1 Volterra Filters

The VF is one of the most commonly used nonlinear filters [41, 42]. It is a polynomial filter with either finite or infinite memory. The discrete P-order VF, for example, can be implemented by the following finite-memory difference equation:

$$\hat{x}[n+1] = \nu[n] + \sum_{p=0}^{P-1} \sum_{k_0=0}^{m-1} \sum_{k_1=0}^{m-1} \cdots \sum_{k_{p-1}=0}^{m-1} h_p[k_0, k_1, \ldots, k_{p-1}] \prod_{j=0}^{p-1} x[n-k_j] \tag{2.1}$$

where $x[n]$ is the input signal, such as beamformed RF data in pulse-echo ultrasound. The kernels, $h_p[k_0, k_1, \ldots, k_{p-1}]$ operate on the polynomial products of the input data $x[n]$ to extract the p-order components. The residual component $\nu[n]$ accounts for noise and higher-order nonlinearities which are not accounted for by the filter. The parameter m represents the system memory.

In our application, the order of nonlinearity (such as quadratic, cubic, quartic, etc.) should be chosen to match the expected nonlinearity of the echo data. For the low-MI imaging scenarios of interest in modern ultrasound imaging, third-order VFs (TVF) are sufficient. A TVF filter can be implemented as follows:

$$\begin{aligned}\hat{x}[n+1] = \nu[n] &+ \sum_{k_0=0}^{m-1} h_L[k_0]x[n-k_0] + \sum_{k_0=0}^{m-1}\sum_{k_1=0}^{m-1} h_Q[k_0,k_1]x[n-k_0]x[n-k_1] \\ &+ \sum_{k_0=0}^{m-1}\sum_{k_1=0}^{m-1}\sum_{k_2=0}^{m-1} h_C[k_0,k_1,k_2]x[n-k_0]x[n-k_1]x[n-k_2] \\ &= \nu[n] + x_L[n] + x_Q[n] + x_C[n]\end{aligned} \tag{2.2}$$

where the kernels $h_L[k_0]$, $h_Q[k_0, k_1]$, and $h_C[k_0, k_1, k_2]$ operate on the polynomial products of the input data $x[n]$ to extract the linear, quadratic, and cubic components, respectively. The output signals represent the linear, $x_L[n]$, quadratic, $x_Q[n]$ and cubic, $x_C[n]$.

The signal decomposition operation of a TVF is schematically represented in Figure 2.1.

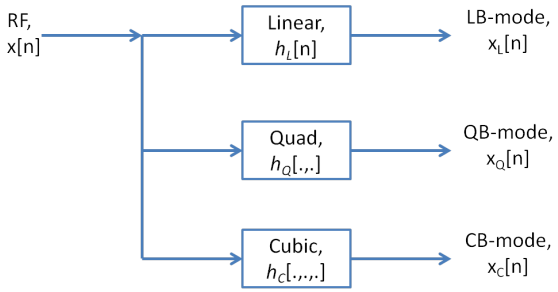

Figure 2.1: A schematic representation of signal decomposition using a TVF.

The TVF decomposition shown in Equation 2.2 offers several advantages in signal processing. First, it can be implemented readily in a much similar manner as a

finite-impulse response (FIR) filter. In fact, the linear component, x_L, is the standard convolution with a 1D FIR filter kernel of length m. The higher order components represent a special form of "polynomial" convolution that extract quadratic (using h_Q) and cubic (using h_C) interactions with memory, $m-1$. Second, the 2nd and 3rd order filtering operations producing x_Q and x_C have been shown to completely reject additive Gaussian noise [43, 44], which is especially beneficial in low MI imaging. Third, and perhaps most importantly, the quadratic and cubic kernels, when appropriately matched to the signal nonlinearities, capture quadratic and cubic interactions throughout the full observable frequency range, not just in specific bands such as the second and third harmonics.

2.1.2 Determination of the TVF Kernel Coefficients

Equation 2.2 provides a means for determining the values of the TVF kernel coefficients through a minimum norm least square (MNLS) solution as suggested in [40, 45]. This is based on the fact that, while Equation 2.2 is nonlinear in the data, it is linear with respect to the kernel coefficients. Therefore, it is possible to form an equation of the form,

$$\boldsymbol{G}_n \boldsymbol{h}_n = \boldsymbol{x}_n + \boldsymbol{\nu}_n, \tag{2.3}$$

where

$$\begin{aligned}\boldsymbol{h}_n =&[h_L[0], h_L[1], \ldots, h_L[m-1], \cdots h_Q[0,0], \ldots, h_Q[m-1, m-1],\\ &\cdots h_C[0,0,0], \ldots, h_C[m-1, m-1, m-1]]^T\end{aligned}$$

is the unknown vector containing the linear, quadratic and cubic kernel coefficients. The vector $\boldsymbol{x}_n$ represents the observed data at N samples, where

$$\boldsymbol{x}_n = [x[n], x[n-1], \cdots, x[n-N+1]]^T.$$

The data matrix $\boldsymbol{G}_n$ is given by

$$\boldsymbol{G}_n = [\boldsymbol{G}_L[n]\ \boldsymbol{G}_Q[n]\ \boldsymbol{G}_C[n]].$$

The structure of the sub-matrices follows from Equation 2.2 and depends on the degrees of symmetry enforced on the quadratic and cubic kernels. Typically, the number

of unknown filter coefficients, M, is given by

$$M = M_L + M_Q + M_C = m + \frac{m(m+1)}{2} + \frac{m(m+1)(m+2)}{6} < N,$$

which leads to an overdetermined system of equations. Since $\boldsymbol{x}_n$ is formed from the (noisy) observed data, these equations may be inconsistent. In this case, an optimal minimum-norm least-squares solution is sought using the Moore-Penrose pseudoinverse (through the singular value decomposition of $\boldsymbol{G}_n$) [40, 45]. A more computationally efficient solution is obtained using the recursive least squares adaptive filtering approach described next.

2.1.3 The VF Memory, m

The memory of the VF filter depends on the nature of the nonlinearity. For example, a static nonlinearity such as a square-law device can be captured with zero memory, $m = 1$ in Equation 2.2. Microbubbles oscillating according to the modified Herring equation (1.1) or similar dynamic models require larger values of m to capture these dynamics. The default value of $m = 15$ represents a temporal memory of 0.375 μs at a sampling frequency of 40 MHz.

Take one experimental data set as an example. (More details will be given in Section 4.1.) $m = 11$ and $m = 19$ produced very similar results in terms of UCA enhancement spectral bands. On the other hand, $m = 30$ resulted in deterioration in UCA enhancement bands. This can be attributed to the fact that the matrix $\boldsymbol{G}$ became increasingly more ill-conditioned as increasing m, which can result in inaccurate solution to the MNLS problem in (2.3).

2.2 Adaptive Algorithms

The linearity of Equation 2.2 with respect to the Volterra kernels allows for the straightforward extension of the least mean squares (LMS) and recursive least squares (RLS) adaptive algorithms for identifying these coefficients [46]. The exponentially weighted RLS algorithm with forgetting factor, λ, is employed and described by the following

equations:

$$\begin{aligned} \boldsymbol{k}_n &= \frac{\boldsymbol{P}_{n-1}\boldsymbol{x}_n}{\lambda + \boldsymbol{x}_n^H \boldsymbol{P}_{n-1}\boldsymbol{x}_n}, \\ \xi[n] &= x[n+1] - \boldsymbol{h}_{n-1}^H \boldsymbol{x}_n, \\ \boldsymbol{h}_n &= \boldsymbol{h}_{n-1} + \boldsymbol{k}_n \xi^*[n], \\ \boldsymbol{P}_n &= \lambda^{-1}(\boldsymbol{P}_{n-1} - \boldsymbol{k}_n \boldsymbol{x}_n^H \boldsymbol{P}_{n-1}), \end{aligned} \tag{2.4}$$

where $\xi[n]$ is the a priori error, $\boldsymbol{k}_n$ is a gain vector and $\boldsymbol{P}_n$ is the inverse matrix of the deterministic correlation matrix given by

$$\boldsymbol{\Phi}_n = \sum_{i=1}^{n} \lambda^i \boldsymbol{x}_i \boldsymbol{x}_i^H + \delta \lambda^n \boldsymbol{I}, \tag{2.5}$$

where δ is a regularization parameter and $\boldsymbol{I}$ is the identity matrix.

2.2.1 Regularization Parameter α and Forgetting Factor λ

The first step to apply the RLS algorithm is to determine the initial value of the time-average correlation matrix $\boldsymbol{\Phi}_0 = \delta I$ with δ given by

$$\delta = \sigma_x^2 (1-\lambda)^{\alpha}, \tag{2.6}$$

where σ_x^2 is the variance of the data $\boldsymbol{x}_n$ and α is a parameter whose value depends on the input SNR. Typically, RLS achieves fast convergence rate and a small steady-state value of the ensemble-average squared error with higher SNR [46]. For SNR values above 30 dB the value of α is 1. For medium SNR values on the order of 10 dB the value of $-1 \leq \alpha < 0$ is used. The value of λ is chosen such that $1 - \lambda \ll 1$.

2.2.2 Determination of the VF Kernel Coefficients

In principle, adaptive filters can be implemented so that their coefficients can be updated on a sample-by-sample basis. In imaging applications, however, this approach can lead to heterogeneity in the image intensity. A more appropriate approach is to derive the coefficients from selected A-line(s) acquired with UCA present. Once the RLS algorithm converges, the estimated kernel coefficients are used in the signal decomposition model of Equation 2.2 to produce the linear, quadratic and cubic components as illustrated in Figure 2.1.

2.2.3 Algorithm Convergence

The main advantage of the RLS algorithm is its robustness and guaranteed convergence. In principle, RLS is able to achieve a fast convergence rate and a smaller steady-state value of the ensemble-average squared error, compared to MNLS, LMS, etc. In the context of linear filtering, the convergence is within $2m$ iterations for an order m filter. For the kernels shown in this dissertation, the number of independent coefficients was in the hundreds, but the convergence was achieved within 200 - 300 iterations (samples) with well-behaved learning curves. It should also be noted that what is important here is that the RLS algorithm converges rather than the speed of convergence since the same filter coefficients are applied to the whole data set.

2.3 Image Display

The three components of the TVF have different dynamic ranges due to noise rejection and the use of polynomial operations on the data samples (for obtaining the quadratic and cubic components). For this reason each of the three components must be displayed with its own dynamic range. The linear component has approximately the same dynamic range as the RF while the quadratic and cubic components have greater dynamic ranges. In this dissertation, the echogenicity values in dB are referenced to the maximum absolute value in the RF data collected with UCA present. This normalization is also applied to the standard B-mode without UCA, PI, linear B-mode (LB-mode), quadratic B-mode (QB-mode), and cubic B-mode (CB-mode) images from the same experiment.

2.4 UCA VF and Tissue VF

As detailed in Section 2.2.2, the filters (referred to as the "UCA filters") are derived from selected A-line(s) acquired with UCA present. The realtime implementation of UCA filters is limited because one has to detect the UCA location beforehand.

At low MI settings, tissue nonlinearity is suppressed; ultrasound propagates linearly in tissue [47]. However, tissue nonlinearity can also result from nonlinear distortion produced by the clinical transducers [48]. Therefore, a TVF can also be trained from

A-line(s) from tissue components only. These filters are referred to as the "tissue filters".

Theoretically, UCA and tissue components exhibit different types of nonlinearities which are affected by MI, acoustic pressure and so on. Therefore, the filters trained by UCA and tissue components are designed to capture the nonlinearities of their own. However, because of the nature of VFs, tissue filters should also be able to pick up UCA nonlinearity even though the outputs may not be as ideal as the ones using the UCA filters. Consequently, it is feasible to derive the filter coefficients from any data component and still capture UCA nonlinearity. The experimental results which will be described next will show that the VF kernel coefficients depend on the training of the data, but the behavior remains the same. This property simplifies the realtime implementation of a TVF.

2.4.1 Experimental Results

Figure 2.2 shows the temporal mean and standard deviation plots resulting from two different "Tissue Filters" (red) compared to the results obtained using the "UCA Filter" (black). The data used to generate the plots were acquired during one *in vitro* experiment. More details regarding to the experiment will be given in Section 4.1. The UCA filter coefficients were derived using the RF data containing echoes from the cellulose tube while pumping the UCA solution. Other "tissue filters" were also derived from RF data containing echoes from tissue. These results show that the VF kernel coefficients depend on the training, but the behavior remains the same. It is interesting to note that the quadratic kernel exhibited larger sensitivity than that of the linear and cubic kernels.

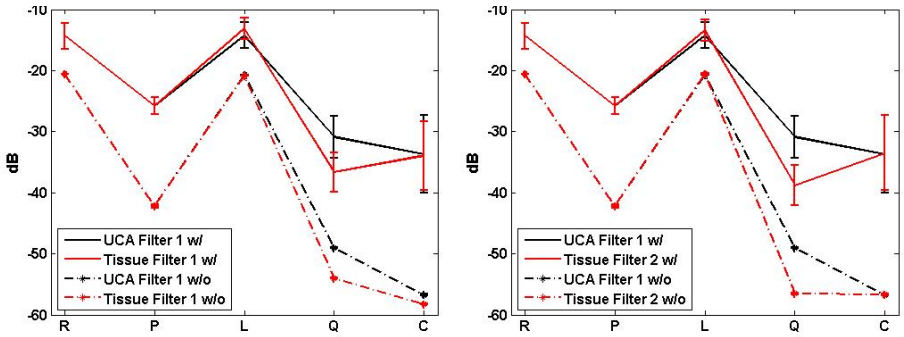

(a) Tissue Filter 1 (b) Tissue Filter 2

Figure 2.2: The temporal mean and standard deviation of the power at the cellulose tube region using the outputs of different TVFs.

2.5 Quadratic Kernels Derived from Second-order versus Third-order VFs

The order of VF determines UCA nonlinearity captured. The nature of microbubble nonlinear oscillation is able to produce third or even higher harmonic signals under low MI [49]. Therefore, increasing the order of the VF can capture more nonlinearities of higher order. However, the number of filter coefficients increases exponentially with the growth of the order of the VF. As a result, the filter requires a large amount of data computation.

A TVF is capable of capturing an even order (second) and odd order (third) nonlinearities from the ultrasound backscattered signal. The two components captured are independent from each other and sufficient for our application. Moreover, the number of coefficients, M, of a TVF is confined and implementable for a realtime application.

Of concern is whether applying a third-order VF will affect the quadratic output. In the earlier publication [40], second-order VFs were proposed to capture UCA nonlinearity. Increasing the filter order to three may affect the quadratic output. To explore the change of quadratic components derived from second-order and third-order VFs,

one can write down the expression of second-order VF as follows:

$$\begin{aligned} x[n+1] &= \nu_1[n] + \sum_{h_0=0}^{m-1} h_L[h_0]x[n-h_0] + \sum_{h_0=0}^{m-1}\sum_{h_1=0}^{m-1} h_{Q1}[h_0,h_1]x[n-h_0]x[n-h_1] \\ &= \nu_1[n] + x_L[n] + x_{Q1}[n]. \end{aligned} \tag{2.7}$$

In principle, with infinite-memory implementation, $\nu_1[n] = \nu[n]+x_C[n]$ and $x_{Q1}[n] = x_Q[n]$. However, the filters can only be implemented with finite memory. Moreover, the filter performance also depends on the choice of initial parameters of the RLS algorithm. On the other hand, the signal leakage between odd- and even-order components should not be significant. Therefore, the change of quadratic components may exist but is limited. Consequently, the difference between h_{Q1} and h_Q should be indistinguishable.

2.5.1 Experimental Results

To analyze the differences between the SVF quadratic kernels (SVF-QK) and the TVF quadratic kernels (TVF-QK), a second-order and third-order VFs were derived using the RLS algorithm and applied to on experimental data set. More details regarding to the experiment and data will be give in Section 4.3.

Filter Coefficients Derivation: Both SVF and TVF were derived with the same A-line with the presence of UCA. The RLS initialization parameters were set to the same (see Section 4.3.2 for the values). The coefficients were updated on a sample-by-sample basis. Both SVF and TVF converged after 175 samples.

Filter Coefficients: Figure 2.3 is the plot of quadratic kernels in the time domain (blue: SVF-QK, red: TVF-QK). It is clear that two groups of quadratic kernels had relatively the same value.

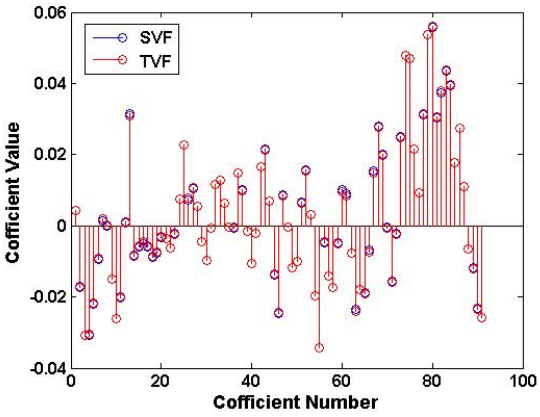

Figure 2.3: The quadratic kernels of the SVF (blue) and TVF (red).

SVF-QK and TVF-QK Frequency Responses: The frequency responses of two quadratic kernels are shown in Figure 2.4. The magnitude was displayed in log-compression. One can tell that the frequency response computed using the two groups of quadratic kernels were approximately the same.

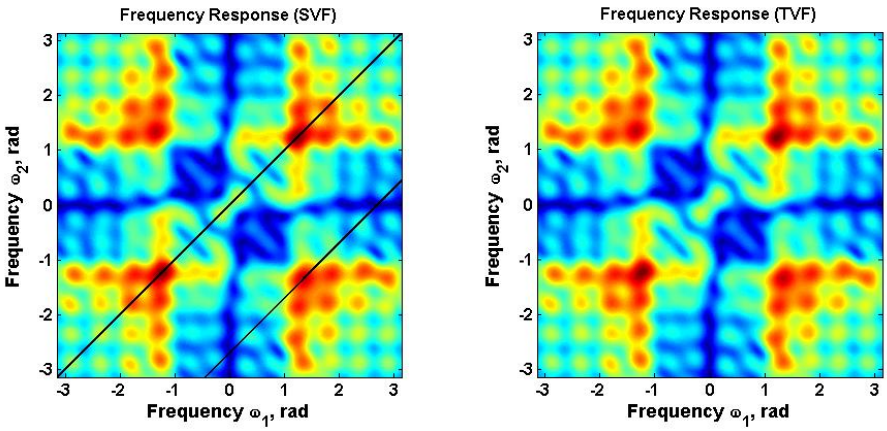

(a) SVF-QK Frequency Response (b) TVF-QK Frequency Response

Figure 2.4: The frequency response of SVF-QK (left) and TVF-QK (right).

Further comparison can be found in Figure 2.5. Figure 2.5 is the frequency response at frequencies $\omega_1 = \omega_2$ and $\omega_1 = \omega_2 - 2.69$, which corresponds to the two black lines in Figure 2.4a. The two lines were chosen because they contained local maxima in the

2D frequency response plot. The frequency response was almost the same for the two kernels.

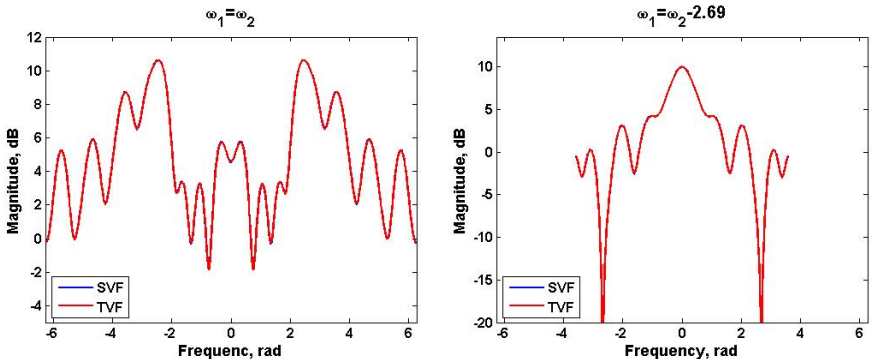

Figure 2.5: The frequency response of quadratic kernels at frequencies $\omega_1 = \omega_2$ (left) and $\omega_1 = \omega_2 - 2.69$ (right). The blue plots were drawn with SVF-QK and the red plots with TVF-QK. The magnitude was displayed in the log-compression.

Therefore, SVF-QK and TVF-QK can achieve the similar performance when derived using the same data samples and the same RLS initialization parameters. The difference is indistinguishable.

Chapter 3

Temporal Perfusion Index

3.0 Introduction

UCA can improve perfusion imaging quality due to the nonlinear oscillations of microbubbles. Moreover, perfusion imaging can be improved by accounting for the UCA dynamic behavior resulting from pulsation and blood circulation. When microbubbles enter and leave the imaging slice, each imaging frame represents an independent "UCA event". The temporal perfusion index (TPI) is proposed to provide a qualitative measure of microbubble perfusion density by accounting for different UCA events. It is designed as a spatial measurement that rewards temporal variance at a given image pixel and penalizes the average image intensity over a small spatial mask.

3.1 Statistical Models for the Ultrasound Backscattered Signal

An ultrasound system which adopts pulse-echo principle acquires the radio frequency (RF) backscattered signals. The envelope of RF the signal, computed using Hilbert transform, is used for characterizing the signal magnitude. Logarithmic compression is routinely followed and employed to reward the weak ultrasound backscattered signal. However, the full dynamic range of the log-compressed enveloped signal retains all noise components which result in artifacts within the further treatment. Therefore, a reduced dynamic range is needed to preserve UCA activities, while rejecting noise to the greatest

extent.

As detailed in Section 2.3, linear, quadratic and cubic components of the outputs of a TVF have different dynamic ranges due to the use of polynomial operations. Therefore, it is difficult to compare dynamic perfusion density computed with different components. One way to provide a comparable measurement among three components is by mapping the log-compressed data with their dynamic range to 256 gray levels, which also accounts for image perception on a standard 8-bit display.

The data transformation can be summarized as follows:

$$\begin{aligned} S_{\mathcal{H}} &= \mathcal{H}(s) \\ \nu &= 20\log_{10}\sqrt{S_R^2 + S_I^2} \\ \nu_{min} &= max(-dR, min(\nu)) \\ I &= \frac{\nu - \nu_{min}}{\nu_{max} - \nu_{min}} \times 255, \end{aligned} \tag{3.1}$$

where s is a vector of ultrasound backscattered RF signal, the symbol $\mathcal{H}$ stands for the Hilbert transform, $S_{\mathcal{H}}$ is the Hilbert transform of s, and S_R and S_I are the real and imaginary parts of $S_{\mathcal{H}}$, respectively, ν is the magnitude of the signal s and dR is the selected dynamic range.

3.2 Temporal Perfusion Index

The TPI is a pixel-wise measurement operating on signal I, which is on grey levels. The TPI was first proposed in [50]. It is a statistical index, which is used to capture the dynamic behavior of single bubble or small clusters of bubbles as they enter and leave the imaging slice. The expression is as follows:

$$TPI(x, z, k) = \frac{\sigma_I^2(x, z, k)}{[\hat{\mu}_I(x, z, k)]^{\gamma}}, \tag{3.2}$$

where

- The variance $\sigma_I^2(x, z, k)$ is the temporal variance of the pixel intensity $I(x, z)$ in frame k,

$$\sigma_I^2(x, z, k) = \frac{1}{N_f + 1} \sum_{\ell=k}^{k+N_f} \left(I(x, z, \ell) - \bar{I}(x, z, k)\right)^2,$$

with the moving average $\bar{I}(x, z, k)$ at pixel (x, z) being

$$\bar{I}(x, z, k) = \frac{1}{N_f + 1} \sum_{\ell=k}^{k+N_f} I(x, z, \ell).$$

The computation is based on the frames $\ell = k, k + 1, \ldots, k + N_f$. The value of N_f is determined from the frame rate and the range of motion observed in the B-mode images. If N_f is too large, the TPI loses sensitivity to the UCA variation. On the other hand, if it is too small, the artifacts from the animal's motion and/or noise will be enhanced.

- $\hat{\mu}_I(x, z, k)$ is the local mean intensity and obtained through a spatial convolution in frame k.

$$\hat{\mu}_I(x, z, k) = \frac{1}{N_f + 1} \sum_{\ell=k}^{k+N_f} (\boldsymbol{h(x, z)} \ast\ast \boldsymbol{I(x, z, k)})$$

The 2D impulse response of the spatial filter, $h(x, z)$, operates on $I(x, z, k)$ in the spatial coordinates to reduce the effects of motion. A typical size of this filter is 31×3 designed as a 2D moving average.

- The intensity ratio γ controls the relative suppression of the high-echogenicity pixels to low-echogenicity pixels. Typical value of γ is in the range of 0.1 - 1. Its effect is to raise the low-echogenicity (UCA) average intensity above the noise floor. This may lower the TPI value for these pixels, but it also improves the robustness of this index in the presence of noise.

3.2.1 Dynamic Range Selection for TPI Computation

The dynamic range (in decibels) for TPI computation is designed to preserve UCA activity, while rejecting noise. The choice of dynamic range is crucial since echogenicities from UCA can be very subtle and at the noise level. In principle, if the dynamic range is too small, UCA activities might be excluded. On the other hand, if the dynamic range is too large, noise may be retained and introduce large TPI artifacts. Therefore, it is important to determine dynamic range before applying the TPI processing.

In [51], Younesy *et al* proposed a differential time-histogram table to visualize the time-varying scalar data. They stated that the histogram distribution reflects a feature

of the functional dimension and usually the feature is extracted at values where the range of data varies greatly. We adopt the idea of the time-histogram table and refer to variations of the probability distribution function (PDF) to determine the dynamic range for TPI computation.

Define $f(\nu, t)$ as the PDF of the log-compressed ultrasound backscattered signal. The PDFs of the backscattered signal before and after injecting UCA microbubbles are represented as $f_B(\nu, t)$ and $f_A(\nu, t)$, respectively. The two variables ν and t stand for the log-compressed signal magnitude and the frame number, respectively. The PDF can be written as:

$$\begin{aligned} f_B(\nu, t) &= f_T(\nu, t) + f_N(\nu, t), \\ f_A(\nu, t) &= f_T(\nu, t) + f_N(\nu, t) + f_{UCA}(\nu, t), \end{aligned} \tag{3.3}$$

where $f_T(\nu, t)$ is the high magnitude component reflected from tissue components, $f_N(\nu, t)$ is the low magnitude noise, and $f_{UCA}(\nu, t)$ is the UCA component. Typically, $f_{UCA}(\nu, t)$ is at the low magnitude level. The difference between f_B and f_A is not significant and may not be able provide guidance to locate the UCA signal.

Due to the UCA dynamic behavior resulting from pulsation and blood circulation, the variation of f_{UCA} over frames is profound. Therefore, it can be used as a means for locating the level of the UCA signal. Define $V_B(\nu)$ as the variation of $f_B(\nu, t)$ over frames and $V_A(\nu)$ as the variation of $f_A(\nu, t)$ over frames. Assume the different components to be independent, we have:

$$\begin{aligned} V_B(\nu) &= \sigma_t^2[f_B(\nu, t)] = \sigma_t^2[f_T(\nu, t)] + \sigma_t^2[f_N(\nu, t)], \\ V_A(\nu) &= \sigma_t^2[f_A(\nu, t)] = \sigma_t^2[f_T(\nu, t)] + \sigma_t^2[f_N(\nu, t)] + \sigma_t^2[f_{UCA}(\nu, t)], \end{aligned} \tag{3.4}$$

where the main contribution to V_B comes from the variation of tissue motion and noise, and the main contribution to V_A comes from the variation of UCA microbubble activity as well as motion and noise. Therefore, the subtraction of $V_A - V_B$ could locate the UCA signal level and determine the dynamic range to preserve the change from UCA activity while suppressing the variation due to noise and tissue motion.

3.3 Motion-triggered Temporal Perfusion Index

In *in vivo* experiments, the sensitivity of the TPI to the presence of UCA can be degraded due to the animal's dominant breathing motion. Under this condition, the

parameter choice for the TPI computation is more confined in order to successfully track the UCA activity. To overcome this difficulty and to better discriminate between echo changes due to UCA activity and changes due to tissue motion and noise, motion-triggered TPI is introduced. The motion-triggered TPI can cancel out the motion effect by accounting for the breathing motion.

Suppose the animal's breathing is approximately periodic, it is possible to align the frames based on their occurrence within the breathing cycle. This is done in motion-triggered TPI by determining the time frame of a breathing cycle of N_t frames. Then the TPI equation, rather than being iterated per frame is instead iterated by N_t frames. The equation is as follows:

$$TPI(x, z, k) = \frac{\sigma_I^2(x, z, \ell)}{[\hat{\mu}_I(x, z, \ell)]^\gamma}, \tag{3.5}$$

where $k = 1, 2, \ldots, N_t$ and $\ell = k, k + N_t, ..., k + N_t \times \lambda$. The parameter λ is determined based on the total number of frames N collected during the experiment such that $k + N_t * \lambda \leq N$.

3.3.1 Dynamic Range Selection for Motion-triggered TPI

The motion-triggered TPI is determined by being iterated by N_t frames, where N_t is the breathing cycle. As a consequence, the method to determine the dynamic range for motion-triggered TPI computation is required to change. To achieve this goal, the variation of the animal's motion needs to be suppressed. Define the PDF Δf as

$$\Delta f(\nu, t) = f(\nu, t + N_t) - f(\nu, t), \tag{3.6}$$

where N_t is the breathing cycle.

The frames t and $t + N_t$ are at the same stage in successive period of the breathing cycle. Consequently, the backscattered echoes from tissue component are supposed to similar and could be cancelled out. On the other hand, UCA activity is preserved due to its nonlinear and nonperiodic dynamic properties. Accordingly, instead of using variation of f over frames, the variation of Δf over frames can tell which signal level the contrast agent activity is excited on, therefore allows to determine the dynamic range.

3.4 Motion Correction

The motion-triggered TPI uses the assumption that animal's breathing motion is approximately periodic. However, with aperiodic motion present, motion-triggered TPI may result in artifacts. A motion correction algorithm is proposed to improve the specificity and sensitivity of the TPI with aperiodic motion present. The algorithm adopts two-dimensional normalized correlation of the RF signal at different frames and is formed as:

$$\rho(i,j) = \frac{\sum_{x=1}^{M}\sum_{z=1}^{N}(S_0(x,z)-\bar{S_0})(S_1(x+i,z+j)-\bar{S_1})}{\sqrt{\sum_{x=1}^{M}\sum_{z=1}^{N}\left(S_0(x,z)-\bar{S_0}\right)^2\sum_{x=1}^{M}\sum_{z=1}^{N}\left(S_1(x+i,z+j)-\bar{S_1}\right)^2}}, \quad (3.7)$$

where S_0 and S_1 are the RF signals in the reference and search regions, respectively, and $\bar{S_0}$ and $\bar{S_1}$ are their average, respectively. M and N are sizes of the searching window in the axial and lateral dimensions, respectively. x and z are the axial and lateral coordinates of the pixel, respectively. i and j are the axial and lateral coordinates of a mismatched pixel in the search region, respectively. ρ is the normalized correlation.

Compared to motion-triggered TPI, the motion correction algorithm is a more accurate way to cancel out motion effect and reduce the TPI artifacts resulting from motion. However, the motion correction algorithm requires long-time data computation. Therefore, for actual applications, one needs to seek for a balance.

3.5 Qualitative and Quantitative Perfusion Measurement

The TPI detailed in this chapter provides a qualitative measure of microbubble perfusion density by accounting for different UCA events. One upside of the TPI is that it can preserve the temporal resolution of UCA activity by accounting for its dynamic behavior resulting from pulsation and blood circulation for a small number of frames.

The ultimate goal of the TPI is to provide a quantitative measurement of microbubble perfusion density. The TPI should be capable of distinguishing different perfusion levels and providing a quantitative comparison between them. To achieve this goal the intensity ratio γ needs to be carefully designed.

Generally speaking, the intensity ratio γ is chosen based on the echogenicity in order to normalize the temporal variance using the local mean. In principle, large values of

γ result in small TPI value, but instead enhance the ratio of UCA TPI value over tissue TPI value. Therefore, a large value of γ provides better discrimination between UCA and tissue components in dynamic perfusion imaging. This is more important for the low-perfusion regions since the high-perfusion regions are already well handled. However, a large value of γ may also increase the risk of increasing artifacts from noise. The proper choice of γ is therefore a delicate tradeoff between two limiting cases.

Chapter 4

In Vitro Validation Studies

4.0 Introduction

The objective of *In vitro* validation study is to approximately mimic *in vivo* conditions while providing a system where ground truth can be independently designed for method testing. Four validation studies are provided in this chapter. Firstly, a study on characterization of microflow is presented with the data acquired from cellulose microchannels embedded in a tissue-mimicking phantom. The study is to test whether the TVF and TPI are suitable for delivering high quality perfusion imaging, capturing its dynamic behavior, and providing spatial and temporal characterization. Secondly, a spatial heterogeneous perfusion and flow imaging study is presented with the data acquired from a flow channel embedded in a tissue-mimicking phantom. The study is to test the performance of the TVF and TPI in terms of the sensitivity and specificity to heterogeneous perfusion imaging. Following that, a preliminary study on longitudinal perfusion imaging is introduced to provide a comparison between TVF components and PI regarding to the sensitivity to heterogeneous perfusion imaging. Last but not least, a preliminary study on combined flow and microflow imaging is briefly introduced to provide a feasibility test on simultaneously detecting perfusion at the capillary level and flow in the artery.

4.1 Spatial and Temporal Characterization of Microflow using TVF

4.1.1 Experiment Setup

Figure 4.1 shows the phantom experiment setup using the LA14-5/38 imaging probe. The imaging system was described in Section 1.3.1. The tissue-mimicking phantom was made following the procedure described by Nightingale *et al* [52]. The scanner was used in the clinical mode to image the phantom and to test the appearance of the speckle under a low MI value of 0.13 before switching to the research mode. Care was taken to avoid saturation and clipping of the RF data.

One 200-μm diameter cellulose tube (Spectrum Laboratories, Rancho Dominguez, CA) was embedded in the center of the phantom. Imaging data were acquired while the channel was filled with saline or UCA microbubbles. This contrast target, with spatial extent smaller than the point spread function of the imaging probe, served to characterize the spatial specificity of the different imaging methods.

Targestar-P (Targeson, San Diego, CA) was used in the experiments reported herein. Targestar-P is a non-targeted perfusion contrast agent with a mean diameter of 2.03 $\pm$ 0.04 μm. It is designed to enhance and quantify blood flow and vascular function. The shell type is a lipid encapsulated perfluorocarbon microbubble incorporating a coating of polyethylene glycol. The UCA was diluted 1 : 15 with sterile saline in 2.5 mL solution. The approximate microbubble concentration was approximately 1.8×10^8 microbubbles per mL.

The LA14-5/38 probe was driven using a single cycle pulse at a frequency of 7.2 MHz, i.e. matching the center frequency of the transducer. The transmit focus was placed at a depth of 29 mm, approximately the axial position of the cellulose tube.

Imaging Slice Selection for Improved UCA Specificity: The cellulose tube produced a strong specular echo when the imaging probe was orthogonal to the tube's axis. To avoid the possible loss of sensitivity to UCA activity, the probe was tilted slightly in the elevation direction to minimize the specular reflection while the cellulose channel was filled with saline. With the probe tilted, the channel echogenicity was indistinguishable from the surrounding tissue in B-mode. Once this was accomplished, the following

procedure was used to collect the data:

1. The scanner was used in research mode to allow RF data collection.
2. Saline was pumped through the tube using a syringe pump (KD Scientific, Holliston, MA) at a rate of 6 mL/hour.
3. RF PI data frames (128 lines) were collected while saline was being pumped.
4. UCA was pumped through the tube at 6 mL/hour using the syringe pump.
5. RF PI data frames were collected while UCA was being pumped.

In each case, 55 frames were acquired giving more than two seconds of data at approximately 25 frames per second (fps).

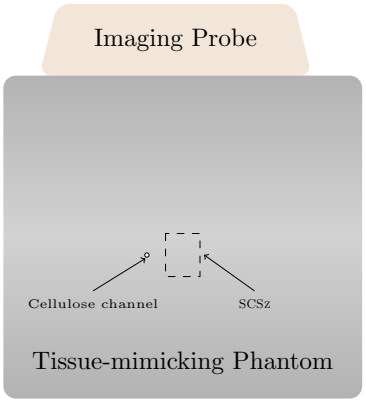

Figure 4.1: A schematic of the phantom imaging setup. The shaded rectangle defines the region for performing speckle statistics and cell size computations. Approximately to scale, but the diameter of the tube is exaggerated.

Contrast Enhancement: The contrast enhancement of the cellulose channel without and with UCA was evaluated as follows:

1. The Contrast-to-Tissue Ratio with UCA:

$$CTR_{UCA} = 10 \log_{10} \left[\frac{P_{UCA}}{P_{tissue}} \right], \tag{4.1}$$

2. The Contrast-to-Tissue Ratio with saline:

$$CTR_{saline} = 10\log_{10}\left[\frac{P_{saline}}{P_{tissue}}\right], \tag{4.2}$$

This ratio was computed to characterize any enhancement due to the walls of the cellulose tube in the absence of UCA.

The power values, P_{UCA}, P_{saline} and P_{tissue}, were computed using samples from a rectangular region, $M'(= 2M + 1)$ A-lines and $N'(= 2N + 1)$ axial samples, containing the echoes from the cellulose channel with UCA, cellulose channel with saline and tissue region at the same depth, respectively. For the cellulose channel, $N' = 31$ and $M' = 3$ were used to define a rectangular region approximately 600×900 μm^2 in the axial and lateral directions, respectively. For the tissue region, the same value of N' was used, but $M = 10$ was used to improve the estimate of average power in tissue. The average power value in a given region was computed using

$$P[t] = \frac{1}{N'M'} \sum_{m=M_0-M}^{M_0+M} \sum_{n=N_0-N}^{N_0+N} |x[m,n,t]|^2, \tag{4.3}$$

where t is the frame number and the ordered pair (N_0, M_0) defines the coordinates of the center of the region in the axial and lateral directions, respectively.

Spatial Resolution and Speckle Statistics: For each imaging mode, the speckle cell size was computed following [53] using a rectangular region with approximate dimensions of 5.6×4.8 mm^2 in the axial and lateral dimensions, respectively. The rectangular speckle region was placed as shown in Figure 4.1. The speckle cell size for this phantom was 0.62 mm laterally and 0.32 mm axially.

4.1.2 Third-order Volterra Filter

Unless otherwise stated, the adaptive RLS algorithm (Equations 2.4&2.5) was implemented using the default values of system order $m = 15$, forgetting factor $\lambda = 0.999$, and regularization parameter $\alpha = -0.1$.

B-mode and PI Reference Imaging: Figure 4.2 shows example B-mode and PI images before and after UCA injection. The dynamic range was set to 45 dB with the

0-dB level determined by the maximum magnitude echo data from the cellulose tube while UCA was present. Both B-mode and PI imaging were sensitive to UCA, but the difference between tissue and UCA echogenicity was much more pronounced for PI as expected. One can see that a residual tissue component remained in PI imaging, approximately 20 dB below the tissue component in B-mode, i.e. just above the noise level for this acquisition setting.

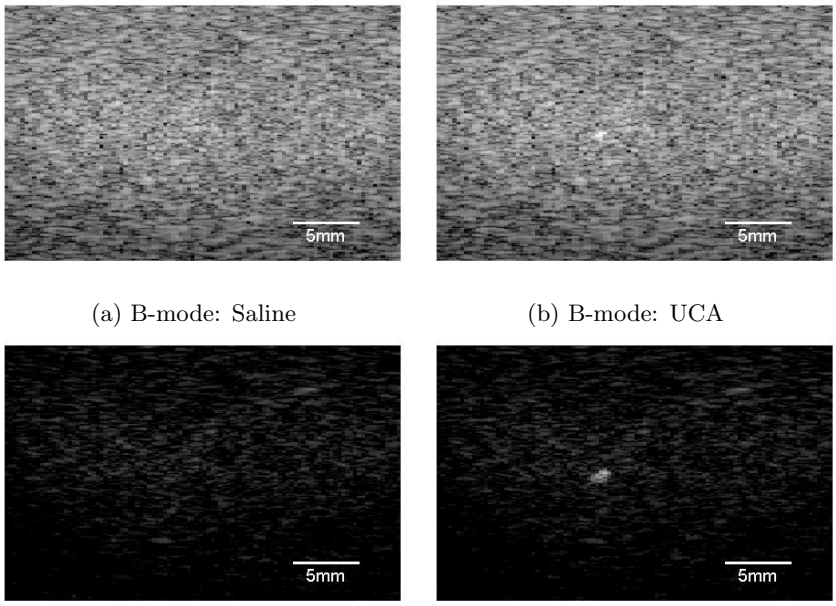

(a) B-mode: Saline (b) B-mode: UCA

(c) PI: Saline (d) PI: UCA

Figure 4.2: B-mode and PI images (45 dB) of the tissue-mimicking phantom while pumping saline (a & c) and UCA (b & d) through the cellulose tube at a flow rate of 6 mL/h. The LA14-5/38 probe was slightly tilted to minimize the specular reflection from the tube.

QB-mode and CB-mode Imaging: The RLS algorithm described in Chapter 2 was applied to selected beamformed RF A-lines passing through the UCA cellulose channel. The default values of m, α, and λ were used. The VF kernels obtained upon convergence were applied to the whole data set, i.e. all A-lines in all frames, without and with UCA. The same RF frame shown in Figure 4.2 was processed using

the quadratic and cubic TVF kernels to produce the corresponding QB-mode and CB-mode images shown in Figure 4.3. The dynamic ranges for these images were set to 60 dB (QB-mode) and 80 dB (CB-mode) with reference to the maximum magnitude of the RF data with UCA present. Qualitatively, both the QB-mode and CB-mode showed enhanced UCA contrast compared to the B-mode image. The tissue echogenicity levels in QB-mode and CB-mode images were estimated at -57 and -70 dB, respectively. These were approximately 20 and 25 dB higher than the noise floor for the quadratic and cubic components, respectively.

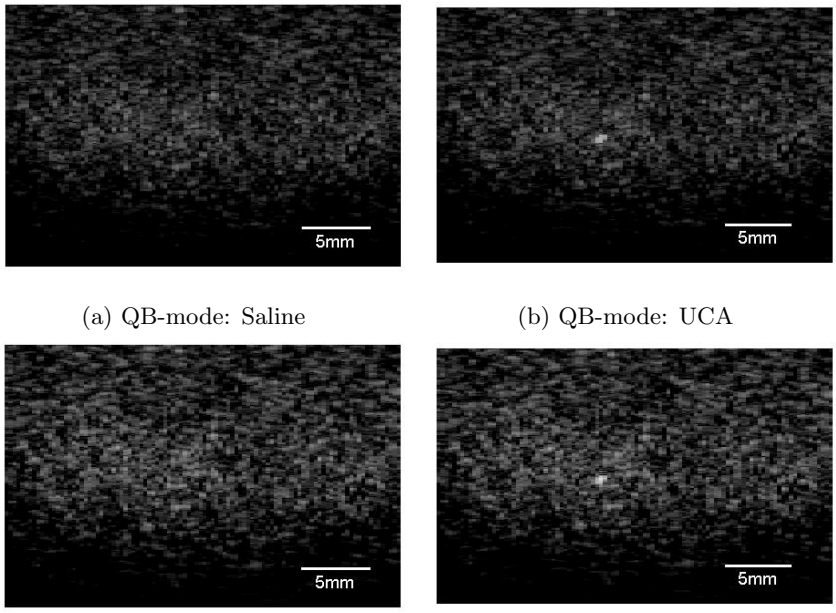

(a) QB-mode: Saline

(b) QB-mode: UCA

(c) CB-mode: Saline

(d) CB-mode: UCA

Figure 4.3: QB-mode (60 dB) and CB-mode (80 dB) images without and with UCA obtained from the RF data used to generate Figure 4.2.

Spatial Characterization of Contrast Enhancement: Figure 4.4 provides a closer comparison between the different imaging modes with respect to the contrast target and the tissue region surrounding it (6.5×8.4 mm^2). The B-mode, PI, QB-mode, and CB-mode images are displayed using a common dynamic range of 50 dB with all components referenced to the same maximum. The UCA enhancement of the channel echogenicity was visible in all components. A-lines # 51 - 53 showed the greatest enhancement in

B-mode and the same was observed in QB-mode and CB-mode. On the other hand, the PI image showed enhancement in A-lines # 50 - 54, i.e. in a larger region around the channel. This pattern consistently has been seen in the majority of collected frames. The RF data are shown from three A-lines: # 52, which showed the greatest enhancement in B-mode, and # 50 & # 54 at the periphery of the enhancement zone. For each A-line the RF data for the $P+$ and $P-$ PI pulses are shown on the left. The UCA echo can be seen starting at an axial distance of 30 mm in A-line #52. The PI (blue), quadratic (red), and cubic (green) RF components are shown for the three A-line segments to provide a direct comparison. For A-line # 52, the UCA enhancement was visible in all three components but it was more spatially confined in the nonlinear VF components.

The PI showed a higher level of echo signal in the channel for A-lines # 50 & # 54. The quadratic and cubic components, on the other hand, did not show appreciable echo changes compared to regions proximal and distal to the channel. Given the lateral extent of the imaging beam, the enhancements seen in A-lines # 50 & # 54 are understood to be due to imperfect cancellation of linear UCA echoes which resulted from near-in sidelobes of the transmit imaging beams. The low-frequency nature of these enhancements is evident from the appearance of the PI echoes shown.

It should be mentioned that the corresponding images and RF data plots have been generated from the same A-line segments collected under saline microflow conditions. No visual enhancement was observed in any of the grayscale images. Similarly, the RF data from the A-line segments did not show any visible enhancement. Therefore, all the enhancements seen in Figure 4.4 are taken to represent sensitivity to UCA.

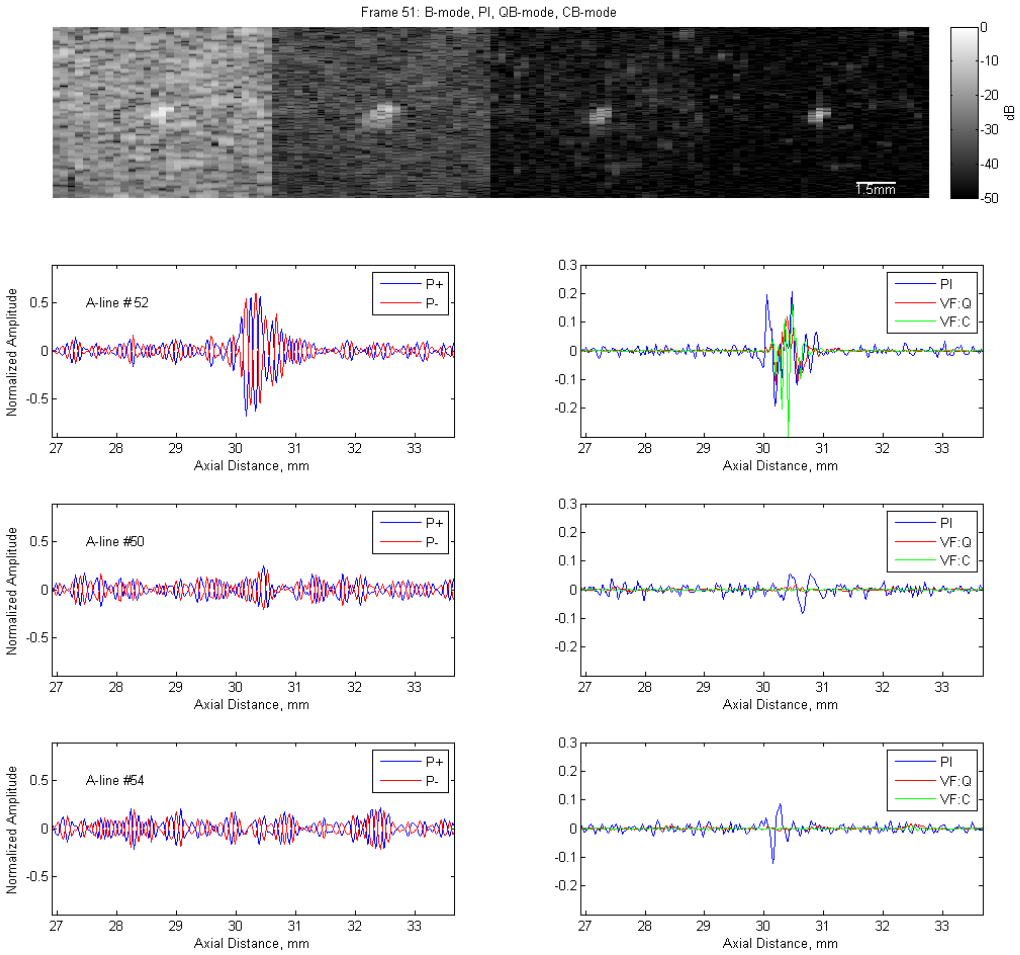

Figure 4.4: Top: Images of all four components using a common dynamic range. Bottom Left: RF data from an A-line passing through the channel showing the echoes from the positive and negative PI pulses. Bottom Right: PI, quadratic and cubic components derived from the RF data shown in the left.

Temporal Characterization of Contrast Enhancement: The collected frames in Cine loop have been reviewed for B-mode, PI, and the TVF components. This review confirmed that each imaging frame represented an independent "UCA event", where the channel echogenicity in the presence of microbubbles changed completely from the

previous frame. This was ascertained by examining the RF data segments from A-lines # 51 - 53, e.g. Figure 4.5 shows A-line # 52, Frame 51. The maximum echogenicity change was dynamic and stochastic in nature in both space (axial and lateral) and time (frame-to-frame). For the purposes of this dissertation, the temporal mean and standard deviation of the echogenicity were evaluated on a pixel-by-pixel basis in a given region of interest (RoI).

The line graphs in Figure 4.5 show the temporal mean (solid lines) and standard deviation (error bars) of the echogenicity along a segment of A-line # 52 with UCA (blue) and saline (red) flowing through the channel. The linear component (left most) produced limited enhancement in the 30 - 30.6 mm axial range, but the mean echogenicity with UCA was not well separated from the saline case. The results from the linear component were practically the same as the results from the RF (not shown) and demonstrated the lack of specificity of conventional B-mode UCA imaging. The PI component (2nd from left) showed significantly higher separation in the axial range of 30 - 31 mm. Similar levels of separation were achieved using the quadratic component (3rd from left) in the axial range of 30 - 30.6 mm (Note the results are plotted in the range -60 – 0 dB). The cubic component (rightmost) produced even higher separation in the axial range of 30 - 30.6 mm (Plotting range of -80 – 0 dB).

The lateral echogenicity through the center of the cellulose channel (similar to Figure 4.5) was also generated. The lateral echogenicity profiles were also consistent with the axial profiles. Specifically, PI, QB-mode, and CB-mode showed clear improvement in sensitivity compared to B-mode. At the same time, the nonlinear TVF components resulted in the same or higher sensitivity as PI with higher spatial specificity.

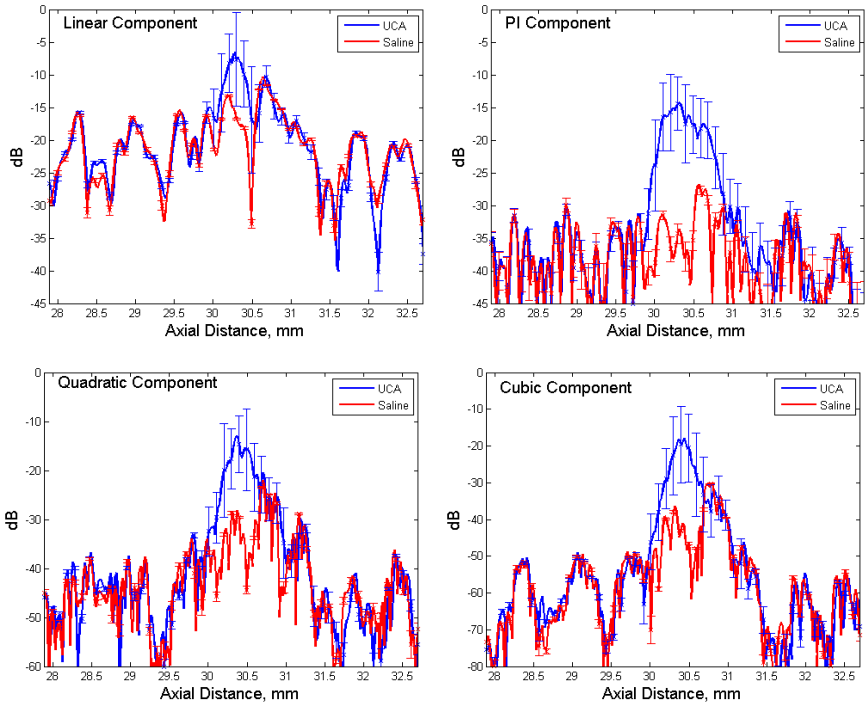

Figure 4.5: Axial echogenicity profiles from an A-line through the cellulose channel. The error bars represent the standard deviation of the echogenicity in the time (frame) direction.

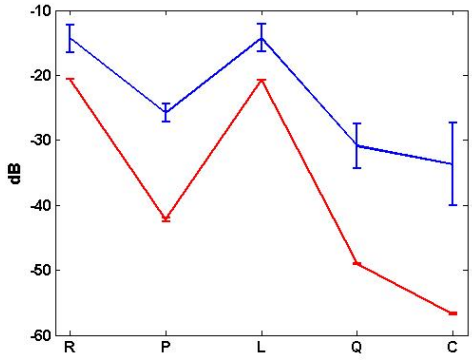

Figure 4.6: Temporal mean and standard deviation of power in a small region containing the cellulose tube for the RF (R), pulse inversion (P), LB-mode (L), QB-mode (Q), and CB-mode (C) images.

Figure 4.6 shows a summary of the temporal variation of the average power in the region containing the cellulose tube for the different imaging modes, i.e. RF (R), pulse inversion (P), LB-mode (L), QB-mode (Q) and CB-mode (C). For each frame, $P[t]$ was computed according to Equation 4.3 with $(M', N') = (3, 31)$ for $t = 1, 2, \ldots, 55$. The graph shows the mean and standard deviation for the time series, $\{P[t]\}_{t=1}^{55}$, collected while pumping UCA (blue) and saline (red). These results were consistent with the line graphs shown in Figure 4.5, but the mean and standard deviation values were lower due to the spatial averaging in Equation 4.3 instead of the pixel-wise calculations used to obtain the line graphs. It should be noted that, even with the spatial averaging in the channel region, the temporal means and standard deviations were higher in the presence of UCA compared to saline only. This trend is important for understanding the *in vivo* results described in Section 5.1 below.

Spectral Characterization of Contrast Enhancement: Figure 4.26 shows the spectrograms of PI, linear, quadratic, and cubic data from A-line # 52 with saline (top) and UCA (bottom) flowing in the cellulose tube. The horizontal axis was labeled as distance (in mm) using the scaling $z = c\tau/2$, where c is the speed of sound (assumed to be uniform) and τ is the echo time. A Hamming window of length 64 was used in computing the spectrogram to preserve the axial resolution while maintaining a reasonable frequency resolution [54].

The spectrograms obtained from the VF components, especially the nonlinear ones, showed an increase in signal level at $\approx$ 30 mm axially, which corresponded to the channel depth. The contrast between the UCA solution and saline flow cases was clear for the PI, quadratic and cubic components. The RF data (not shown) produced similar spectrograms to the linear VF results shown in Figure 4.26 b) & f).

The spectra of linear VF (and RF) showed enhanced response due to the channel in the fundamental band (mainly in the 4 - 6 MHz range). Spectral broadening was observed in the presence of UCA. The PI data with UCA produced broad enhancement in the 2 - 9 MHz range which was clearly above the signal level. In realistic imaging situations with linear array probes, the PI signal has substantial residual tissue component resulting from incomplete cancellation of linear echoes at the sidelobe level.

The nonlinear VF components produced distinct enhancement in the channel before

and after infusing the UCA solution in a much wider frequency range. The spectrograms revealed that both the quadratic and cubic echo components were sensitive to the channel walls even without UCA. However, the differences between the wall and UCA enhancements were pronounced.

4.1.3 Summary of Phantom Imaging Results

The contrast-to-tissue ratios defined in Equations 4.1&4.2 provide a measure of sensitivity to the channel without and with UCA, respectively. Table 4.1 shows the CTR_{saline}&CTR_{UCA} values for the PI, LB-mode, QB-mode, and CB-mode. These values demonstrate, consistent with the graphical results in Figures 4.5&4.26, that the nonlinear VF components achieve CTR enhancement by suppressing, not eliminating, tissue components.

The size of the cellulose channel (200 μm inner diameter and 280μm outer diameter) was smaller than the speckle correlation cell size [53] for the LA14-5/38 probe in the vicinity of the channel (0.62 mm laterally and 0.32 mm axially). Therefore, the extent of the channel estimated using echogenicity is a measure of the spatial specificity. Table 4.2 shows the spatial extent of the UCA region in each image component based on direct measurement from line graphs such as those shown in Figure 4.5. A pixel was included in the UCA region if its mean echogenicity was separated from the tissue mean echogenicity by more than one standard deviation. While the spatial extent was a coarse measurement, especially in the lateral direction, it served to illustrate the sensitivity of the different methods to sidelobe artifacts. In this case, the PI method produced the largest spatial extent which resulted from imperfect cancellation of echo components due to the sidelobes of the imaging beams.

Table 4.1: CTR Values in dB (mean± SD)

	PI	Linear	Quadratic	Cubic
CTR_{saline}	3.9±0.3	2.7±0.0	2.8±0.1	4.6±0.1
CTR_{UCA}	20.2±1.4	9.2±2.1	21.0±3.4	27.8±6.3

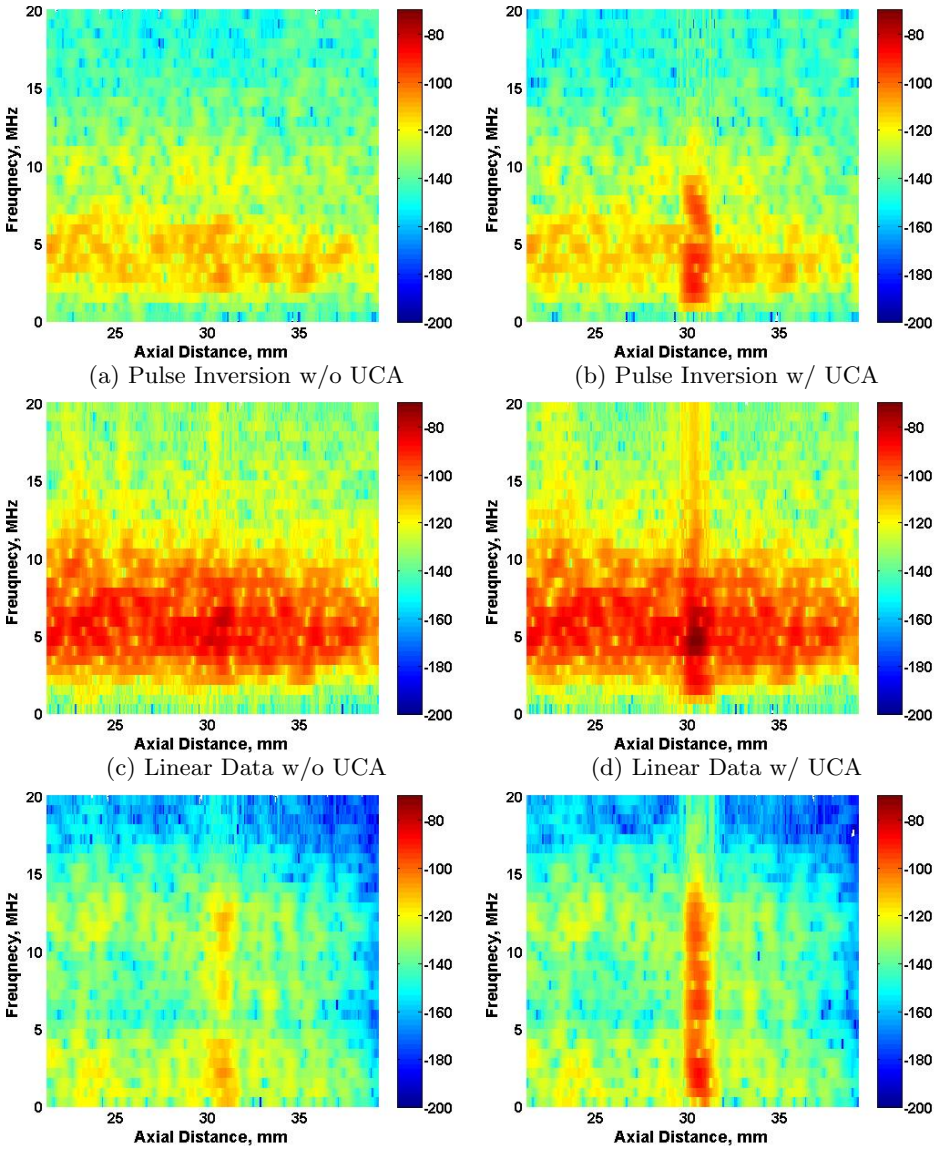

(a) Pulse Inversion w/o UCA

(b) Pulse Inversion w/ UCA

(c) Linear Data w/o UCA

(d) Linear Data w/ UCA

(e) Quadratic Data w/o UCA

(f) Quadratic Data w/ UCA

Figure 4.7: Spectrograms of the A-line through the cellulose channel while pumping saline (left) and UCA (right) at a rate of 6 mL/h.

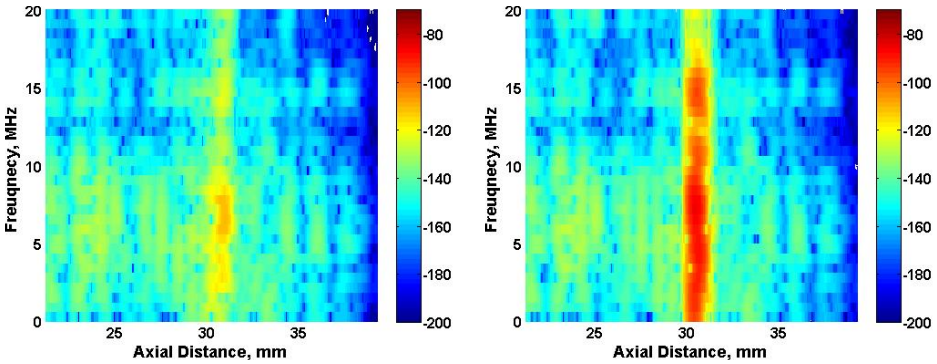

(g) Cubic Data w/o UCA (h) Cubic Data w/ UCA

Figure 4.7: Spectrograms of the A-line through the cellulose channel while pumping saline (left) and UCA (right) at a rate of 6 mL/h.

Table 4.2: Spatial Extent of UCA Activity

	PI	Linear	Quadratic	Cubic
Axial, mm	0.9	0.5	0.5	0.5
Lateral, mm	1.2	0.6	0.6	0.6

The results shown in Tables 4.1 and 4.2 are representative of all the frames collected and allow for the following summary:

i. The quadratic component of the VF produced similar levels of sensitivity (CTR_{UCA}) as PI while offering a higher dynamic range and better spatial specificity.

ii. The cubic component of the VF outperformed the other methods in terms of CTR values, spatial specificity and improved dynamic range.

4.2 Spatial and Temporal Characterization of Microflow using TPI

4.2.1 Experiment Setup

The phantom experiment setup is similar with the one shown in Figure 4.1. The LA14-5/38 probe was driven using a single cycle pulse at a frequency of 7.2 MHz. The imaging system was described in Section 1.3.1. The transmit focus was placed at a depth of 27 mm, approximately at the axial position of the cellulose tube.

Two 200-μm diameter cellulose tubes (Spectrum Laboratories, Rancho Dominguez, CA) were embedded in the center of the phantom approximately 2 mm axially and 3 mm laterally away from each other. Image data were acquired while the channel was filled with saline or UCA microbubbles. Targestar-P (Targeson, San Diego, CA) was used in the experiments reported herein. RF PI data were collected with two different probe positions.

Imaging Slice with Orthogonal Probe: Data were first collected with the imaging probe orthogonal to the tube's axis. The data collection procedure was as follows:

1. The scanner was used in research mode to allow RF data collection.
2. Saline was pumped through the *left* tube using the syringe pump at a rate of 6 mL/hour during the whole experiment.
3. Saline was pumped through the *right* tube using the syringe pump at a rate of 6 mL/hour. RF PI frames ("DATA1") were collected while saline was being pumped.
4. Saline was switched to UCA solution with a concentration of 1×10^8 microbubbles per mL ($1:28$ UCA to saline, low) for the *right* tube. RF PI frames ("DATA2") were collected while UCA solution and saline were being pumped.
5. The concentration of UCA solution was increased to 1.1×10^9 microbubbles per mL ($1:1.5$ UCA to saline, high) for the *right* tube. RF PI frames ("DATA3") were collected while UCA solution and saline were being pumped.

The objective of this procedure was to demonstrate the function of the TPI in the presence of strong specular reflection from the tube walls. The MI at focus was below 0.09. For each round of data collection, 85 frames were collected at the frame rate of 37 fps.

Imaging Slice with Tilted Probe: When the first experiment was done, the imaging probe was tilted until strong reflection from the tube walls disappeared. The data acquisition was then carried out with the following procedures:

1. The scanner was used in research mode to allow RF data collection.
2. UCA solution with concentration of $1:11$ (2.4×10^8 microbubbles per mL) was pumped through the *right* tube using the syringe pump at a rate of 6 mL/hour during the whole experiment.
3. Saline was pumped through the *left* tube using the syringe pump at a rate of 6 mL/hour. RF PI frames ("TDATA1") were collected.
4. Saline was switched to UCA solution with a concentration of 1×10^8 microbubbles per mL ($1:28$ UCA to saline, low) for the *left* tube. RF PI frames ("TDATA2") were collected while UCA solution was being pumped.
5. The concentration of UCA solution was increased to 2.4×10^8 microbubbles per mL ($1:11$ UCA to saline, medium) for the *left* tube. RF PI frames ("TDATA3") were collected while UCA solution was being pumped.
6. The concentration of UCA solution was increased again to 4.8×10^8 microbubbles per mL ($1:5$ UCA to saline, high) for the *left* tube. RF PI frames ("TDATA4") were collected while UCA solution was being pumped.

The objective of this procedure was to demonstrate the nature of qualitative measure of the TPI. The MI at focus was approximately 0.09. For each data acquisition, 104 frames were collected at the frame rate of 37 fps.

TPI Computation: To estimate TPI performance, an average TPI value was computed in a given rectangular region with $(M' = 2M + 1)$ A-lines and $(N' = 2N + 1)$

axial samples. The equation is as follows,

$$TPI[t] = \frac{1}{N'M'} \sum_{m=M_0-M}^{M_0+M} \sum_{n=N_0-N}^{N_0+N} TPI[m,n,t], \tag{4.4}$$

where t is the frame number and the ordered pair (N_0, M_0) defines the coordinates of the center of the region in the axial and lateral directions, respectively. The TPI value is normalized by the maximum value computed. Each experiment shares one common maximum TPI value, regardless of how many data sets were acquired in the experiment.

Spatial Resolution and Speckle Statistics: For each imaging mode, the speckle cell size was computed following [53] using a rectangular region with approximate dimensions of 5.6×4.8 mm^2 in the axial and lateral dimensions, respectively. The rectangular speckle region was placed as shown in Figure 4.1. The speckle cell size for this phantom was 0.74 mm laterally and 0.20 mm axially.

4.2.2 Temporal Perfusion Index with Tube Wall Echoes Present (Orthogonal Probe)

UCA Imaging in Phantom: Figure 4.8 is one frame of RF B-mode and pulse inversion (PI) images of the tissue-mimicking phantom using "DATA3". The images were displayed using a dynamic range of 25dB. The linear probe was orthogonal to the tubes' axes during the data acquisition. Strong specular reflections from the channel walls were detected. The locations of two cellulose channels were distinguishable in both images. The data were acquired when pumping UCA solution with a concentration ratio of 1 : 1.5 through the right channel and saline through the left channel. However, the difference between two tubes was not visible in either images.

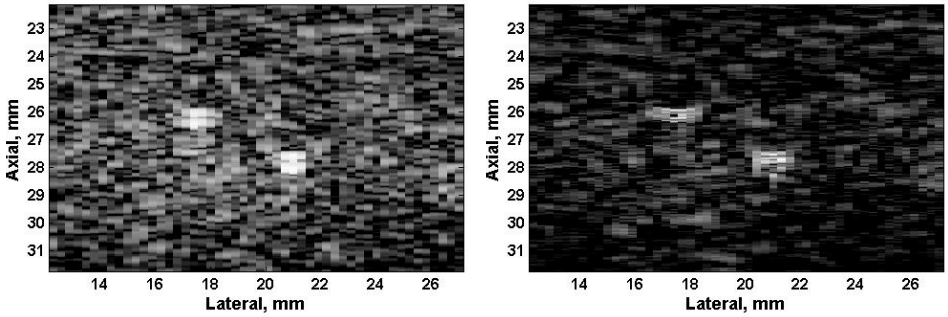

(a) RF B-mode (b) Pulse Inversion

Figure 4.8: One frame RF B-mode and PI images (25dB) of the tissue-mimicking phantom when UCA solution with a concentration of 1 : 1.5 being pumping through the right channel and saline through the left channel. The LA14-5/38 probe was orthogonal to the tubes' axes.

Volterra Filtering: The parameters to derive the TVF were set as forgetting factor $\lambda = 0.999$ and regularization parameter $\alpha = -0.5$, and it took approximately 400 samples before the filter converged. After the filter was derived, it was applied to the whole data set. Figure 4.9 shows QB-mode and CB-mode images produced using the same RF frame shown in Figure 4.8. The difference between two channels was still invisible.

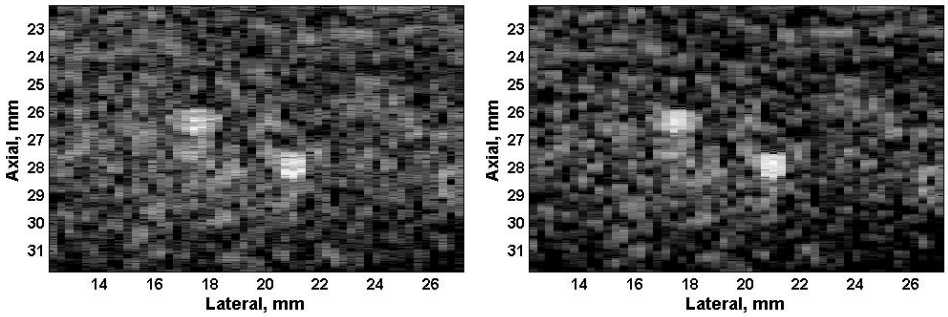

(a) Quadratic Component (b) Cubic Component

Figure 4.9: QB-mode (48 dB) and CB-mode (65 dB) images obtained from the RF data used to generate Figure. 4.8.

Temporal Perfusion Index: The TPI was applied to capture UCA activity and separate it from tube walls and tissue component. As detailed in Section 4.1, nonlinear components show higher sensitivity to UCA activity. To make it more concise, only TPI results computed using cubic components are displayed. However, TPI results derived with quadratic components exhibited similar performance.

Figure 4.10 is the cubic TPI maximum projection overlaid on CB-mode images. The dynamic range for TPI computation was 20 dB, with $\gamma = 0.5$. Each TPI frame was computed using 13 frames, which was approximately 0.35s. The TPI value in the left channel was nearly zero, whereas the TPI value in the right channel was much higher and increased with the growth of the UCA concentration.

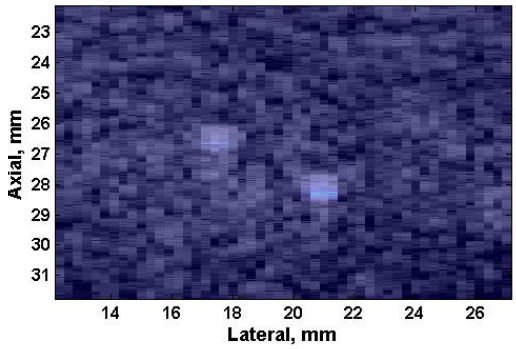

(a) DATA1: Saline Only

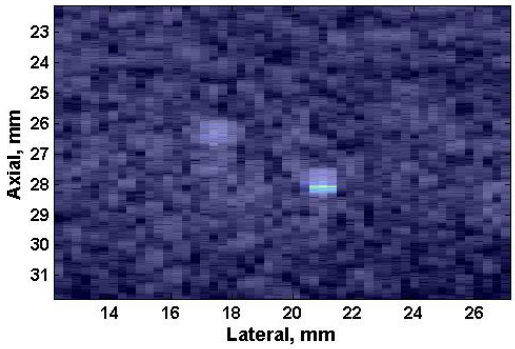

(b) DATA2: UCA Low Concentration

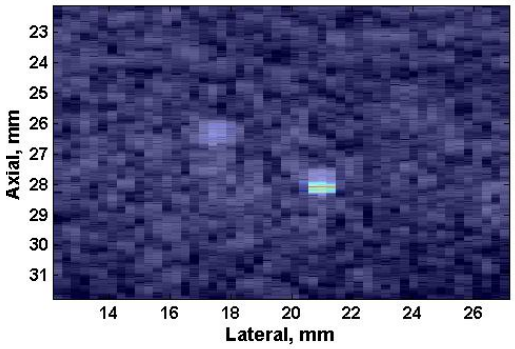

(c) DATA3: UCA High Concentration

Figure 4.10: The cubic TPI maximum projection laid over one frame CB-mode image. The results were computed using the data collected with different UCA concentrations. The dynamic range for the TPI computation was 20dB. The value of γ was 0.5.

To further illustrate the transient nature of the TPI values in the absence and presence of UCA, the time trace of TPI value was computed within a window size of 21×3, which was approximately 0.4×0.9 mm^2 in the axial and lateral directions. This means that, for each frame, $TPI[t]$ was computed according to Equation 4.4 with $(M', N') = (3, 21)$ for all frames. The result is shown in Figure 4.11.

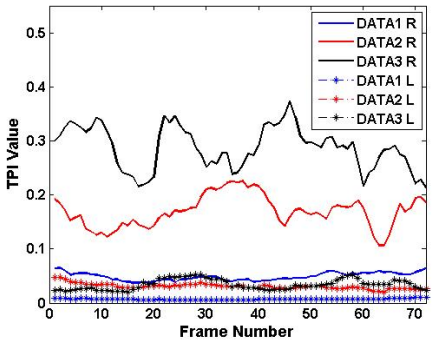

Figure 4.11: Cubic TPI trace over frames. The TPI values were obtained within a window size of 3×21 in the left channel (L) and right channel (R) without $(-*-)$ and with (solid) UCA.

The conclusions drawn from Figures 4.10 and 4.11 can be summarized as follows:

(a) The TPI is able to distinguish UCA activity from high reflection signals from channel walls. In the B-mode images, UCA signal was submerged by the strong backscattered echoes reflected from channel walls. Therefore, the difference between two channels was not detectable. On the other hand, the TPI was able to reward the UCA activity by accounting for its dynamic behavior while suppressing the signal from channel walls. As a result, the TPI raised the UCA activity above the channel wall and tissue component.

(b) The TPI is able to measure microbubble perfusion density qualitatively. The result in Figure 4.11 shows that the TPI value increased with the growth of concentration of UCA solution. Therefore, the TPI is capable of providing a qualitative measure of different microbubble perfusion densities.

The Presence of Tube Wall Echoes: The echogenicities of the signal reflected from tube walls depend on the imaging angle between the target and the imaging plane. In the experimental setup shown in Section 4.1, one can tilt the probe to reduce the strong reflection from channel walls. However, in *in vivo* experiments, high specular reflections are inevitable due to the complexity of vasculature. Therefore, the dynamic behavior becomes the key to detect and capture perfusion activity.

The TPI is designed to capture the perfusion information by accounting for the dynamic behavior of UCA microbubbles under different flow and microflow conditions. The *in vitro* results in this section have shown that the TPI is capable of capturing the UCA activity from surrounding tissues and high specular reflectors and of providing a qualitative measure of microbubble perfusion density.

4.2.3 Temporal Perfusion Index without Tube Wall Echoes Present (Tilted Probe)

UCA Imaging in Phantom: Figure 4.12 is one frame of RF B-mode and PI images of the tissue-mimicking phantom using "TDATA4". The images were displayed using a dynamic range of 25dB. The linear probe was tilted at a small angle until the specular reflection from channel walls disappeared. The data were collected while pumping UCA solution through two channels. The concentrations for the left and right channels were $1:5$ and $1:11$, respectively. It was difficult but possible to detect the two cellulose channels in the RF B-mode image, though, they were much more distinguishable in the PI image, especially for the right channel.

It should be noted that, even though the UCA concentration in the left channel was more than twice that of the right channel, its echogenicity appeared much lower than that from the right channel. This may result from the different angles between the imaging probe orthogonal and the tubes' axes (referred to as the imaging angle). As plotted in Figure 4.13, α and β were the imaging angles between the transmit beam and the axes of the left and right channels, respectively. Under the condition that tube wall reflection was not detectable, the relation between different angles was,

$$\alpha < \beta < 90^{\circ}.$$

Therefore, the transducer captured relatively more reflections from the right channel

than from the left one. As a result, the right channel appeared much brighter, even with lower UCA concentration.

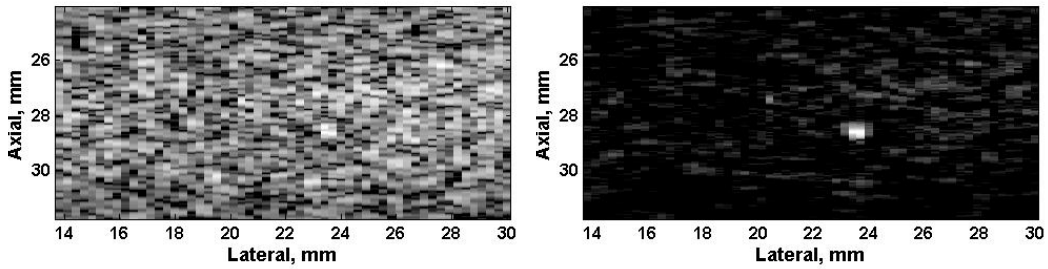

(a) RF B-mode (b) Pulse Inversion

Figure 4.12: One frame of RF B-mode and PI images (25dB) of the tissue-mimicking phantom while pumping UCA solution through the two channels. The concentrations for the left and right channels were $1:5$ and $1:11$, respectively. The LA14-5/38 probe was tilted to reduce specular reflection from channel walls.

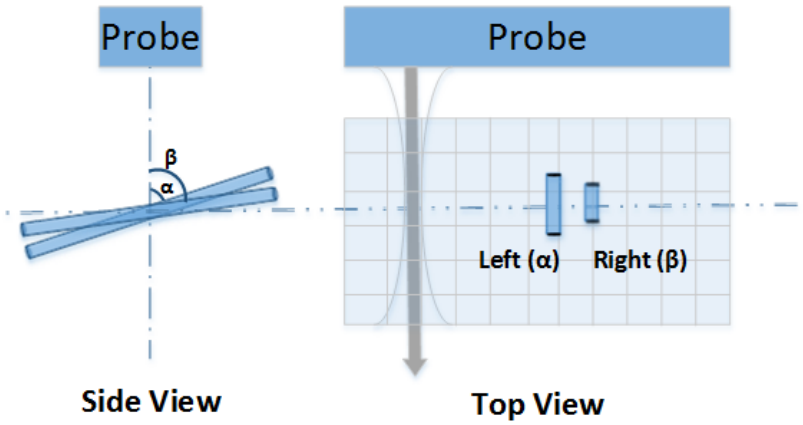

Figure 4.13: A schematic of spatial position between the image probe orthogonal and the axes of the two cellulose channels. The drawing was made to compare the two imaging angles and provide an explanation for the comparison of backscattered signals reflected from two channels. The position may be slightly different from the actual layout.

Volterra Filtering: The parameters to derive the TVF were set as forgetting factor $\lambda = 0.999$ and regularization parameter $\alpha = -0.75$, and it took approximately 500 samples before the filter converged. Figure 4.14 shows QB-mode and CB-mode images produced by the TVF using the same RF frame shown in Figure 4.12. The location of the right channel was clearly visible in both QB-mode and CB-mode images. The signal reflected from the right channel was still stronger than that from the left channel.

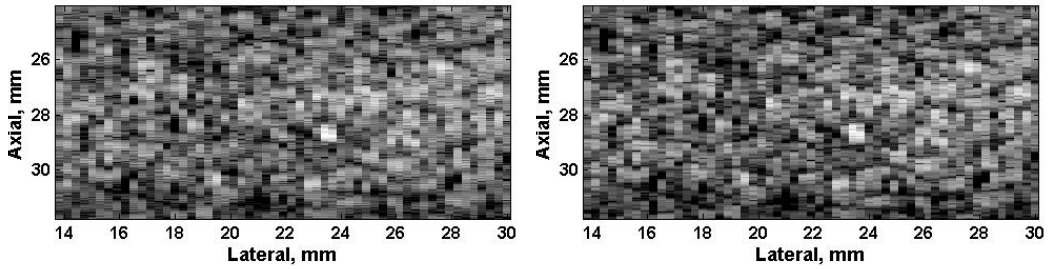

(a) Quadratic Component (b) Cubic Component

Figure 4.14: QB-mode (42 dB) and CB-mode (60 dB) images obtained from the RF data used to generate Figure. 4.12.

Temporal Perfusion Index: In this section, only TPI results computed using quadratic components are displayed. However, the results computed using cubic components exhibited similar performance.

Figure 4.15 is the quadratic TPI maximum projection laid over QB-mode images. The dynamic range for TPI computation was 53 dB, with $\gamma = 1$. Each TPI frame was computed using 7 frames, approximately 0.19s. The TPI values computed in the right channel using different data sets were relatively the same. On the other hand, the TPI values computed in the left channel were different. Higher TPI value was associated with higher UCA concentration.

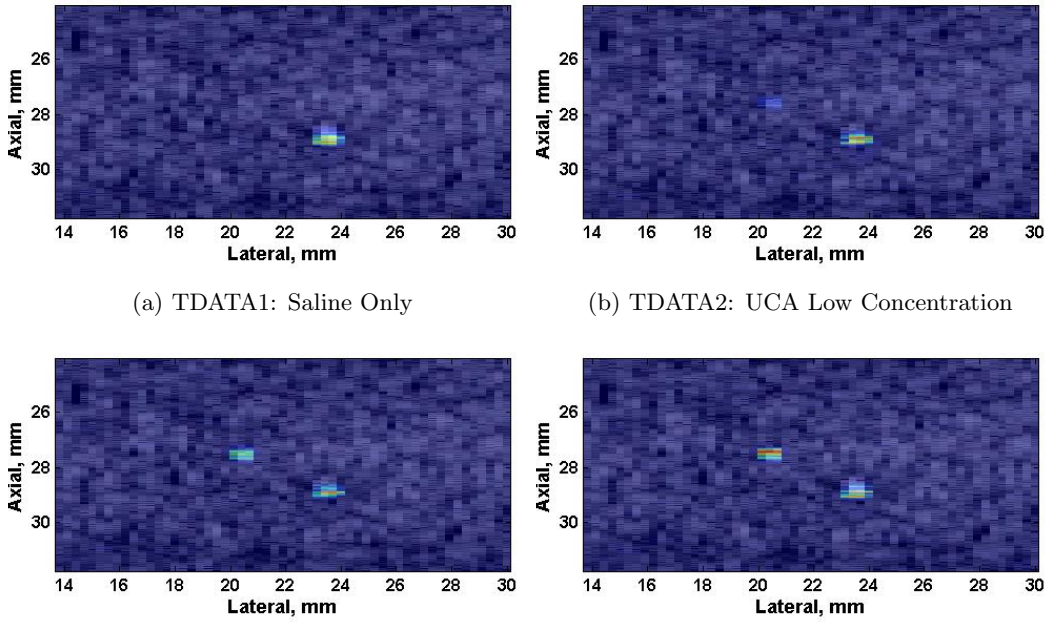

(a) TDATA1: Saline Only

(b) TDATA2: UCA Low Concentration

(c) TDATA3: UCA Medium Concentration

(d) TDATA4: UCA High Concentration

Figure 4.15: The quadratic TPI maximum projection laid over QB-mode images. The results were computed using the data collected with different UCA concentrations. The dynamic range for the TPI computation was 53dB. The value of γ was 1.

To better demonstrate the relationship between the TPI value and UCA concentration, the time trace of TPI value was computed within a window size of 21×3, which was approximately 400×900 μm^2 in the axial and lateral directions. Therefore, $TPI[t]$ was computed according to Equation 4.4 with $(M', N') = (3, 21)$ for all frames. The result is plotted in Figure 4.16.

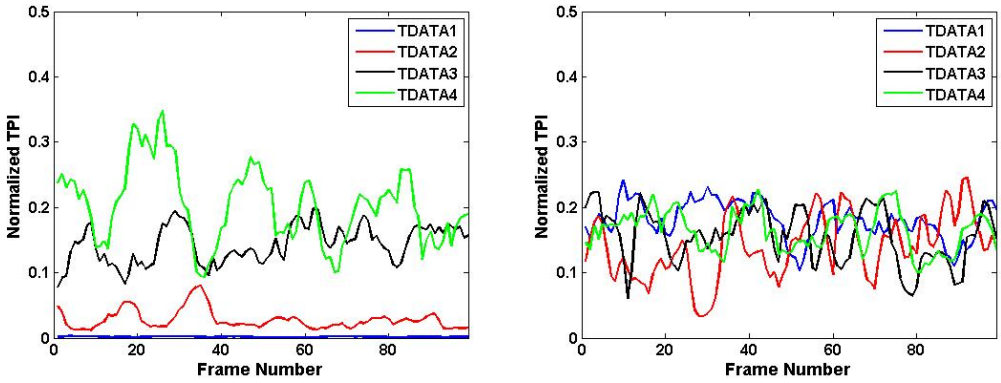

(a) Left Channel (b) Right Channel

Figure 4.16: Quadratic TPI trace over frames. The TPI values were obtained within a window size of 21×3 in the left channel and right channel with different UCA concentrations.

The observations from Figures 4.15 and 4.16 can be summarized as follows:

(a) The TPI is able to qualitatively measure microbubble perfusion density within the same data acquisition. For example, the UCA concentration is lower in the left channel than that in the right channel when acquiring "TDATA2". As a result, the TPI value computed in the left channel was smaller than that in the right channel (Figure 4.15b). Similarly, the UCA concentration was higher in the left channel when acquiring "TDATA4". Therefore, the TPI value computed in the left channel region was larger (Figure 4.15d).

(b) The TPI is able to qualitatively measure microbubble perfusion density between different data acquisitions. For instance, the UCA concentration in the right channel was the same during the whole experimental procedure. As a result, the TPI values computed in the right channel using four different data sets were relatively the same, with an average value of approximately 0.15 (Figure 4.16b). On the other hand, the UCA concentration in the left channel was different. Therefore, the TPI values computed in the left channel using different data sets were different. The TPI exhibited higher value with larger UCA concentration (Figure 4.16a).

(c) The TPI is not sensitive to the imaging angle between the imaging plane and the channels' axes. As detailed earlier, B-mode images were sensitive to the imaging angle. The imaging angle can affect the backscattered signals reflected from high reflectors, such as that in Figure 4.12, where the echogenicities from the right channel (with lower concentration) exhibited larger value compared to the left channel. On the other hand, the TPI value, as shown in Figure 4.15d which was plotted using the same data set, exhibited consistency with the UCA concentration regardless of the imaging angle.

Imaging with Different UCA Concentrations: To further illustrate the point that the TPI is a qualitative measure of microbubble perfusion density, the mean and standard deviation of TPI value were computed for the time series, $\{TPI[t]\}_{t=1}^{104}$ at both the left and right channels. The results are summarized in Table 4.3.

Table 4.3: The TPI value (mean ± SD) at different channels

	TDATA1	TDATA2	TDATA3	TDATA4
$Channel(L)$	0.00±0.00	0.03±0.01	0.14±0.03	0.20±0.06
$Channel(R)$	0.18±0.03	0.14±0.05	0.16±0.04	0.16±0.03

One can see the TPI value in the left channel can qualitatively measure different UCA concentrations, and the TPI values in the right channel region was relatively the same due to the constant UCA concentration used. Therefore, the TPI is capable of providing a qualitative measure on microbubble perfusion density.

4.3 Spatial Heterogeneous Perfusion and Flow Imaging with A 6mm-channel Flow Phantom

4.3.1 Experiment Setup

The experiment setup is shown in Figure 4.17. A 6mm channel from a peripheral flow phantom model 524 (ATS laboratories, Inc., Bridgeport, CT) was used as the imaging

target. A peristaltic pump (Model 77200-60, Cole-Parmer, Vernon Hills, IL) was used to pump water, linear scatters (Sigma Cell Type 20, Sigma-Aldrich, St. Louis, MO), and UCA (Targestar-P, Targeson, San Diego, CA). The solution was stirred by a stirrer (Stirrer/ Hot Plate, Corning, Inc., Corning, NY) during the experiment. This was to make sure the linear scatters and UCA were well dissolved. The imaging system was described in Section 1.3.1.

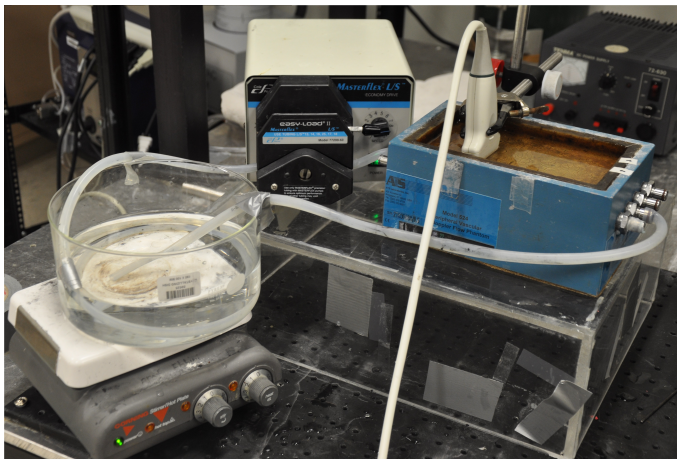

Figure 4.17: The 6mm-channel flow phantom experiment setup.

The linear probe was slightly tilted to reduce the specular reflection from tube walls. Following that, the data acquisition was carried out with the following procedures:

1. The scanner was used in research mode to allow RF data collection.

2. Water was pumped through the 6mm channel using the peristaltic pump at a rate of 90mL/min (and being kept the same for the following steps). RF PI frames were collected. This data set is referred to as "baseline".

3. 1.75g linear scatters were dissolved into 1000mL water. The solution was stirred during the data collection. RF PI frames were collected while the solution was being pumped through. This data set is referred to as "linear scatters".

4. 0.05mL UCA microbubbles were dissolved into the 1000mL solution from step 2. The UCA concentration was 1.5×10^5 microbubbles per mL. The new solution

was pumped through while being stirred. RF PI frames were collected. This data set is referred to as "UCA050".

5. Another 0.05mL of UCA microbubbles were dissolved into the 1000mL solution from step 3. The UCA concentration was 3.0×10^5 microbubbles per mL. RF PI frames were collected when the new solution was being stirred and pumped through the channel. This data set is referred to as "UCA100".

The objective of this experiment was to demonstrate the specificity and sensitivity of spatial heterogeneous perfusion imaging. We used a flow phantom with low UCA concentration to mimic heterogeneous perfusion imaging. UCA microbubbles coming in and out of the imaging slices are quasi random activity both in time and space. When the concentration is low enough to capture the activity from a single bubble or a small cluster of bubbles, the UCA flow within a small region (μm in size) can be considered as UCA perfusion. In Section 4.3.3, we choose five regions with a size of 600×900 μm^2 in the axial and lateral directions to study heterogeneous perfusion imaging.

The data were also used as an example to illustrate how to apply the method detailed in Section 3.2.1 to determine the dynamic range for TPI computation. 143 successive RF PI frames were collected for each data set. The frame rate was approximately 42 fps. The MI was approximately 0.07.

Spatial Resolution and Speckle Statistics: For each imaging mode, the speckle cell size was computed following [53] using a rectangular region with approximate dimensions of 5.6×4.8 mm^2 in the axial and lateral dimensions, respectively. The rectangular speckle region was placed as shown in Figure 4.1. The speckle cell size for this phantom was 0.80 mm laterally and 0.26 mm axially.

UCA Imaging in Phantom: RF B-mode and PI images with a dynamic range of 45dB are shown in Figure 4.18. All images were normalized by the maximum magnitude of the RF data "UCA100". In the baseline image, the echogenicities from the channel were nearly invisible and at the noise level. The backscattered signal was enhanced while pumping linear scatters, but was still 10 to 20dB lower than the tissue signal. Later with the increase of UCA concentration, the echogenicities from the channel increased

and eventually became approximately 10dB stronger than the echogenicities from the surrounding tissue component. All PI images showed suppressed tissue signal but appeared noisier. Nevertheless, a better separation of UCA backscattered signal from the tissue signal was observed for the PI as expected.

4.3.2 Dynamic Range Selection for TPI Computation

As illustrated in Section 3.2.1, the dynamic range is determined by accounting for the variation of PDF over frames. A demonstration of how to apply the method to derive the dynamic range is detailed as follows.

First, determine the region of interest. The imaging target in this experiment was the 6mm channel, and only data acquired within the channel were used to determine the dynamic range. In the Figure 4.18a, the region (221×21 samples, axially and laterally) was highlighted using the white box. After defining the data region, the variance of the PDF over 143 frames was computed for each data set. The result is shown in Figure 4.19.

The observations from Figure 4.19 can be summarized as follows:

1. The variance computed using "baseline" and "linear scatters" was relatively the same, especially for the PI.

2. Larger variance was detected in the data sets acquired with UCA present. The higher the UCA concentration was, the larger the variance was.

3. All variance distributions were unimodal. The magnitude corresponding to the peak variance increased with the growth of the UCA concentration.

The optimal dynamic ranges determined from Figure 4.19 were 30dB and 42dB for raw RF and PI, respectively.

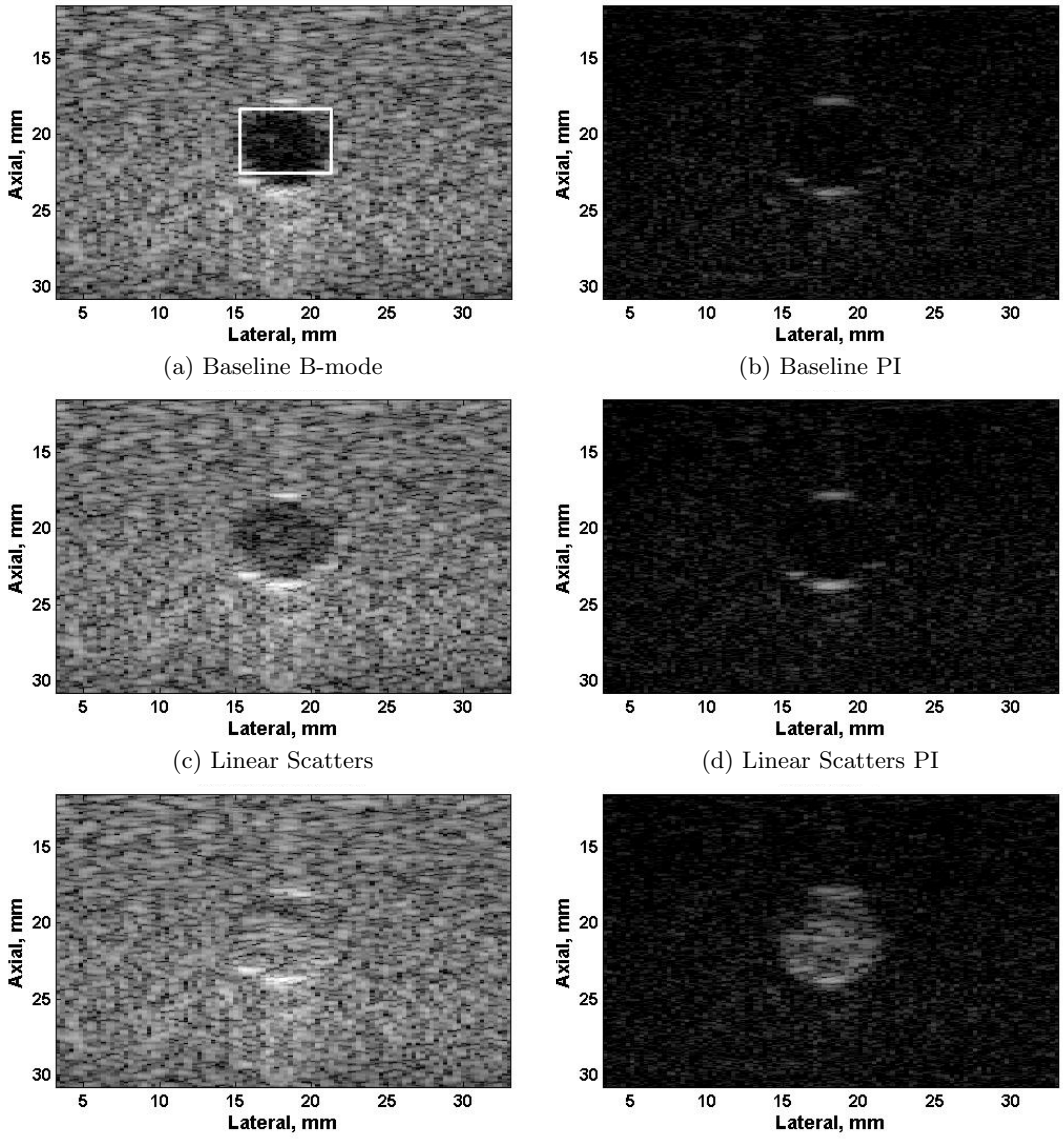

(a) Baseline B-mode

(b) Baseline PI

(c) Linear Scatters

(d) Linear Scatters PI

(e) UCA050

(f) UCA050 PI

Figure 4.18: One frame of RF B-mode and PI images (45 dB) of the flow phantom with the 6mm channel filled with water only, linear scatters and different concentrations of UCA.

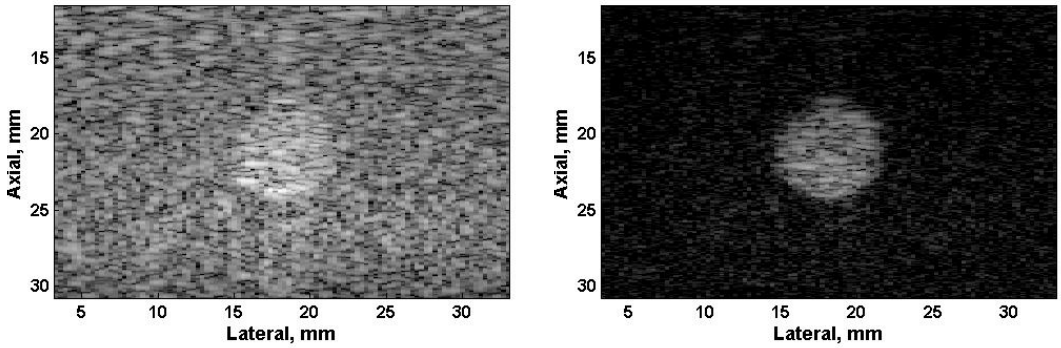

(g) UCA100 (h) UCA100 PI

Figure 4.18: One frame of RF B-mode and PI images (45 dB) of the flow phantom with the 6mm channel filled with water only, linear scatters and different concentrations of UCA.

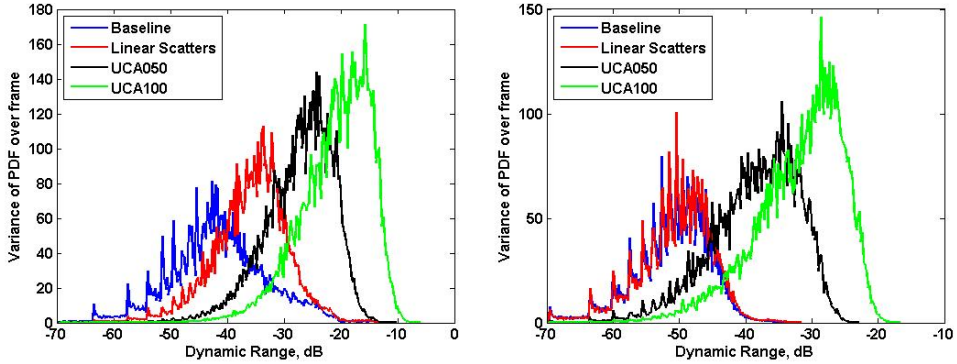

(a) Raw Data (b) Pulse Inversion

Figure 4.19: The variance of PDF over 143 frames. The results were computed using both RF and PI data.

Third-order Volterra Filter: A TVF was derived using one A-line with the presence of UCA from the data set "UCA100". The forgetting factor $\lambda = 0.999$, regularization parameter $\alpha = -0.1$, and the system order is 13. It took 175 samples before the filter converged. Once the filter was derived, it was applied to all frames from all data sets.

Temporal Perfusion Index: The optimal dynamic ranges for linear and nonlinear components were computed using the same procedure. They were 30, 70 and 100dB

for linear, quadratic, and cubic components respectively. Following that, the TPI computation was applied to each component. To save the space, Figure 4.20 only shows the TPI maximum projection computed using cubic components. Each TPI frame was computed using 11 frames, which was approximately 0.26s. The dynamic range for TPI computation was 100dB and $\gamma = 0.5$.

The following conclusions can be drawn from Figure 4.20:

1. The TPI is able to distinguish the UCA activity from water and linear scatters. The TPI value computed using the data acquired with UCA present was much higher than the value computed using the data acquired with water and linear scatters only.

2. The TPI is able to separate the UCA activity from its surrounding tissue component. In the B-mode images shown in Figure 4.18, echogenicities from UCA and tissue were relatively at the same level. However, TPI results showed a much clearer separation between the UCA and tissue component.

3. The TPI is capable of measuring microbubble perfusion density qualitatively. The higher the UCA concentration was, the stronger the UCA activity was and the larger the TPI value was.

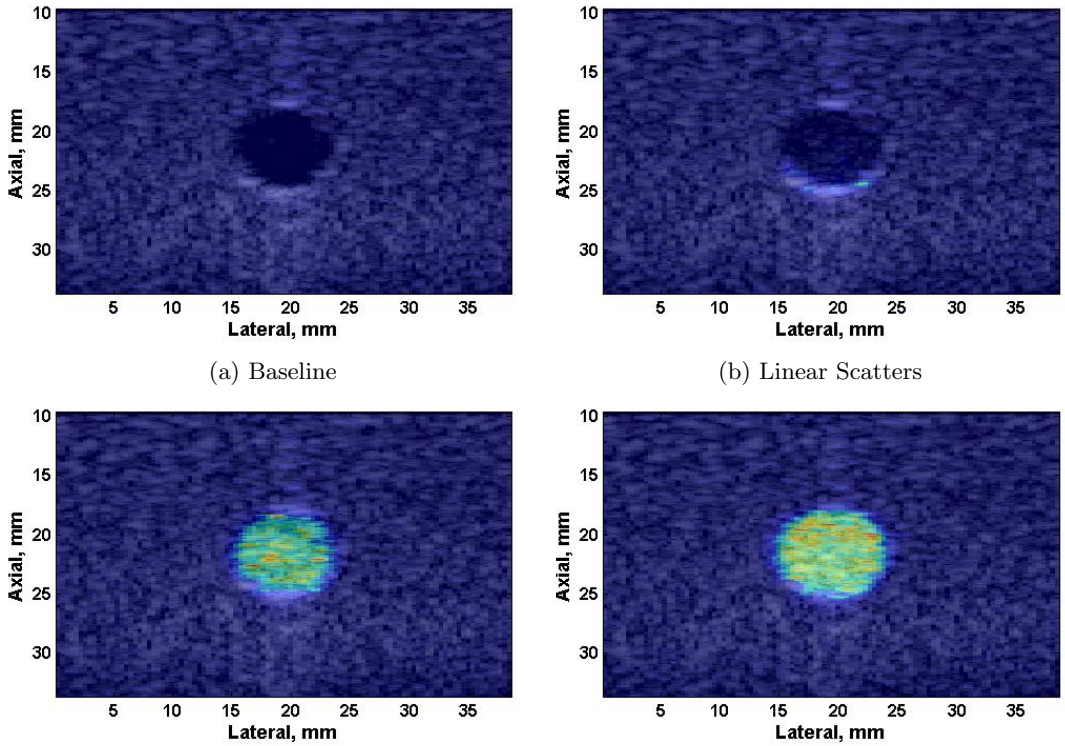

(a) Baseline

(b) Linear Scatters

(c) UCA050

(d) UCA100

Figure 4.20: The cubic TPI maximum projection overlaid on CB-mode images (100dB) with a 6mm channel filled with water, linear scatters only, and different concentrations of UCA. The probe was tilted in the elevation direction to minimize specular echoes from the tube wall. The dynamic range for the TPI computation was 100dB.

Dynamic Range Evaluation: To test whether the derived dynamic range was the optimal choice, normalized cubic TPI with different dynamic ranges (60 to 140dB with a step size of 10dB) were computed. Their mean and standard derivation of TPI value in the region of interest (the white box in Figure 4.18a) are shown in Figure 4.21.

If the dynamic range was too small ($\leq$ 70dB), the TPI value computed using "UCA050" was nearly zero. This means that the UCA activity cannot be preserved with small dynamic range. On the other hand, if the dynamic range was too large ($\geq$ 110dB), the TPI value with UCA present began to decrease and the TPI value with water and linear scatters began to increase, due to the fact that much more noise was

retained. This means that large artifacts can be introduced with large dynamic range. As a result, both large and small dynamic ranges compromise the TPI performance. The optimal dynamic range from Figure 4.21 was approximately 90 to 100 dB, which was consistent with the results derived using our method.

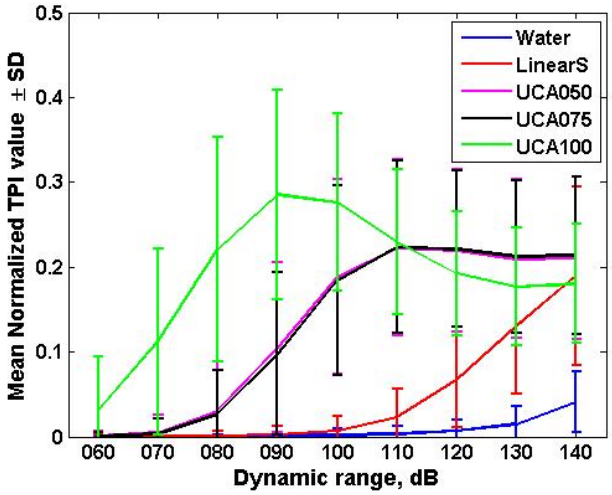

Figure 4.21: The mean and standard derivation of normalized TPI value in the region of interest with different dynamic ranges. All results were calculated using the data within the white window shown in Figure 4.18a.

4.3.3 Spatial Heterogeneous Perfusion and Flow Imaging

As stated earlier, we use flow phantom and UCA solution with a low concentration to mimic perfusion imaging. To present the properties of heterogeneous perfusion and flow imaging, five regions with a size of $(M', N') = (3, 31)$ (600×900 μm^2 in the axial and lateral directions) were selected, as shown in Figure 4.22. For each frame, $P[t]$ was computed according to Equation 4.3 for $t = 1, 2, \ldots, 143$. The graphs in Figure 4.23 show the temporal mean and standard deviation for the time series, $\{P[t]\}_{t=1}^{143}$, computed with data sets "baseline" (blue), "linear scatters" (red), "UCA050" (black), and "UCA100" (green). The computation was applied to the five windows, respectively, and later was also applied to the window in Figure 4.18a with the size of $(M', N') = (21, 221)$. The results are shown in Figure 4.23.

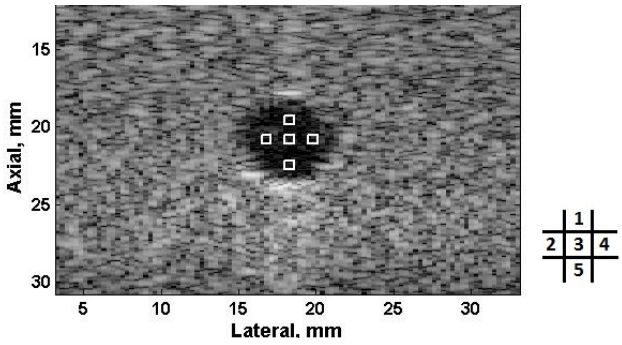

Figure 4.22: One frame B-mode image (45 dB) of the flow phantom with a 6mm channel filled with water only. Five windows with a size of $(M', N') = (3, 31)$ were chosen to demonstrate heterogeneous perfusion imaging. The window number is shown in the lower right corner.

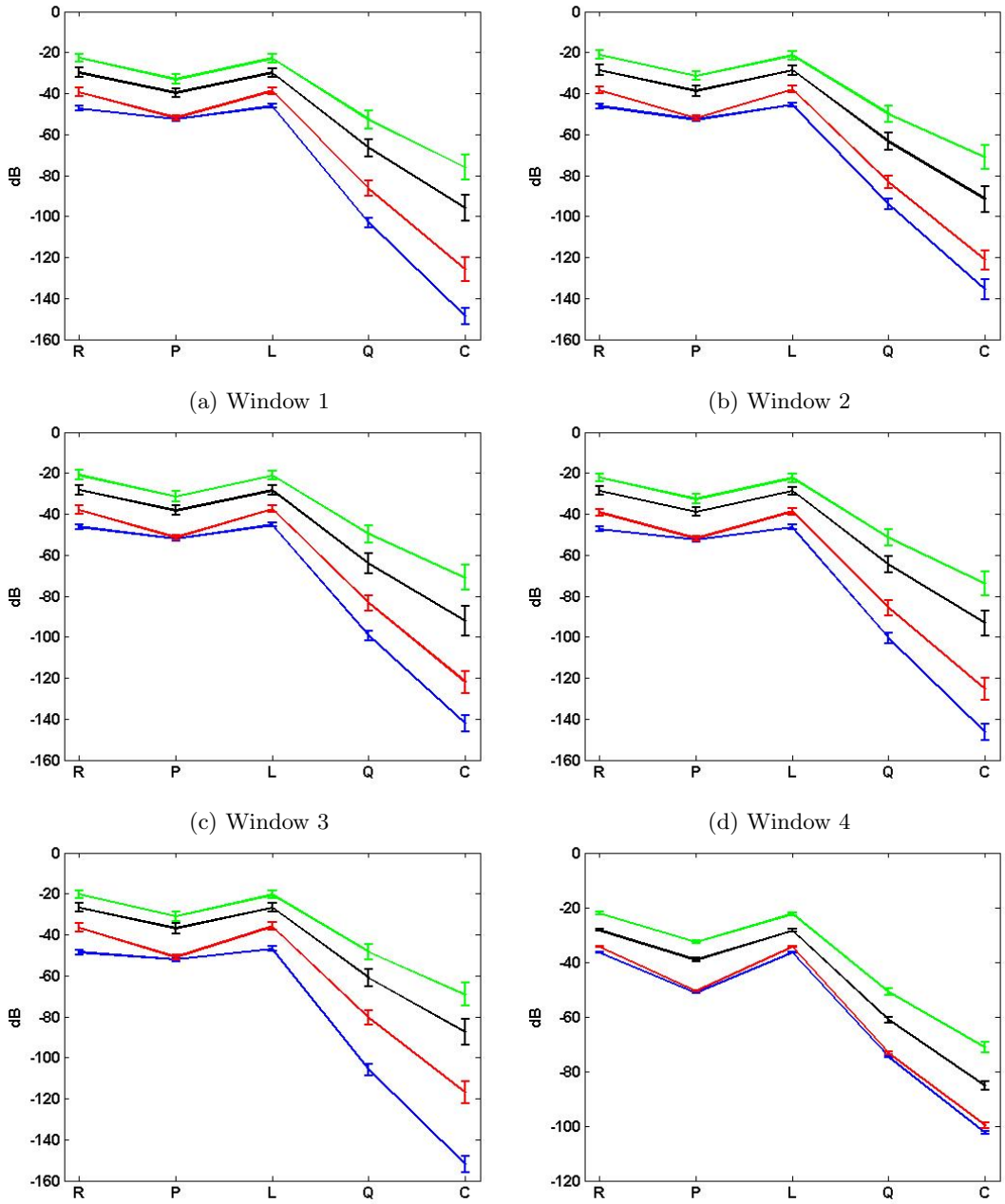

(a) Window 1

(b) Window 2

(c) Window 3

(d) Window 4

(e) Window 5

(f) Window from Figure 4.18a

Figure 4.23: The temporal mean and standard deviation of the power at five window locations in Figure 4.22 (a - e) and the window in Figure 4.18a (f). Baseline: blue, linear scatters: red, UCA050: black, UCA100: green. The y-axis is dB.

The observations from Figure 4.23 can be summarized as follows:

1. The temporal mean and standard derivation of PI power plots from five different windows were relatively the same. However, the plots using other data components exhibited varieties such that the results from window 2 showed larger temporal mean and slightly increased standard derivation.

2. The spatial temporal mean and standard deviation were higher in the presence of UCA compared to water and linear scatters only, regardless of window size and location.

3. Nonlinear components exhibited better separation between the data without and with UCA present in terms of improved temporal mean of the power.

4. The standard derivation of the power exhibited limited improvement between the data without and with UCA present. This is due to the characteristics of flow. This point will be further illustrated using Figure 4.25f which will be shown later.

To further compare the UCA activity at different locations, the average powers computed using the data from five different windows were saved as a data vector. The mean and standard deviation of this vector is shown in Figure 4.24. The standard deviation using PI was nearly zero. This indicates that the average power values computed using PI at different locations were relatively the same. On the other hand, the average power computed using other components, especially nonlinear ones, had much larger standard deviation due to the heterogeneous perfusion property. This is consistent with the result shown in Figure 4.23. Therefore, nonlinear components can preserve heterogeneous perfusion property, while PI cannot achieve this.

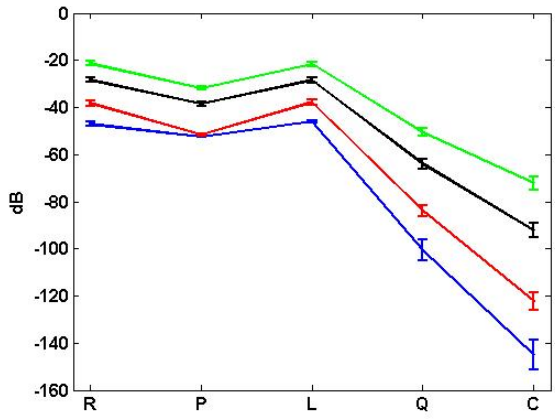

Figure 4.24: The temporal mean and standard deviation of the data vector which was formed of the average powers computed using the data from the five different windows. Baseline: blue, linear scatters: red, UCA050: black, UCA100: green.

Figure 4.25 is the normalized TPI value trace over frames at each window location. The result of $TPI[t]$ for each frame was computed, according to Equation 4.4, for $t = 1, 2, \ldots, 132$. The dynamic ranges for TPI computation using linear, quadratic and cubic components were 30, 70, 100dB, respectively. Each TPI frame was computed using 11 frames and $\gamma = 0.5$. Baseline and linear scatter results are not shown here since their maximum TPI value was smaller than 0.015.

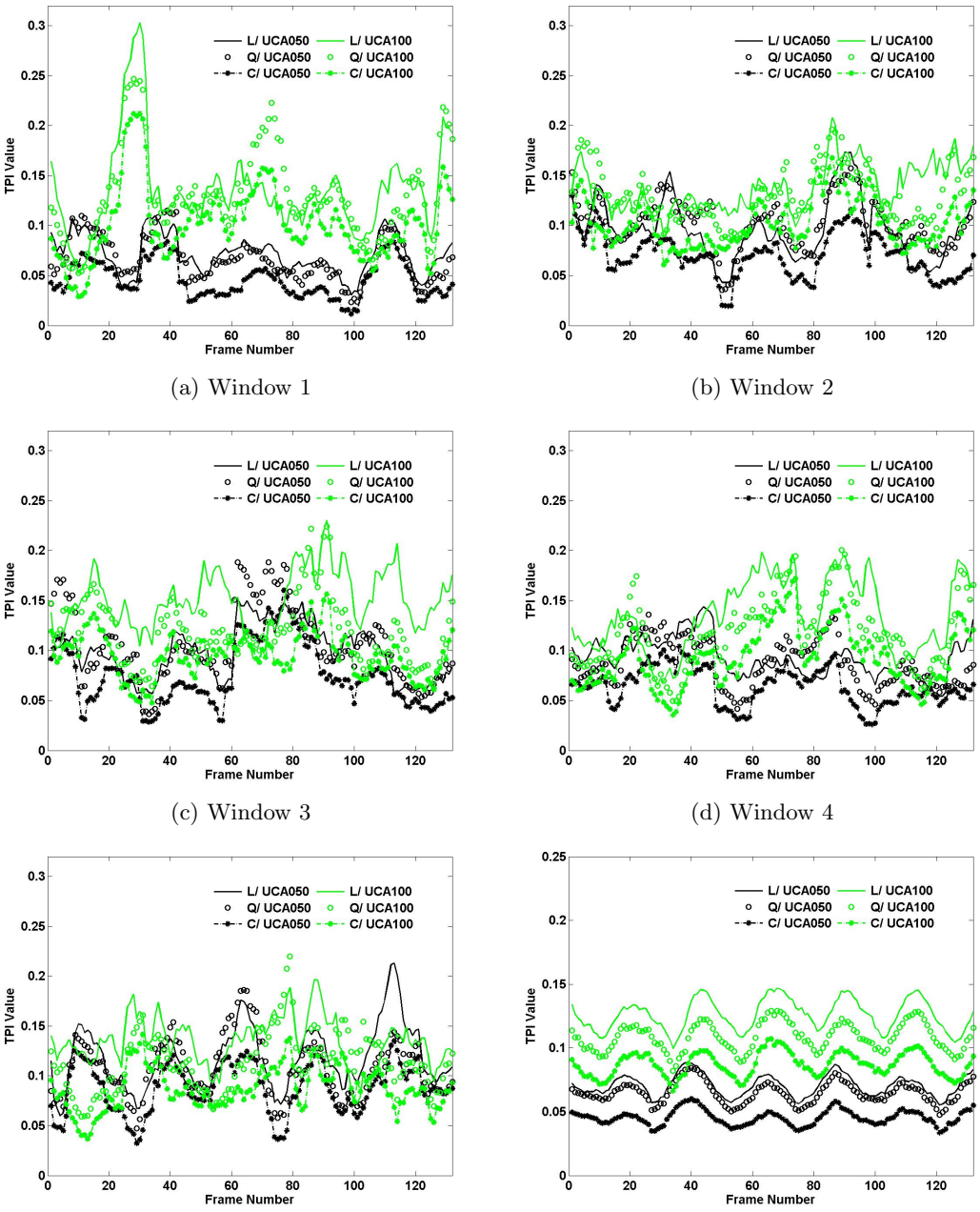

(a) Window 1

(b) Window 2

(c) Window 3

(d) Window 4

(e) Window 5

(f) Window from Figure 4.18a

Figure 4.25: The TPI value trace over frames using five windows shown in Figure 4.22 (a - e) and the window in Figure 4.18a (f). L/: linear component, Q/: quadratic component, C/: cubic component. UCA050: black, UCA100: green. Baseline and linear scatter results are not shown here since their maximum TPI value was smaller than 0.015.

The observations from Figure 4.25 can be summarized as follows:

1. The TPI results computed using all three components were consistent with each other; the TPI value computed with higher UCA concentration was larger than or relatively the same as (in some locations) the TPI value with lower UCA concentration. This further supports the conclusion that the TPI is a qualitative measure of microbubble perfusion density.

2. The TPI can preserve the UCA activity in different regions within the 6mm flow. Therefore, the TPI can preserve heterogeneous perfusion property.

3. The periodic pattern shown in Figure 4.25f was due to the tube motion resulting from pumping. When the pump pushed the flow into the imaging slice the inner diameter of the channel slightly increased. This brought more solution appearing in the slice and resulted in stronger echo reflections from microbubble UCA. On the other hand, when the solution flowed away from the imaging slice, the inner diameter of the channel decreased, which resulted in weaker echo reflections from microbubble UCA. This is a classic mode for flow imaging and it also explained the limited standard derivation separation in Figure 4.23.

Summary of Heterogeneous Perfusion and Flow Imaging: The 6mm-channel phantom experiment provided a validation study of heterogeneous perfusion with ground truth. The performance of the TVF components in terms of preserving heterogeneous perfusion property was improved when compared to the PI.

The TPI can preserve UCA activity and separate them from surrounding tissue component. The TPI images showed a clear distinction between the UCA activity and signals reflected from water, linear scatters, and the tissue component. The TPI also exhibits sensitivity to heterogeneous perfusion imaging and can be used to provide a qualitative measurement of microbubble perfusion density in heterogeneous perfusion regions.

To summarize, TVF and TPI have and sensitivity to heterogeneous perfusion imaging and provide a qualitative measure of microbubble perfusion density.

4.4 A Preliminary Study of *In Vitro* Combined Flow and Microflow Imaging

Simultaneously detecting perfusion at the capillary level and flow in the artery become an emerging topic in medical ultrasound imaging research due to its important clinical applications such as vasa vasorum imaging for diagnosis and treatment of atherosclerosis. However, this area remains a challenge in ultrasound imaging. The reason is that the methods suitable for imaging perfusion and flow are different and they are not compatible with each other. Doppler imaging is a standard method to image flow but it does not have the specificity and sensitivity for perfusion imaging. On the other hand, nonlinear methods such as PI has enhanced specificity and sensitivity to perfusion but are not capable of depicting large vascular structures [33]. However, the PI shows limited imaging spatial specificity for realtime high-speed perfusion due to its sensitivity to motion.

The preliminary study on combined flow and perfusion imaging was carried out on a tissue-mimicking phantom with a 200μm cellulose channel and a 9.525mm wall-free channel. The two channels were at the same axial depth but 3mm apart in the lateral direction. The imaging system was described in Section 1.3.1. The RF and PI frames were collected using the LA14-5/38 imaging probe when saline and UCA were pumped through the cellulose channel at a flow rate of 6 mL/hour and the flow channel at a flow rate of 90 mL/min. No tube signals were observed under the B-mode image. The speckle cell size was computed as 0.75 mm laterally and 0.20 mm axially.

Figure 4.26 shows the B-mode, PI, QB-mode, and CB-mode images of tissue-mimicking phantom while pumping saline and UCA through both channels. The dynamic range was 50dB for all components, with the 0-dB level determined by the maximum magnitude echo data from the two channels with UCA present. Quadratic and cubic components were the outputs of a TVF which was derived from one A-line with UCA present. The initial parameters to derive the TVF were set as system order $m = 15$, forgetting factor $\lambda = 0.999$, and regularization parameter $\alpha = -0.1$.

The results showed the sensitivity and specificity to image perfusion and flow simultaneously using a clinical transducer. QB-mode and CB-mode images exhibited higher specificity to perfusion imaging than PI. On the other hand, PI delineated a

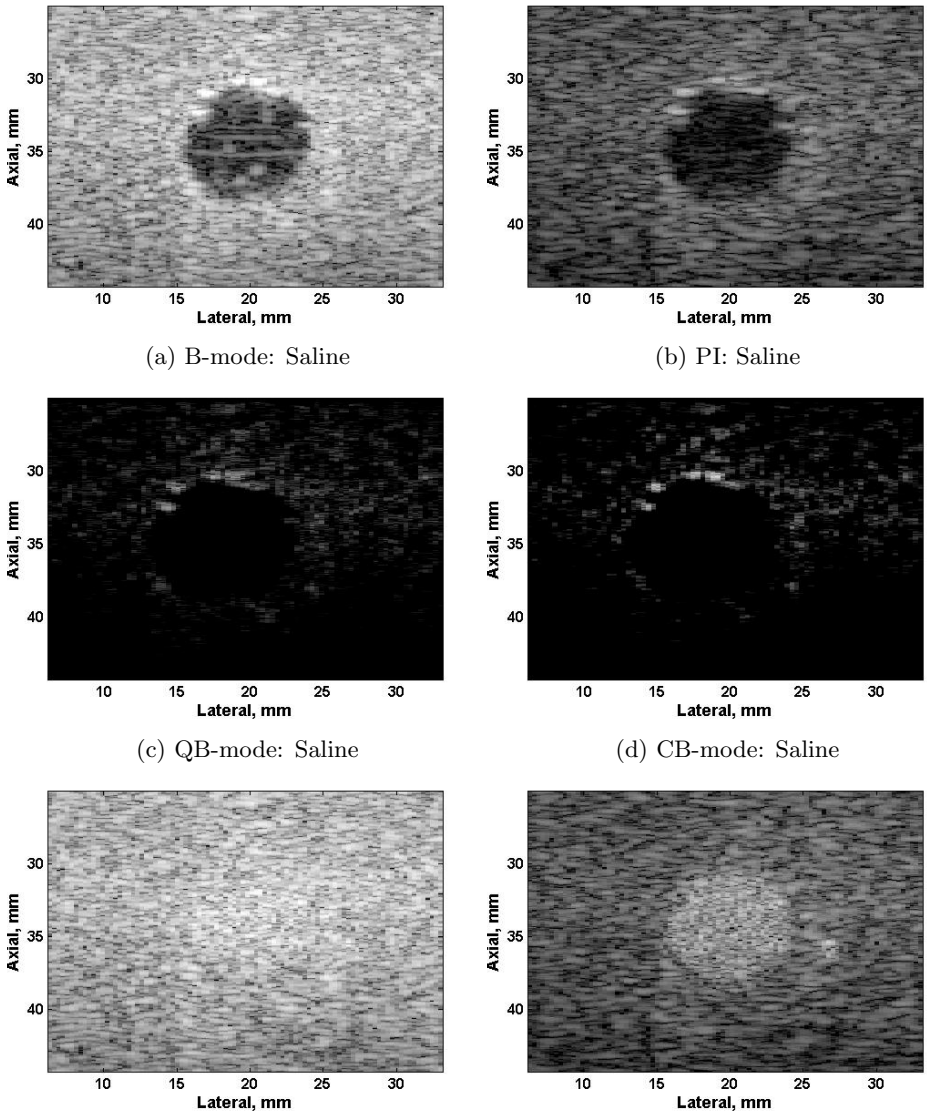

(a) B-mode: Saline

(b) PI: Saline

(c) QB-mode: Saline

(d) CB-mode: Saline

(e) B-mode: UCA

(f) PI: UCA

Figure 4.26: B-mode and PI, QB-mode and CB-mode (50 dB) images of the tissue-mimicking phantom while pumping saline (a - d) and UCA through both channels. The LA14-5/38 probe was slightly tilted to minimize the specular reflection from the tube.

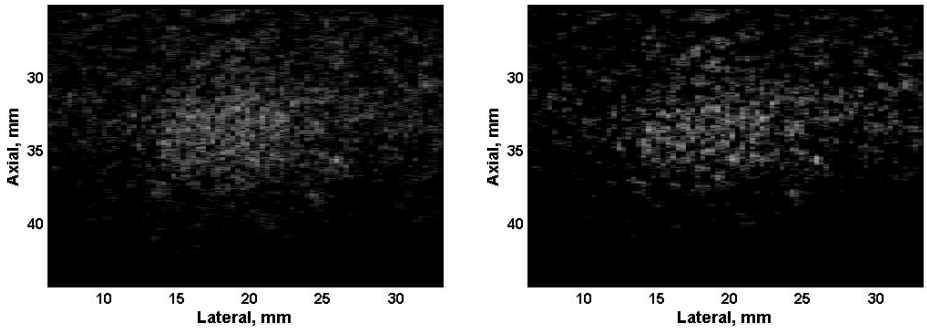

(g) QB-mode: UCA (h) CB-mode: UCA

Figure 4.26: B-mode and PI, QB-mode and CB-mode (50 dB) images of the tissue-mimicking phantom while pumping saline (a - d) and UCA through both channels. The LA14-5/38 probe was slightly tilted to minimize the specular reflection from the tube.

clearer boundary of the flow channel. The combination of the two nonlinear methods may improve the imaging quality of combined flow and perfusion simultaneously. This study would make a worthwhile contribution to flow and perfusion imaging and is recommended for the future study.

4.5 A Preliminary Study of *In Vitro* Longitudinal Perfusion Imaging

As mentioned in Chapter 3, microbubble UCA perfusion also exhibits dynamic behavior due to pulsation and blood circulation. When microbubbles enter and leave the imaging slice within the microflow, each frame represents an independent "UCA event". To further illustrate the concept of the UCA event, a preliminary study of *in vitro* longitudinal perfusion imaging was done on the same tissue-mimicking phantom as the one shown in Section 4.4. The imaging target in this experiment was the 200μm cellulose channel only. The RF PI frames were acquired while pumping UCA solution through the cellulose channel using the LA14-5/38 imaging probe. The imaging system was described in Section 1.3.1. The flow rate of UCA solution inside the channel was 6 mL/hour. The probe was tilted until no tube wall signals were observed under the B-mode image.

Figure 4.27 shows the B-mode, PI, QB-mode, and CB-mode (35dB) images while

pumping UCA through the microchannel at two different time stamps. The image of '33rd Frame" was collected 0.0166s later than the image of "32nd Frame". The quadratic and cubic components were the outputs of a TVF which was derived from one RF A-line with UCA present. The initialization parameters to derive the TVF were set as $m = 15$, forgetting factor $\lambda = 0.999$, and regularization parameter $\alpha = -0.5$. The images were normalized by the maximum absolute value of echo data from the microchannel with UCA present.

In the images shown in Figure 4.27, UCA activity was clearly observed in the center of the images at both frames. The difference between two PI image was indistinguishable. On the other hand, the change of UCA microflow at different frames was visible in both QB-mode and CB-mode images. Take CB-mode images as an example. At 32nd frame, a small cluster of UCA reflectors were detected at a location of 34mm axially and 33mm laterally. Due to the micropump pushing, later at 33rd frame, a new group of UCA microbubbles arrived, exhibiting different echogenicities and behaviors. Meanwhile, the old cluster of reflectors flowed forward. Various individual or clusters of microbubbles were involved at different frames. The UCA behavior at each frame was referred to as an individual UCA event.

Moreover, QB-mode and CB-mode images exhibited better performance than PI in terms of improved sensitivity and specificity to different UCA events and heterogeneous perfusion imaging. Moreover, QB-mode, CB-mode, and PI images showed enhanced sensitivity to perfusion imaging than RF B-mode images.

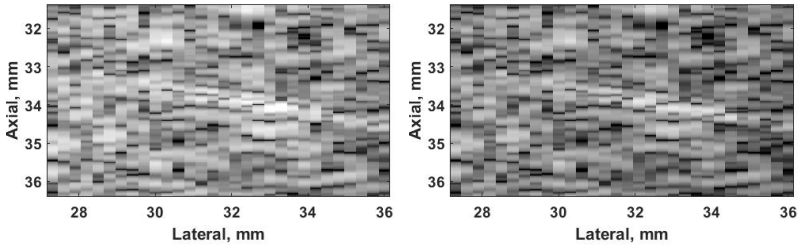

(a) B-mode: 32nd Frame

(b) B-mode: 33rd Frame

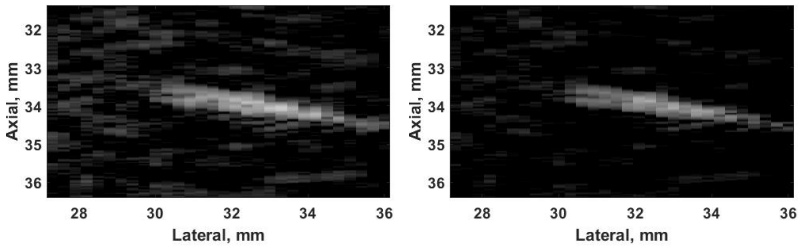

(c) PI: 32nd Frame

(d) PI: 33rd Frame

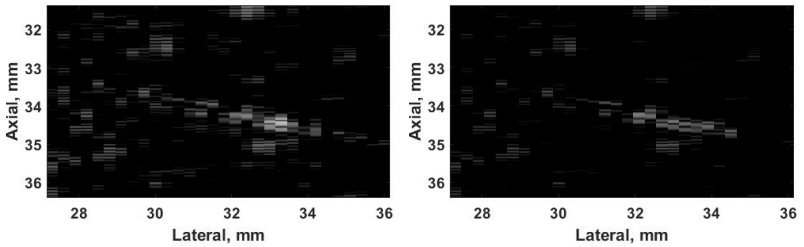

(e) QB-mode: 32nd Frame

(f) QB-mode: 33rd Frame

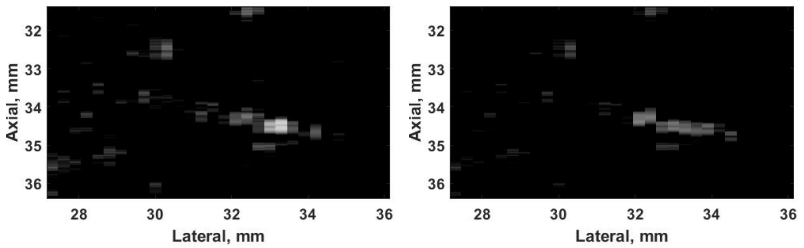

(g) CB-mode: 32nd Frame

(h) CB-mode: 33rd Frame

Figure 4.27: B-mode, PI, QB-mode, and CB-mode (35 dB) images of the tissue-mimicking phantom while pumping UCA through a microflow channel. The LA14-5/38 probe was slightly tilted to minimize the specular reflection from the tube.

Chapter 5

Contrast-enhanced Tumor Perfusion Imaging

5.0 Introduction: Heterogeneous Tumor Perfusion Imaging

Tumor vasculature provides an important factor for tumor therapy and treatment due to its ability to access to blood-borne anticancer agents and to provide an intact vascular supply for the survival of most cells [55]. Accurate perfusion imaging techniques are required during tumor treatment to provide feedback and guidance [56] to confine the treatment location and reduce the error.

Tumor perfusion imaging is one of the most significant applications of perfusion imaging. In this chapter, the *in vivo* heterogeneous tumor perfusion imaging is presented. The data were acquired on a LNCaP tumor with a clinical transducer.

5.1 *In vivo* Heterogeneous Tumor Perfusion Imaging

5.1.1 Experiment Setup

The imaging data were acquired from the *in vivo* target under IACUC-approved protocol. The target was a LNCaP tumor implanted in the hind limb of a Copenhagen rat (approx. 300 grams). The objective of this experiment was to demonstrate the ability

of VFs to detect the UCA nonlinearities in a tumor with nonhomogeneous vasculature and the sensitivity and specificity of TPI to heterogeneous perfusion imaging. The HST15-8/20 probe was used for this experiment. Its center frequency was 10 MHz, and the focus beams were at 18mm. The MI at the focus was less than 0.08.

The animal was anesthetized using Ketamine and Xylazine and placed in a prone position. A viscous acoustic standoff pad (Civco Medical Instruments, Calona, IA) was placed between the tumor and imaging probe to improve the image quality at the skin surface since the tumor was subcutaneous. Imaging settings were optimized in clinical mode before switching the scanner to research mode. Care was taken to avoid saturation and clipping of RF data.

MicroMarker UCA (Visual Sonics, Toronto, ON Canada) was used for the *in vivo* experiments. MicroMarker, a lipid encapsulated mixture of nitrogen and perfluorobutane microbubble, is a non-targeted contrast agent with a median diameter in the range of 2.3 - 2.9 μm.

The imaging system was described in Section 1.3.1. RF data collection started a few seconds before the injection of the UCA in the rat. After the baseline data were collected, a bolus injection of UCA (.75 mL) was given and another set of RF data was collected with the contrast present. Care was taken to bring the imaging probe back to the same position as that of pre-injection.

5.1.2 UCA Imaging

Figure 5.1 shows grayscale images of the LNCaP tumor in the hind limb of a Copenhagen rat without (left) and with (right) UCA in B-mode (55 dB). The dynamic range was chosen based on the low-echogenicity region in the center of the tumor (noise floor) with reference to the specular echoes from the skin (0 dB). For B-mode, the average echogenicity of this region was approximately -50 dB and the dynamic range was set at 55 dB.

A subtle but appreciable difference in the echogenicity of the tumor was established after UCA injection. The changes were even more pronounced when reviewing the sequence of frames in Cine loop. For example, the lower left quadrant of the tumor showed significant increase in echogenicity after UCA injection with pronounced dynamic changes from frame to frame, indicating high microbubble perfusion density.

The center of the tumor maintained its low echogenicity, but we observed sporadic localized changes consistent with microbubble flow in isolated vessels. This indicated a low-perfusion region with microflow conditions. The right side of the tumor maintained its low echogenicity throughout, indicating a low or no perfusion region. The sensitivity to UCA was also clear in the high-echogenicity tissue regions surrounding the tumor.

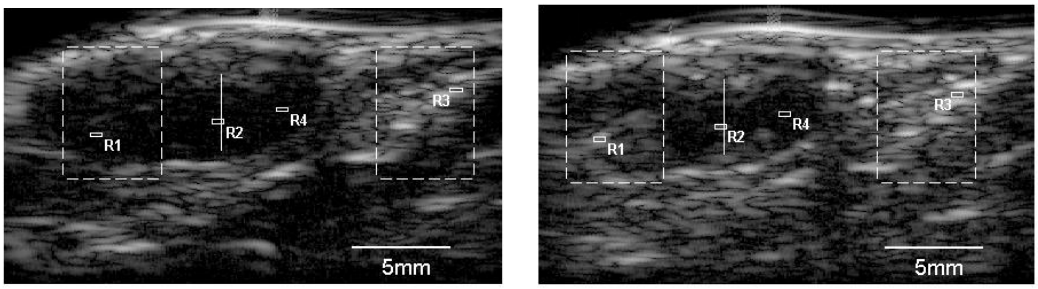

Figure 5.1: Grayscale images (55 dB) of the tumor and the surrounding tissue without (left) and with UCA. The effect of the UCA on the echogenicity in B-mode is subtle but evident, especially in hyperechoic regions.

5.1.3 Third-order Volterra Filter

A TVF was derived using with the parameters set as forgetting factor $\lambda = 0.999$ and regularization parameter $\alpha = -0.4$, and it took approximately 500 samples before the filter converged. The filter was later applied to the whole data sets. Linear, quadratic, and cubic components were acquired.

Figure 5.2 shows grayscale images of the LNCaP tumor without (left) and with UCA (right) in QB-mode (120 dB) and CB=mode (185 dB). The dynamic ranges were determined by the same criteria. For QB-mode and CB-mode, the echogenicity levels were -115 dB and -180 dB and the corresponding dynamic ranges were set to 120 dB and 185 dB, respectively.

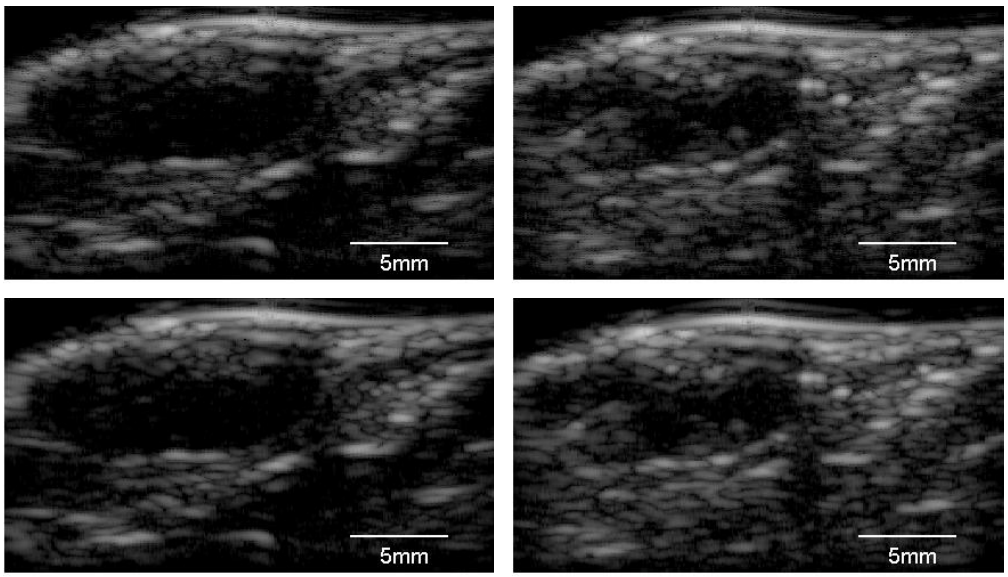

Figure 5.2: Grayscale images of the tumor and surrounding tissues without (left) and with (right) UCA. Top: QB-mode (120 dB). Bottom: CB-mode (185 dB).

Figure 5.3 shows examples of power spectral density representations from the two regions in Figure 5.1 (large boxes with dashed edge lines). The box on the left contained mostly tumor tissue that exhibited heterogeneous echogenicity distribution. The box on the right was completely within normal tissues with more homogeneous echogenicity. Figure 5.3(a) shows the average normalized PSDs (W/Hz) for the VF filter components in the normal tissue region without and with UCA. For the linear components, the differences in the PSDs without and with UCA were subtle. On the other hand, the quadratic and cubic components in the presence of UCA showed marked increase over a wide range of frequencies. The situation was similar in the region containing tumor tissues with heterogeneous echogenicity as seen in Figure 5.3(b), but the relative enhancements in the quadratic and cubic components were less. Figure 5.3(c) illustrates the quality of signal prediction achieved by the VF by plotting the PSDs of the RF data (Input) and the VF components from the tissue region in the presence of UCA. As expected, the linear component was dominant and its PSD almost matched that of the input. The quadratic and cubic components were approximately 30 and 50 dB below the linear, respectively.

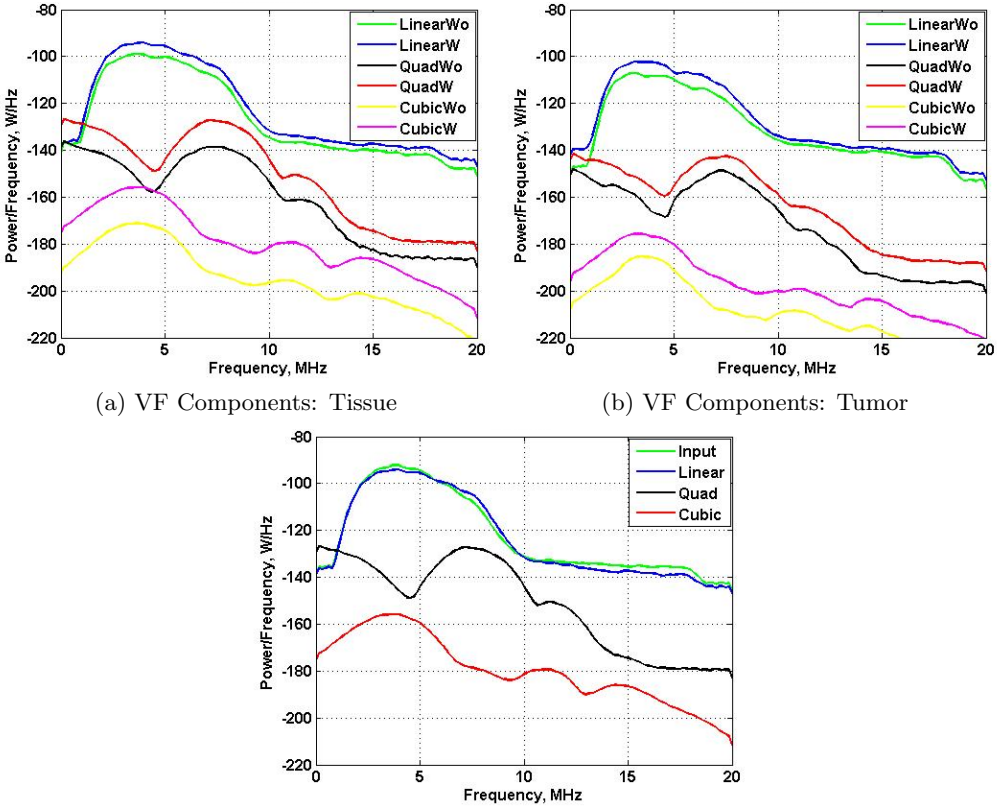

(a) VF Components: Tissue

(b) VF Components: Tumor

(c) VF Components: Tissue with UCA

Figure 5.3: Normalized power spectral density (W/Hz) for the VF components: (a) In the tissue region within the dashed box on the right (Figure 5.2). (b) In the tumor region within the dashed box on the left (Figure 5.2). (c) The PSDs of the VF filter components in the tissue region plotted together with the PSD of the input RF data. The linear component with UCA exhibited spectral broadening and slight increase in power compared to the linear component without UCA. These effects were more pronounced for the quadratic and cubic components. Furthermore, the enhancement levels were different in tissue and tumor regions.

Figure 5.4 shows the temporal mean and standard deviation of the power in regions R1, R2, R3 and R4 indicated by the solid boxes in Figure 5.1. The size of each region was $N' \times M' = 13 \times 7$. R1 was located in a well-perfused segment of the tumor while R2 was located in a poorly-perfused segment with isolated microflow. R3 was located in a low-perfused, high-echogenicity segment of the tissue surrounding the tumor. R4 was

located in a low-echogenicity segment of the tumor with no apparent perfusion. The classification of perfusion in each region was based on Cine loop review before and after UCA injection. It should be noted that the locations of the boxes in the images without and with UCA were corrected for small spatial shifts of approximately 1.5 mm laterally and 0.5 mm axially.

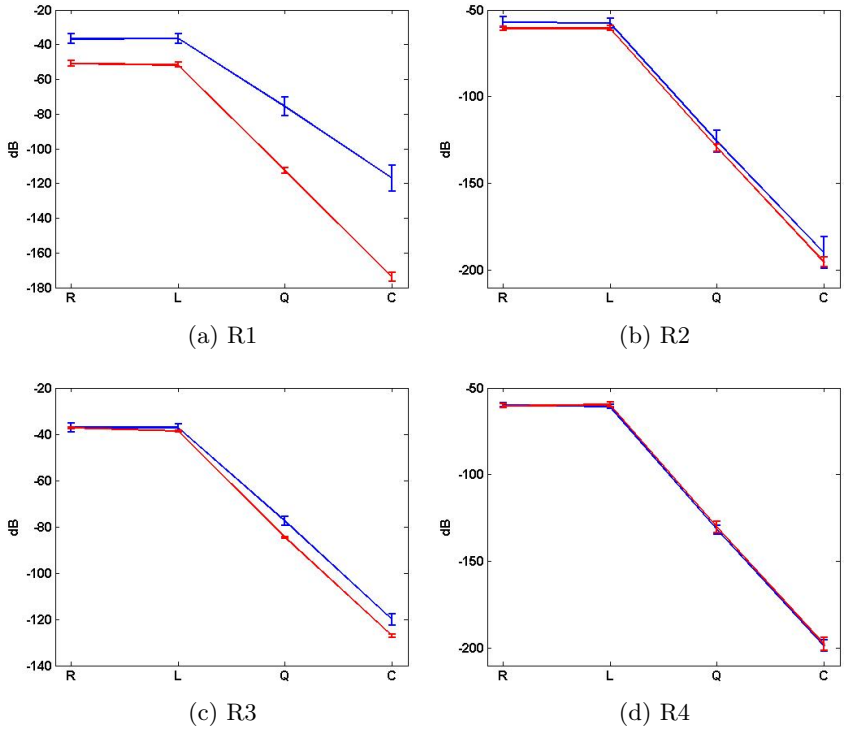

(a) R1 (b) R2

(c) R3 (d) R4

Figure 5.4: Temporal mean and standard derivation (error bars) of the average power in the four representative regions shown in Figure 5.1. Data shown without (red) and with (blue) UCA.

In R1, all image components, showed an increase in the mean power level as well as an increase in standard deviation. This was the expected result in well-perfused regions where the presence of the UCA was observed in B-mode immediately after injection. In R2, the B-mode showed a smaller change in the mean value and a marked increase in standard deviation. In R3, B-mode and LB-mode showed relatively the same mean value before and after UCA injection with a slight increase in the standard deviation.

The nonlinear components showed greater separation in the mean values and a slight increase in the standard deviation after injection. In R4, the statistics were practically the same with or without UCA indicating low or no perfusion in a low scattering region.

A comparison between the echogenicities of Regions 2 & 4 in Figure 5.1 led to an interesting difference that helped to shed some light on the advantages of nonlinear filtering. Note that, in the absence of UCA, both regions had the same values of average power (both mean and standard deviation). In the presence of UCA, R2 exhibited a significant increase in the standard deviation compared to that of R4. In reviewing the imaging frames in Cine loop with UCA, it was clear that an isolated vessel ran through R2 in the axial direction as evidenced by a localized echo moving towards the transducer. To illustrate this point, we show spatio-temporal echogenicity maps (M-mode) for the vertical line segments passing through R2 before (left) and after (right) UCA injection in Figure 5.5. The conventional M-mode images shown on the left were obtained using the RF data from 144 and 160 frames collected before and after UCA injection, respectively. The dB range of [-80,-29] was set with reference to the maximum value used to set the dB range of the B-mode image in Figure 5.1.

In the presence of UCA, the M-mode images in Figure 5.5 revealed an upward movement of blood in a microvessel aligned with the imaging slice. For example, a "microbubble event" appears in Frame 1 at an axial distance of 17.5 mm and moves up to an axial distance of 15.5 before disappearing in Frame 75. The M-mode data shows that the low echogenicity portion within the line segment ([15,17.5] mm) was dominated by clutter and noise components. The noise was responsible to the graininess of the echogenicity values, both spatially and temporally. The clutter produced semi-regular echo components which could have resulted from reverberation and/or beamforming artifacts given the cyst-like nature of this portion of the tumor.

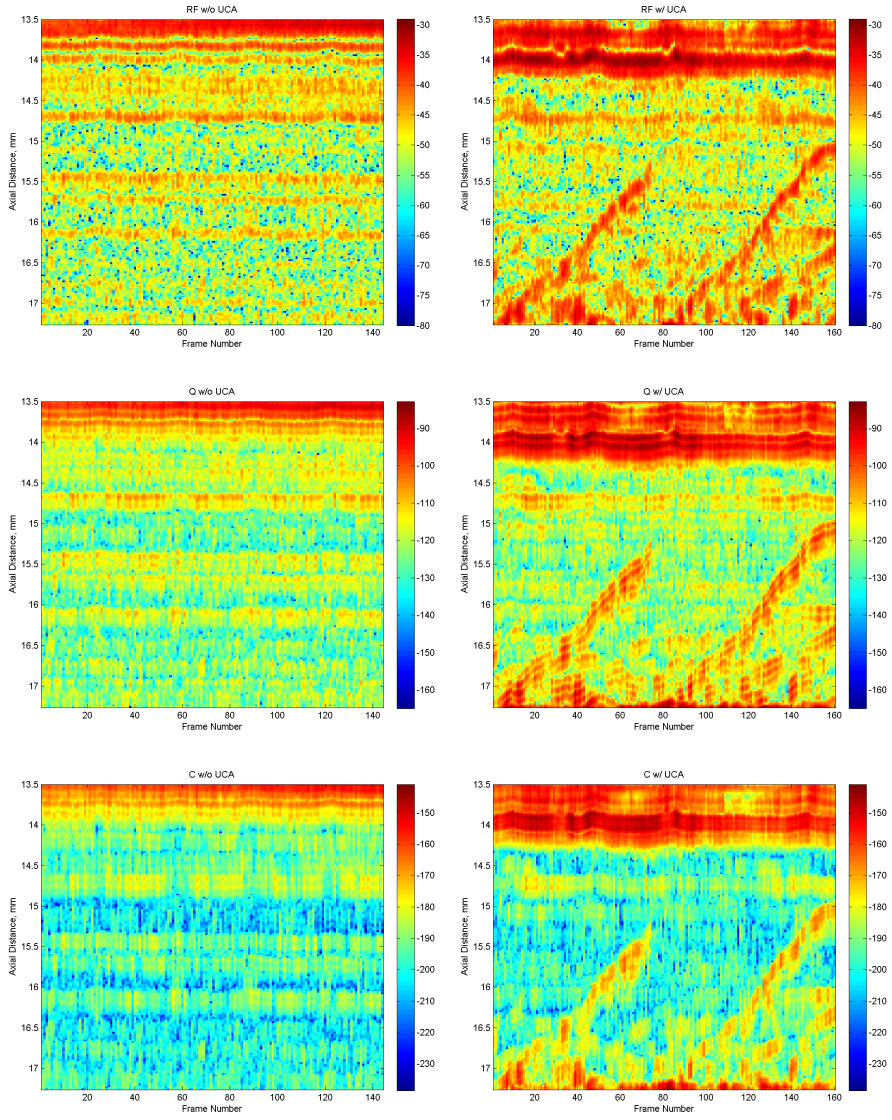

Figure 5.5: Left: Spatio-temporal representation of the echogenicity from the A-line segment indicated by the vertical line in the left image of Figure 5.1. Right: Spatio-temporal representation of the echogenicity from the A-line segment indicated by the vertical line in the right image of Figure 5.1. Top to bottom: RF, quadratic and cubic signals, respectively. Each pair of images without and with UCA was normalized to the same dB scale.

Figure 5.5 also shows the corresponding QM-mode ([-165,-84] dB) and CM-mode ([-238,-142] dB) representations of the echogenicity for the same A-line segments. These showed the same microbubble events, but with significant noise reduction compared to M-mode (evidenced by the absence of the graininess in both components). In addition, QM-mode and CM-mode produced more reduction in clutter components compared to M-mode. For example, M-mode showed persistent clutter patterns at 15.8 and 16.1 mm axially with intensity levels close to those generated by the microbubble event. These clutter patterns were substantially suppressed in QM-mode and CM-mode. The suppression of the noise and other clutter in low scattering regions could be the key to imaging low-level UCA activity in heterogeneously perfused tumors.

5.1.4 Temporal Perfusion Index

Dynamic Range Selection for TPI Computation: As detailed in Section 3.2.1, the dynamic range for TPI computation is determined by the probability distribution function (PDF). Figure 5.6 shows PDF $f(\nu, t)$ of cubic components and its corresponding variance $V(\nu)$ over frames, before (red) and after (blue) the UCA injection. Because of the presence of UCA, the backscattered signal after the injection was improved, and the center of the distribution shifted to the right.

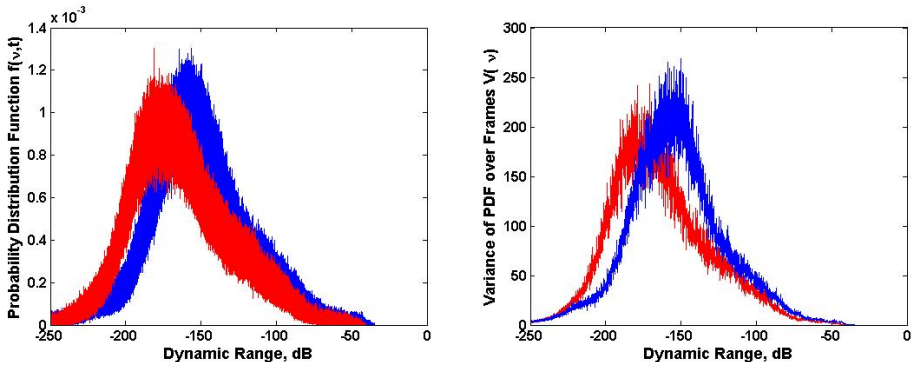

Figure 5.6: The probability distribution function $f(\nu, t)$ and its corresponding variance $V(\nu)$ over frames before (red) and after (blue) the UCA injection. The results were computed using cubic components.

The observations from Figure 5.6 can be summarized as follows:

1. Compared to $f(\nu, t)$, the distributions of $V(\nu)$ exhibited better separation of the data acquired without and with UCA. $V(\nu)$ was more sensitive to the presence of UCA.

2. The variance $V(\nu)$ was enhanced after UCA injection for $\nu \geq -165$ dB. The enhancement resulted from the UCA activity.

3. The variance $V(\nu)$ was reduced after UCA injection for $\nu \leq -165$ dB, which was relatively at the noise level.

It can be determined from Figure 5.6 that -165 dB was a reasonable threshold to preserve the UCA activity while suppressing the noise to the greatest extent. Therefore, the dynamic range for TPI computation was determined to be 165 dB.

Temporal Perfusion Index: Figure 5.7 is linear (top), quadratic (center), and cubic (bottom) maximum TPI projections overlaid on B-mode images, without (left) and with (right) UCA. The dynamic ranges for TPI computation were 45, 105, and 165dB, respectively. The nonzero TPI values before the UCA injection reflect the sensitivity of the estimator to tissue motion and/or noise variation depending on the local tissue echogenicity. This is inevitable for any dynamic measurement based on tissue echogenicity. In the presence of UCA, however, the TPI values were significantly higher throughout the tissue region and within parts of the tumor as seen in the images. The result clearly shows the TPI distribution within and outside the tumor with relatively high values at different locations, illustrating the sporadic nature of the UCA-induced echogenicity change. Moreover, the presence of high-value TPI captured by different components showed consistency with each other.

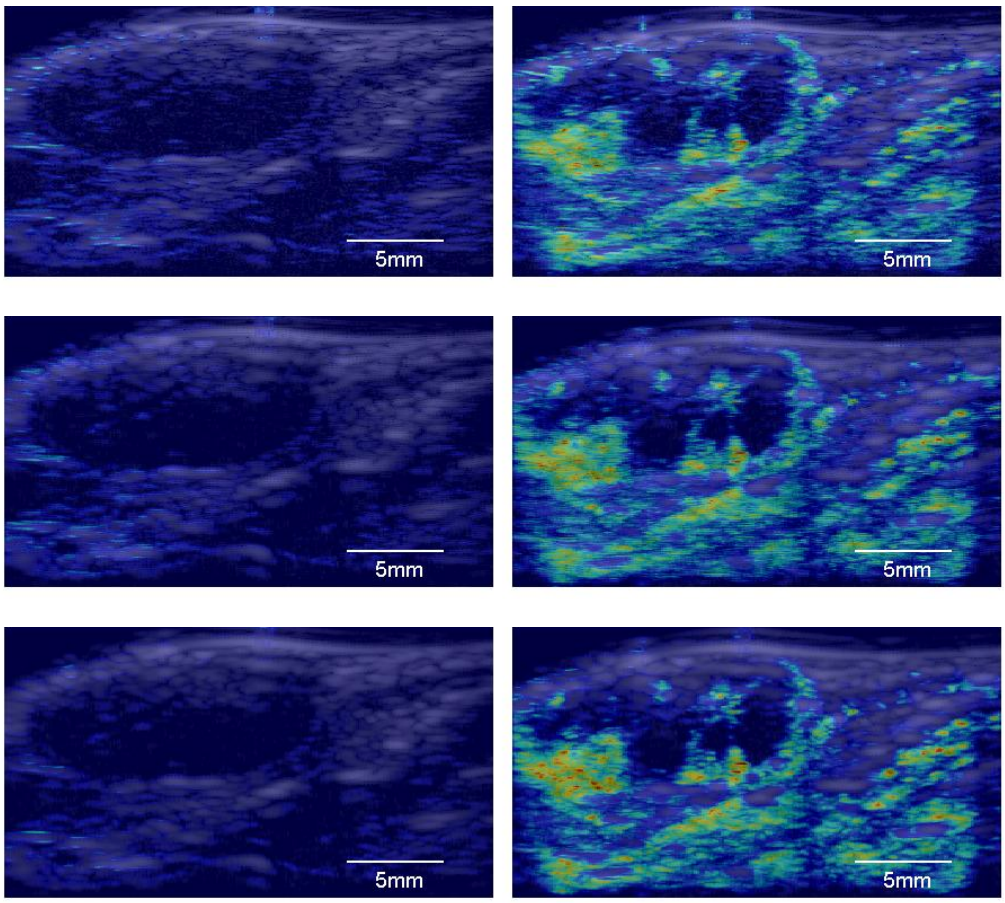

Figure 5.7: Linear (top), quadratic (center), and cubic (bottom) maximum TPI projections overlaid on B-mode images, without (left) and with (right) UCA. The dynamic ranges for TPI computation were 45, 105, and 165dB, respectively. The value of γ was 0.5.

To further illustrate the transient nature of the TPI values in the absence and presence of the UCA, the temporal profiles of normalized TPI values at R5 are shown in Figure 5.9. The R5, with a window size of $N' \times M' = 13 \times 7$, is defined in Figure 5.8 and was chosen because it exhibited a relatively large TPI value before the UCA injection which was related to the animal's breathing motion. The results from linear, quadratic, and cubic components are shown from left to right in the Figure 5.9. In this case, before the contrast injection, the pattern followed the breathing rhythm of the

animal under anesthesia (gasps approximately every 1.5 seconds). On the other hand, TPI values from the same location after the UCA injection were more sporadic with significantly higher values. This clearly shows that R5 represents a region in the image with relatively high perfusion. In addition, the TPI results using linear components were more sensitive to the animal's breathing motion, while quadratic and cubic results showed better separation between the data sets acquired without and with UCA for this region.

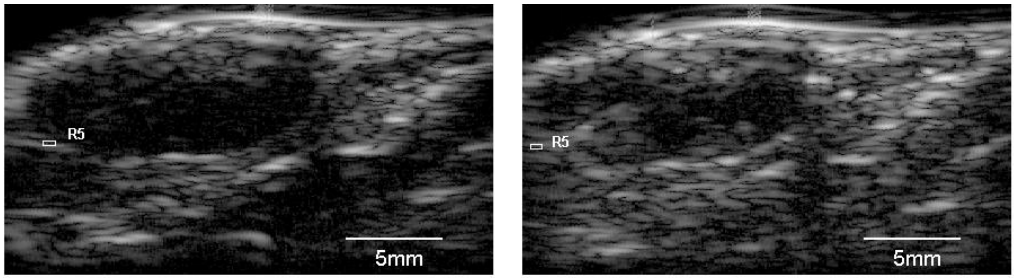

Figure 5.8: Define the location of R5 on one frame RF B-mode image (55dB) without (left) and with (right) UCA present.

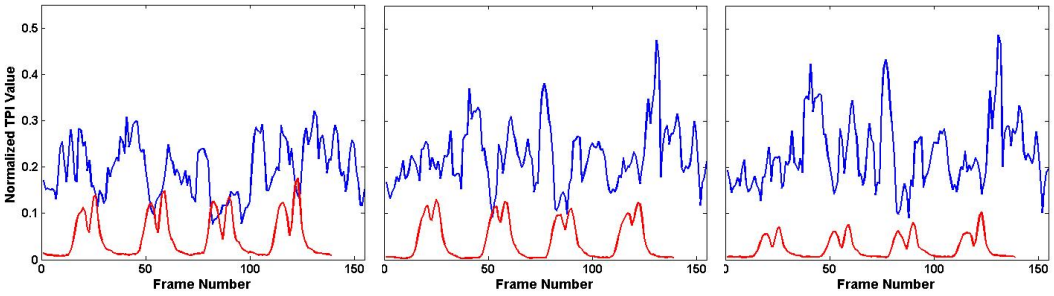

(a) Linear Component (b) Quadratic Component (c) Cubic Component

Figure 5.9: The trace of TPI values over frames, computed using linear, quadratic and cubic components at R5 without (red) and with (blue) UCA.

Dynamic Range Evaluation: To evaluate the TPI performance using the derived optimal dynamic range, the normalized TPI values with different dynamic ranges from $40dB$ to $210dB$ were computed using the four regions located in Figure 5.1. The four regions were chosen as a high perfused tumor region (R1), a low perfused tumor region

(R2), a low perfused tissue region (R3), and a tumor segment of no observed perfusion (R4). $TPI[t]$ was computed according to Equation 4.4 with $N' \times M' = 13 \times 7$ for all frames. The mean and standard deviation of $TPI[t]$ were computed for the time series, and the results are shown in Figure 5.10.

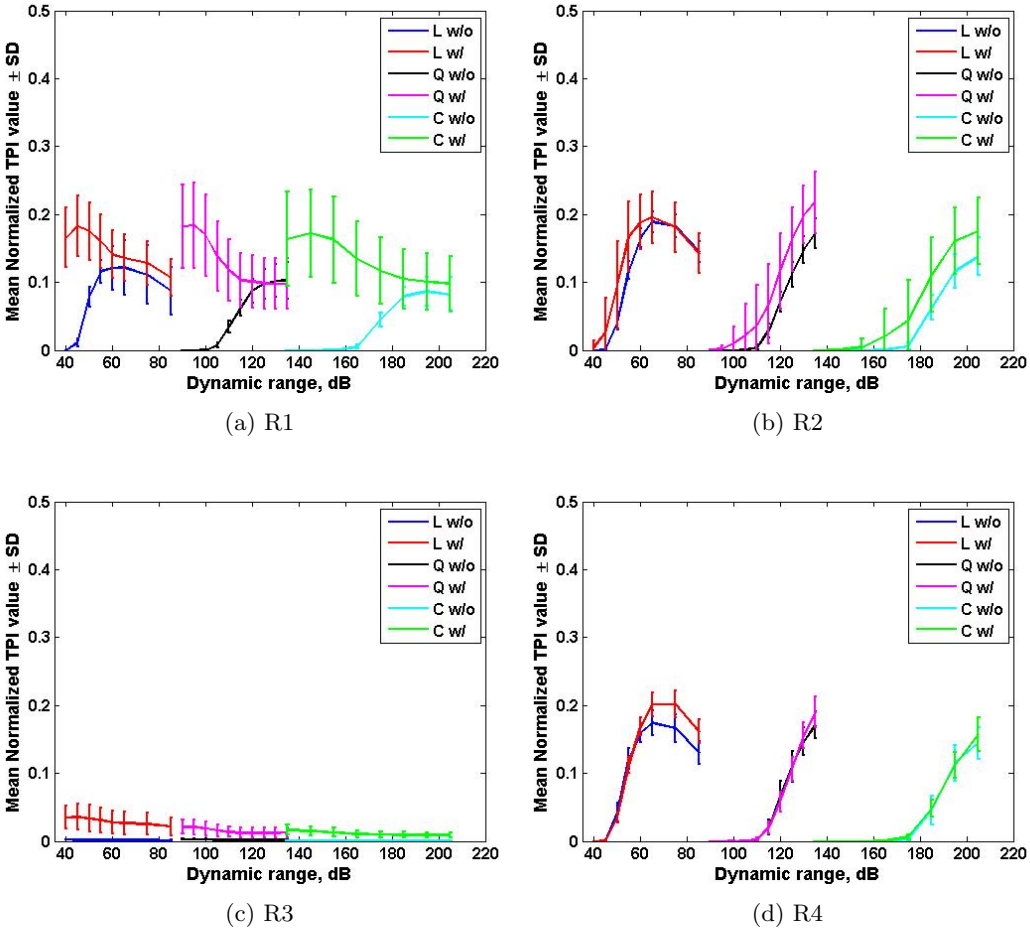

(a) R1 (b) R2

(c) R3 (d) R4

Figure 5.10: The mean and standard derivation of normalized TPI value with different dynamic ranges computed in four regions (R1 - R4) located in Figure 5.1. The value of γ was 0.5.

In the high perfused tumor region R1, small dynamic range, such as linear 40dB, quadratic 90dB, or cubic 140dB, was able to capture the UCA activity. However, with the growth of dynamic range, the TPI value computed using the data with UCA

decreased while the TPI value without UCA started to increase. For linear 60dB, quadratic 130dB, and cubic 180dB, the TPI value without and with UCA were relatively the same. TPI performance in region R3 exhibited similar behavior except for much smaller TPI values.

In the low perfused tumor region R2, the TPI values, computed using small dynamic range such as quadratic 90dB and cubic 140dB, were 0. This indicates that low dynamic range was not able to pick up the UCA activity and preserve UCA signals. On the other hand, the TPI value computed using linear components without and with UCA were relatively the same when the dynamic range was 60dB. The large TPI value without UCA was actually artifacts. This indicates that large dynamic range may result in artifacts which compromised TPI performance.

In R4 (no perfusion tumor region), high dynamic range, such as linear 45dB, quadratic 105dB, and cubic 165dB, introduced large TPI artifacts. Artifacts increased rapidly with the growth of the dynamic range.

Therefore, the choice of the dynamic range for TPI computation needs to account for different regions within the whole image. High, low and no perfused regions selected for their own dynamic range. The global dynamic range was determined by seeking a balance. The optimal dynamic range should be large enough to preserve the low perfusion activity while small enough to eliminate the noise and tissue motion to the largest extent. Overall, the derived dynamic ranges 45, 105, and 165dB were the simplistic tradeoff choice for the three components, respectively. The optimal choice may be achieved by seeking for localized dynamic range.

Intensity Ratio γ: Besides dynamic range, another important parameter which affects TPI performance is the intensity ratio γ. As stated in Equation 3.2, γ is designed to raise the low-echogenicity (UCA) average intensity above the noise floor. To explore the relationship between the value of γ and TPI performance, the mean and standard deviation of normalized TPI for the time series were computed using different values of γ. The results are shown in Figure 5.11.

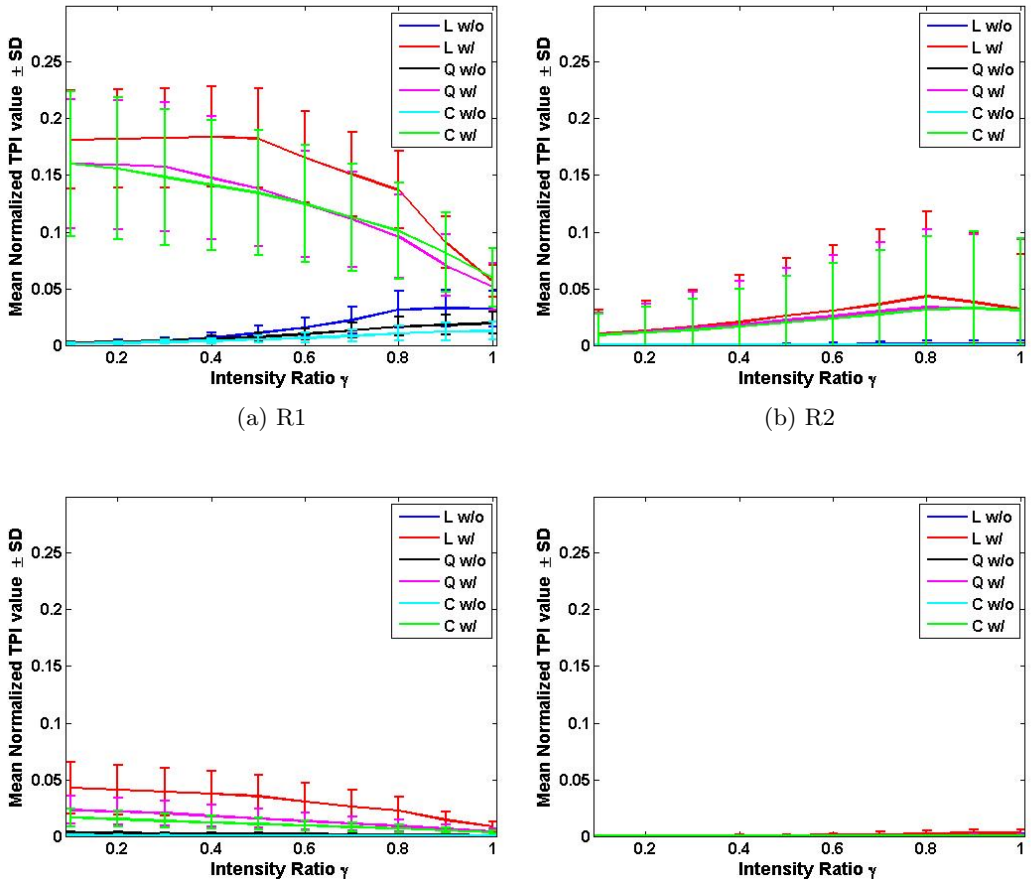

(a) R1 (b) R2

(c) R3 (d) R4

Figure 5.11: The mean and standard derivation of normalized TPI value with γ in four regions (R1 - R4) located in Figure 5.1. The dynamic ranges were 45, 105 and 165dB for three components respectively.

The TPI values decreased with the increase of the value of γ in perfused regions R1 and R3. TPI value in R1 decreased faster than that of R3. Similar behavior was observed in R2 as was observed in R1 when $\gamma \geq 0.8$. The normalized TPI values in R1 and R2 were relatively the same and larger than the TPI value in R3, when γ increased to approximately 1. This indicates that the high perfused tumor region was more sensitive to the change of γ; and a large value of γ rewarded TPI performance in the low perfused regions.

On the other hand, TPI artifacts resulting from noise increased with the increase of the value of γ in R4. This indicates that a large value of γ produced large artifacts. TPI artifacts may become dominant if γ keeps increasing.

Overall, a small value of γ achieves a better TPI separation between the data sets acquired without and with UCA. However, a large value of γ benefits low perfused regions. On the other hand, a large value of γ introduces large artifacts due to noise. The choice of γ should be determined by balancing this tradeoff.

5.1.5 Summary of *In Vivo* Tumor Results

The LNCaP tumor model provided an excellent example of a region with heterogeneous perfusion and echogenicity levels before and after the UCA injection. Regions within the tumor that can be easily characterized were identified as high and low perfused regions. The performance of the TVF components in terms of improving the sensitivity and specificity to UCA activity was supported by observing the dynamics of the echoes in Cine loop and on M-mode.

The TPI can be used to track perfusion while minimizing the sensitivity to breathing motion and high-intensity reflections from tissue and components other than blood vessels. The PDF-guided TPI images clearly discriminate between the echoes due to the UCA activity and the changes due to the tissue motion/breathing. The TPI value can provide qualitative indications of perfusion density in both heterogeneous tumor region and homogeneous tissue region.

To sum up, the results show large resolution imaging of heterogeneous tumor perfusion over a high dynamic range using standard diagnostic probes and clinically-relevant concentrations of UCA.

Chapter 6

Transcranial Imaging Guidance for Noninvasive Brain Disease Treatment

6.0 Introduction: Transcranial Brain Perfusion Imaging

Transcranial focused ultrasound (tFUS) is an emerging noninvasive neuromodulation approach [57, 58]. Most currently employed methods, such as vagus nerve stimulation (VNS) [59], require invasive procedures. Invasive treatments require operation on patients' skull, which increases the chances of infection and other serious complications. Therefore, noninvasive brain disease treatment using focused ultrasound is gathering more and more attentions.

Applications of tFUS include blood brain barrier (BBB) opening, tumor ablation, etc. A major challenge to the reliability of tFUS application are the combined effects of reflection, absorption, and aberration through the skull [59]. These have a detrimental effect on the quality of the focus, both in terms of focal gain and location. The use of microbubble ultrasound contrast agents has allowed for the use of tFUS to produce bioeffects at lower intensities and provided a partial answer to the reduction in focal gain. However, the distribution of UCA throughout the brain can result in unintended bioeffects at locations other than the intended target.

A high resolution imaging method for monitoring microbubble perfusion density in the small vessels (μm size) would provide a beneficial form of feedback for guiding the tFUS application. In addition, transcranial perfusion imaging would be extremely useful in the characterization of ischemia, such as in the context of characterization of stroke. Transcranial perfusion imaging is a critical tool for providing diagnosis and treatment of brain disease.

Modalities used for brain perfusion imaging include computerized tomography [60, 61], positron emission tomography [62], and single-photon emission computed tomography [63]. As mentioned in Chapter 1, these methods produce radiation and/or require radioactive material injection. The idea of optical brain imaging was proposed in [64]. In spite of its safety, optical brain imaging faces the challenge of overcoming the limitation of penetration depth and imaging resolution because of light scattering [65]. Functional magnetic resonance (MR) can also be used to image brain perfusion. However, MR is expensive and its data acquisition is typically a time-consuming task.

Ultrasound is a diagnostic medical imaging modality with a proven safety record [59]. Recently, ultrasound transcranial imaging has been widely studied [66, 67, 68, 69]. In this chapter, both *in vitro* and *in vivo* ultrasound transcranial perfusion imaging using our methods are presented and discussed.

6.1 Transcranial *In Vitro* Experiments

6.1.1 Experiment Setup

The experimental setup is illustrated in Figure 6.1. The top left image is of a rat's skull which was embedded in a tissue-mimicking phantom approximately 1-2mm below the surface. Two 200μm cellulose tubes were embedded approximately 8mm below the skull. The two channels were placed in parallel with the sagittal suture of the skull and approximately 4mm apart from each other.

The top right image is a one frame B-mode (35dB) image of the skull phantom acquired using the LA14-5/38 transducer. The image was collected from the phantom surface closer to the cellulose channels in order to avoid the interference from the skull. The two channels are indicated by the arrows in the image. The image provides the spatial relationship between the two channels and the skull.

The bottom image is the setup of the skull phantom experiment using the DMUA. The DMUA was fixed at one side of the tank, submerged in the degassed and deionized water. The phantom was placed within the focal zone of the DMUA. The imaging system was described in Section 1.3.2. The data were acquired with the GPU-based platform at a frame rate of approximately 23 fps from the phantom surface closer to the skull. The MI was lower than 0.09. During the data acquisition, the right side channel had saline pumped through, while the left channel had UCA solution with a concentration of approximately 2.4×10^8 microbubbles per mL ($1 : 10$ UCA to saline) pumped through. The flow rate was approximately 6mL/hour.

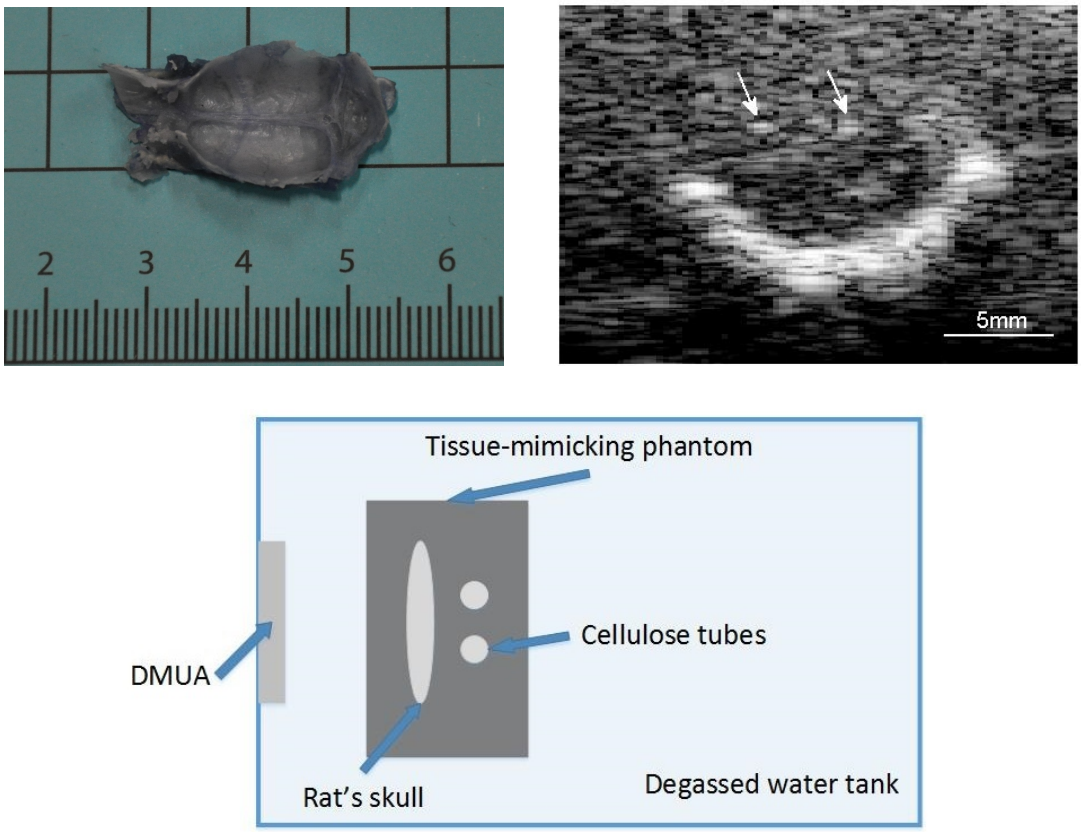

Figure 6.1: An illustration of the experimental setup. Top left: A picture of the rat's skull. Top right: One frame B-mode (35dB) image of the skull phantom. The data were acquired using the linear array LA14-5/38. Bottom: A schematic of the experimental setup with DMUA.

The purpose of this experiment was to test the feasibility of trans-skull imaging of UCA microbubbles activity in the cellulose microchannels. The use of the DMUA prototypes in image-guided tFUS application in small animal models has been presented in [70]. The focus of this section is on DMUA transcranial perfusion imaging performance.

6.1.2 DMUA SA B-mode Imaging

The data acquisition using the DMUA started with locating the two channels. The data set was first acquired at the location without the presence of the skull. One frame SA B-mode (65dB) image is shown in Figure 6.2a. Both cellulose tubes with saline pumped through were clearly detected at 42mm axially. The DMUA SA B-mode image exhibited better imaging quality and higher SNR than the B-mode image collected using the LA14-5/38 (Figure 6.1). The left channel was slightly brighter than the right channel because the left one was closer to the geometric center of the transducer, which was (40mm, 0mm) in the axial and lateral dimensions. The DMUA's concave structure and SA beamforming reward targets near the geometric center.

After locating the two channels, the phantom was moved 20mm along the channels' axes to a new position where the skull existed. The UCA solution was pumped though the left channel while the saline was kept for the right one. 251 SA beamformed frames were collected at a frame rate of approximately 23 fps. This data set is referred to as "skull with UCA". The B-mode image is shown in Figure 6.2b. In the presence of the skull, the signals reflected from the distal tissue was much weaker.

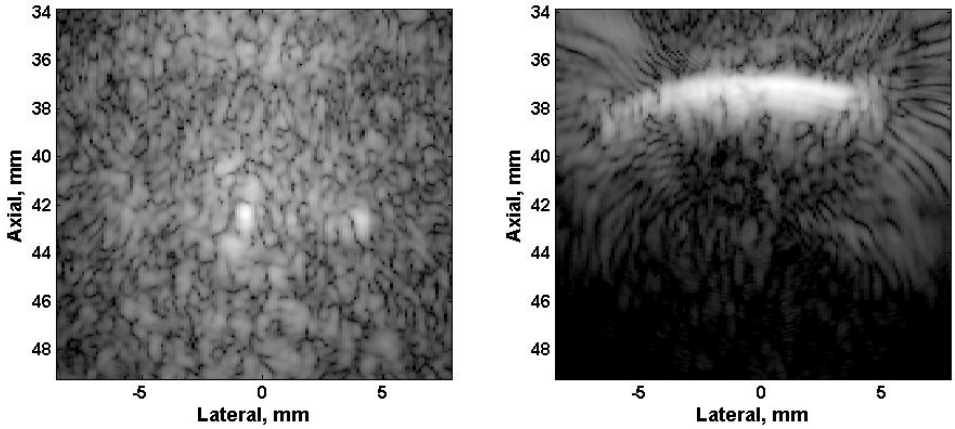

(a) SA Image without Skull Present, Saline (b) SA Image with Skull Present, UCA (left)

Figure 6.2: The SA B-mode (65dB) images without and with the presence of the skull.

6.1.3 Third-order Volterra Filter and Temporal Perfusion Index

A TVF with system order of 15 was derived from the one A-line with UCA present using the data set "skull with UCA". The forgetting factor $\lambda = 0.999$ and regularization parameter $\alpha = -0.4$. It took 680 samples before the filter converged. The filter was applied to the whole data sets. After that, the TPI was applied to the outputs of the filter. To save space, only linear and cubic TPI maximum projections computed using the data set "skull with UCA" are presented in Figure 6.3. The dynamic ranges for TPI computation using linear and cubic components were determined as 50dB and 160dB, respectively. The quadratic component exhibited similar behavior to the cubic component. Each TPI frame was computed using 13 frames with the parameter $\gamma = 0.25$.

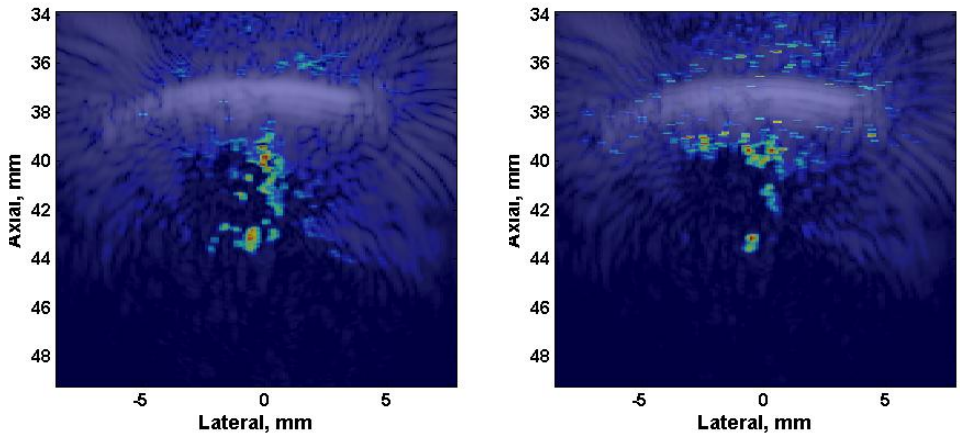

(a) Linear TPI Maximum Projection (b) Cubic TPI Maximum Projection

Figure 6.3: The linear and cubic TPI maximum projections map overlaid LB-mode and CB-mode images. The dynamic ranges for TPI computation using linear and cubic components were 50dB and 150dB, respectively.

The observations from Figure 6.3 can be summarized as follows:

1. The TPI can successfully detect the UCA activity, using either linear or nonlinear components. The channel location captured by linear and nonlinear TPI were consistent with each other. They were also consistent with the information shown in Figure 6.2.

2. Nonlinear TPI exhibited much more confined spatial extent, in both axial and lateral directions.

3. Linear TPI suffered more artifacts near the skull and close to the geometric center (40mm 0mm), due to the noise.

6.1.4 New Imaging Plane with Chirp Excitation

In the image plane shown before, the channel with UCA was closer to the transducer's geometric center (40mm, 0mm) than the other channel with saline. To eliminate the interference due to the difference of the channels' spatial positions, the phantom was moved to a new position (referred to as L2 in this section). One frame B-mode image of L2 is shown as the left image in Figure 6.4. Two channels were placed nearly symmetrically with respect to the geometric center. The UCA solution was switched to the right channel and saline was switched to the left one. 241 SA beamformed frames were collected at a frame rate of 23 fps. The two channels were clearly observed under the SA B-mode image. However, no visible difference between the two can be found. Moreover, more tissue components were observed at L2 as compared to the previous location, due to the smaller skull at L2.

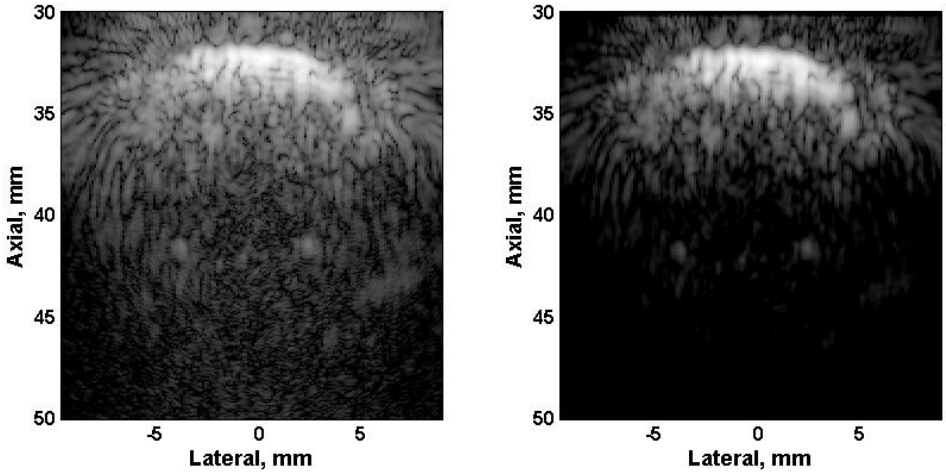

(a) Raw SA B-mode Image (b) Cubic SA B-mode Image

Figure 6.4: One frame SA B-mode (65dB) and CB-mode (180dB) images of the skull phantom at a new imaging plane L2. Two cellulose channels were symmetric to the geometric center of DMUA.

A TVF with the system order of 13 was derived using one A-line with UCA present. The forgetting factor $\lambda = 0.999$ and the regularization parameter $\alpha = 0.2$. It took 356 samples before the filter converged, and then the filter was applied to the whole data set. The CB-mode (180dB) shown in Figure 6.4(b) exhibited much higher SNR, though, there was still no visible difference between the two channels. The quadratic component exhibited similar performance to the cubic component.

The TPI was applied to all three components. The dynamic ranges to compute TPI using linear and cubic components were determined as 37dB and 135dB, respectively. The quadratic component was not shown since it exhibited similar behavior to the cubic component. Each TPI frame was computed using 13 frames with the parameter γ =0.25. The TPI maximum projections at L2 are shown in Figure 6.5.

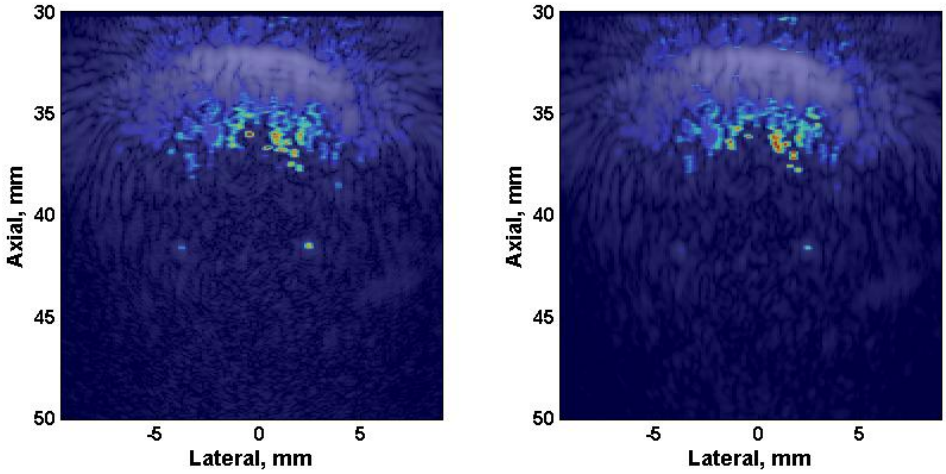

(a) Linear TPI Maximum Projection (b) Cubic TPI Maximum Projection

Figure 6.5: The TPI maximum projection maps overlaid on LB-mode and CB-mode images. The dynamic ranges to compute TPI using linear and cubic components were 37dB and 135dB, respectively.

The observations from Figure 6.5 can be summarized as follows:

1. The TPI can detect UCA activity and distinguish the difference between two channels. Two channels at L2 were distributed symmetrically with respect to the transducer's geometrical focus. The comparison between the two channels was free of interference resulting from different DMUA focal gain at different spatial position.

2. Both linear and nonlinear TPI images were able to location the channel with UCA. Nonlinear TPI showed better separation between the two channels than linear TPI.

3. Artifacts were mainly distributed near the skull and observed in both linear and nonlinear TPI images. Nonlinear TPI exhibited less artifacts than linear TPI.

The TPI artifacts may come from two sources. First, the bubbles were trapped by the rat skull, due to the surface of the rat skull being irregular and coarse. Some bubbles may be trapped near the skull when making the phantom and resulted in artifacts.

Second, the noise resulting from the electronic device and is mainly distributed in the focal zone of the transducer. This type of noise and denoising method will be introduced in Section 8.2.1.

Chirp Excitation and Compression: In [71], chirp compression was proposed to improve the signal-to-noise ratio and image quality. The chirp signal was designed to cover the main bandwidth of the transducer transmitting signals. Its time and frequency responses are shown in Figure 6.6. The chirp compression used a matched-filter approach to recover the axial resolution. Approximately 220 frames were acquired at L2 with chirp excitation at a frame rate of approximately 23 fps.

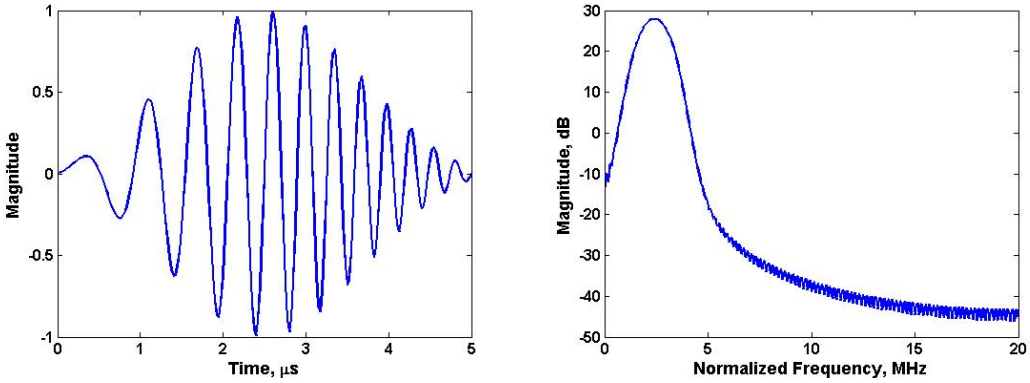

(a) Time Response (b) Frequency Response

Figure 6.6: The time and frequency responses of the chirp signal.

The left image in Figure 6.7 is one frame B-mode (65dB) image at L2 with chirp excitation and a matched filter compression. One can tell that the axial resolution was compromised after the chirp compression, though the SNR of the image was improved. The same TVF derived from the last section was applied to the data set after the chirp compression. The CB-mode (180dB) image is shown in Figure 6.7(b). The two channels were visible in the image, but no difference between the two channels was observed.

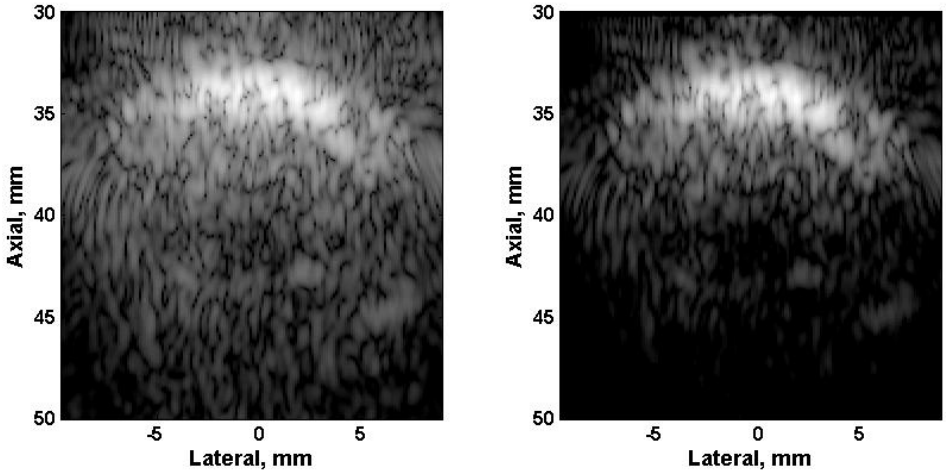

(a) Raw B-mode Image (b) Cubic B-mode Image

Figure 6.7: The SA B-mode (65dB) and CB-mode (180dB) images with chirp excitation and a matched filter compression.

The TPI was applied to the outputs of the TVF. The TPI maximum projections overlaid on B-mode images are shown in Figure 6.8. The quadratic component was not shown since it exhibited similar behavior to the cubic component. The dynamic ranges for TPI computation using linear and cubic components were 38dB and 140dB, respectively. Each TPI frame was computed using 13 frames, with a parameter $\gamma = 0.5$.

The UCA activity was successfully detected when applying TPI method. Moreover, TPI artifacts near the skull region were largely suppressed. However, artifacts were still observed close to the geometric center of the transducer, due to the noise.

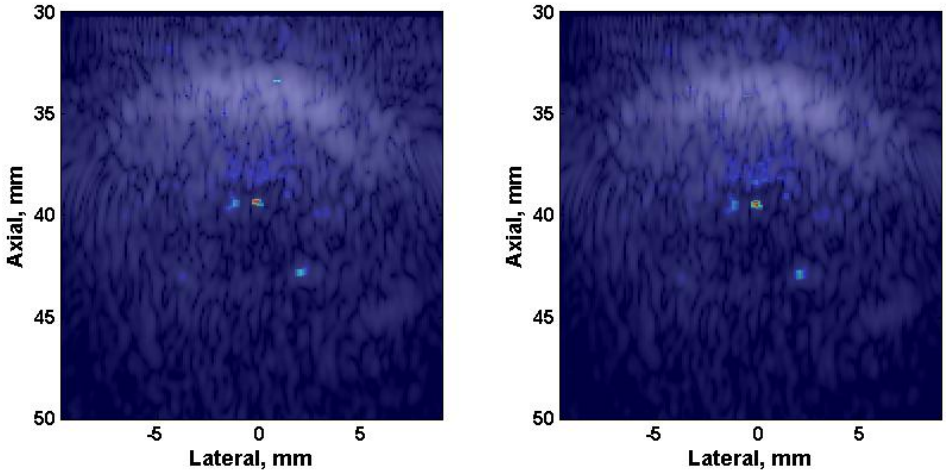

(a) Linear TPI Maximum Projection (b) Cubic TPI Maximum Projection

Figure 6.8: The TPI maximum projection maps overlaid LB-mode and CB-mode images. The results were acquired with the chirp excitation and compression. The dynamic ranges for TPI computation using linear and cubic components were 38dB and 140dB, respectively.

Overall, chirp excitation followed by a matched-filter compression can improve the imaging quality, at the cost of compromising the axial resolution. However, the TPI artifacts were much reduced without sacrificing the image resolution.

6.2 Transcranial *In Vivo* Experiment

6.2.1 Experiment Setup

The experimental setup shown in Figure 6.9 was under approved IACUC protocol. A healthy rat (250 - 300 grams) was anesthetized with Ketamine and Xylazine and placed in a prone position. The animal's head was secured with ear bars to reduce the breathing motion effect. The DMUA was used for transcranial imaging of the animal's brain without and with UCA. The imaging system was described in Section 1.3.2. Real-time SA beamforming was performed on a GPU at a frame rate of approximately 23 fps with a low MI setting below 0.09.

Images were obtained before and after an injection of 100 μL of SIMB4-5 UCA

(Advanced Microbubbles Laboratories, Boulder, CO) diluted with 200 μL sterile saline (5.3×10^8 microbubbles per mL). SIMB4-5 contains size-isolated lipid-coated gas-filled microbubbles with a mean diameter of 4.2 $\pm$ 1.0 μm. It is designed for ultrasound imaging and targeted delivery applications. An MP36R data acquisition and analysis system (BIOPAC Systems, Inc., Goleta, CA) was used to monitor the animal's ECG signals and temperature while performing the experiment. No dominant breathing motion was observed.

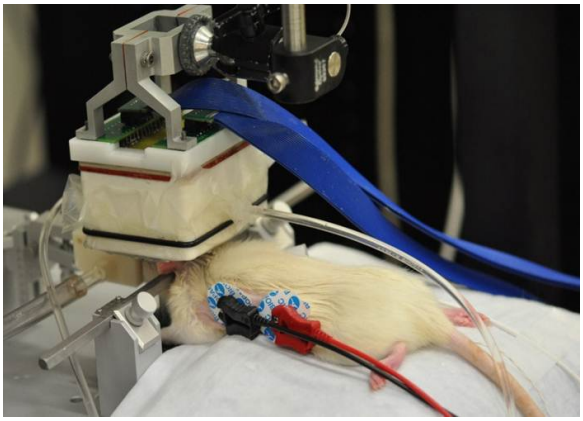

Figure 6.9: An *in vivo* experimental setup. The animal was placed in a prone position. The head was secured with ear bars. The data were collected with DMUA transducer under SA mode. Electrode sensors were place in both sides of the animal's chest for monitoring its ECG signals.

6.2.2 SA B-mode Imaging

Figure 6.10 shows transcranial SA B-mode (55dB) images without and with UCA present. The animal's position was slightly changed after the injection but the change was limited. No discernible echogenicity improvement was observed after the injection. A large vessel was detected at (42mm, 0mm) in the axial and lateral directions near the base of the skull. It could be observed even before the UCA injection.

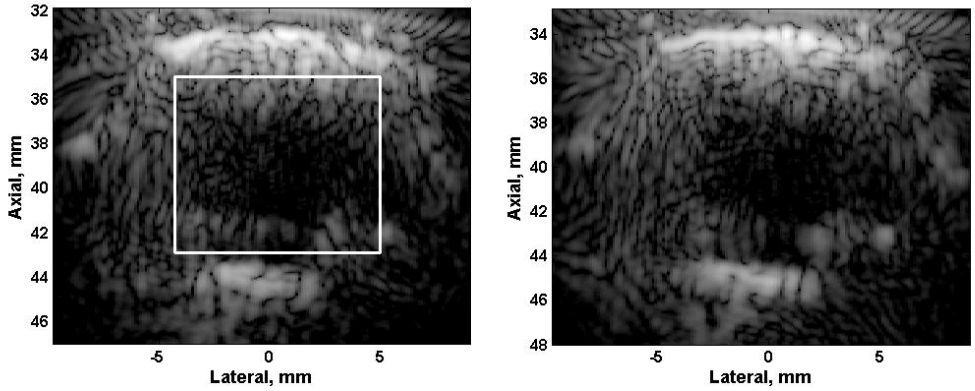

(a) SA Image w/o UCA (b) SA Image w/ UCA

Figure 6.10: Transcranial B-mode (55dB) images without (left) and with UCA present.

6.2.3 Third-order Volterra Filter

A TVF with a system order of 13 was derived from one A-line with UCA present. The forgetting factor $\lambda = 0.999$ and the regularization parameter $\alpha = 0.12$. The filter converged after 122 samples and then was applied to the whole data sets, without and with UCA.

6.2.4 Temporal Perfusion Index

The data used to derive the dynamic range for TPI computation was located in the center of the brain, which was highlighted using the white rectangular window shown in Figure 6.10a. The dynamic ranges for TPI computation using linear, quadratic and cubic components were determined as 50dB, 130dB and 190dB, respectively. Each TPI frame was computed using 5 frames with a parameter γ =0.75.

Figure 6.11 shows the TPI maximum projections overlaid on B-mode images. The results were computed using all three components. The large vessel near the base of the skull observed before UCA injection was also observed in the TPI images. Moreover, the TPI was able to detect the vessels at the left side of the brain with UCA present. The TPI results computed using the three components were consistent with each other.

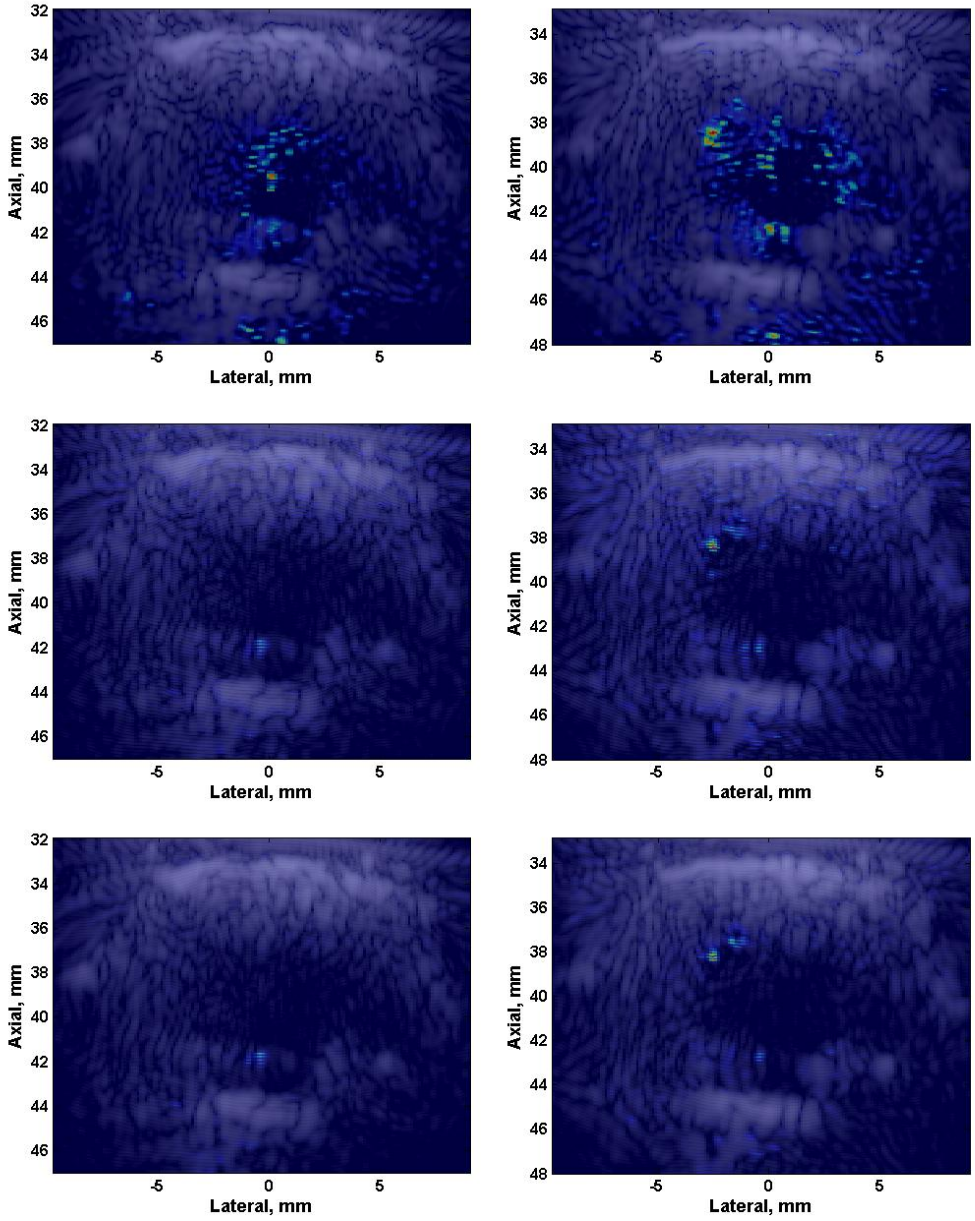

Figure 6.11: The TPI maximum projection overlaid on B-mode images generated using linear (top), quadratic (center), and cubic (bottom) components, before (left) and after (right) the UCA injection. The dynamic ranges for TPI computation using each component were 50, 130, and 190dB, respectively.

The observations from Figure 6.11 can be summarized as follows:

1. Linear components were more vulnerable to the noise at the DMUA focal zone. The TPI results computed using linear components without and with UCA showed large TPI artifacts in the DMUA focal zone, while these artifacts were not observed in the TPI images computed using nonlinear components.

2. The vascular locations identified by nonlinear components were more confined and localized. On the other hand, the spatial extents of the vessels computed using the linear component appeared much larger.

One point of consideration is that linear TPI plots showed multiple locations with large TPI values on the right side of the brain. We strongly believe that some of these contained UCA signals. Even though the histology is needed to determine whether these were true vascular structures or artifacts, this result indicates that a localized TPI method is needed to identify vessels with different sizes at multiple locations. The idea will be discussed in Section 8.2.3.

To further demonstrate the transient behavior of the TPI, the temporal profiles for each component in a representative region (approximately 38mm axially and -2.5mm laterally) with a window size of $N' \times M' = 21 \times 3$ (0.4×0.35 mm^2 in axial and lateral directions) are shown in Figure 6.12. A distinct separation of TPI values can be observed with all three components. Moreover, the transient behavior computed using three components were consistent with each other. In the transient profiles without UCA present, one can see the periodic signal due to the animal's breathing motion, but the motion was limited and did not interfere with the TPI performance.

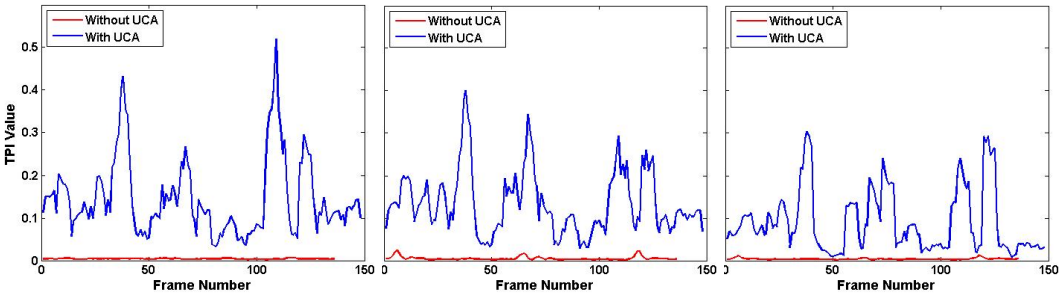

(a) Linear Components (b) Quadratic Components (c) Cubic Components

Figure 6.12: Normalized TPI trace over frames using linear, quadratic, and cubic components, before (red) and after (blue) UCA injection.

6.3 Transcranial *In Vivo* Experiment with Pronounced Breathing Motion Present

6.3.1 Experiment Setup

The experimental setup was similar to the previous transcranial *in vivo* experiment. But there were two differences. First, the injection for this experiment used 60 μL of Targestar-P UCA with 140 μL sterile saline (approximately 8.7×10^8 microbubbles per mL). Second, the animal's breathing motion was much more pronounced, gasping visible approximately once every 68 frames.

6.3.2 SA B-mode Imaging

Figure 6.13 shows transcranial SA B-mode (50dB) images without and with UCA present. As one can observe, after UCA injection, the echogenicities in the center of the brain were enhanced, modestly.

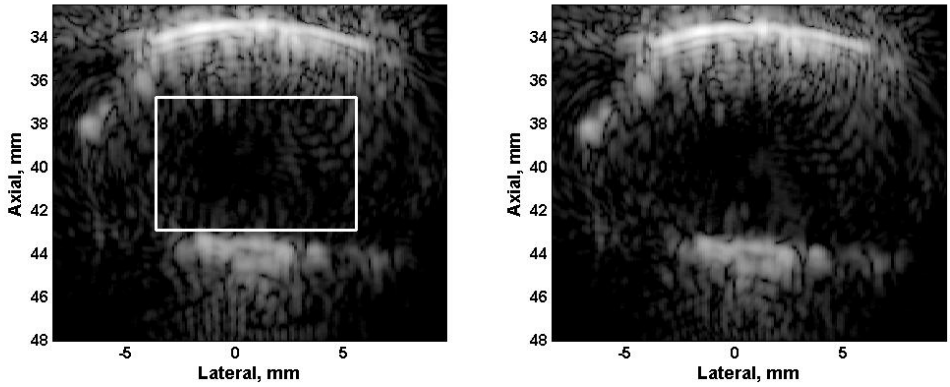

(a) SA Image w/o UCA (b) SA Image w/ UCA

Figure 6.13: Transcranial B-mode (50dB) images without (left) and with UCA present.

6.3.3 Third-order Volterra Filter

A TVF with a system order of 15 was derived from one A-line with the presence of UCA. The forgetting factor $\lambda = 0.999$ and the regularization parameter $\alpha = -0.367$. The filter converged after 304 samples. The filter was implemented to separate linear, quadratic, and cubic components from the beamformed echo data.

6.3.4 Dynamic Range Selection for Motion-triggered TPI

The animal's breathing motion was pronounced when acquiring data. Therefore, motion-triggered TPI was adopted to further suppress this motion. As illustrated in Section 3.3.1, the dynamic range for motion-triggered TPI is determined by accounting for the variation of $\Delta f(\nu, t)$ (instead of $f(\nu, t)$) over frames. The procedure is detailed as follows.

First, region of interest was determined. The imaging target in this experiment was the center of the brain, which was highlighted using the rectangular window shown in Figure 6.13a. Then, the variance of the $\Delta f(\nu, t)$ was computed for each data set and the result is shown in Figure 6.14 (only cubic result shown here).

Figure 6.14 provides guidance to determine the dynamic range. A proper dynamic range is able to preserve the changes from the contrast agent activity while suppressing

the variation due to noise and motion. To achieve this, the dynamic range was determined as 170 dB because for the log-compressed value of $V_C(\nu)$ larger than -170 dB, the variance of data with UCA was larger, and the for the value less than -170 dB, the variance without contrast was larger.

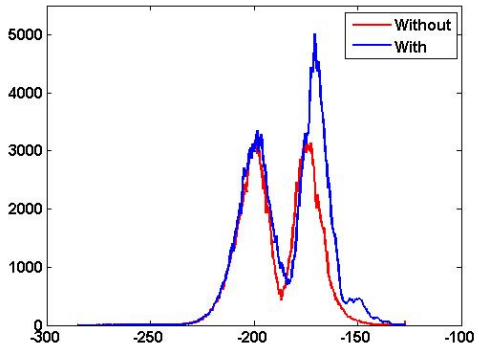

Figure 6.14: The variance distribution of the $\Delta f(\nu, t)$ (cubic component).

6.3.5 Motion-Triggered TPI

The motion-triggered TPI was applied to three components after deriving the dynamic range. Since the animal's breathing cycle was 68 frames (3 sec), the parameter N_t in Equation 3.5 was determined as 68. The dynamic ranges for the TPI computation using linear, quadratic, and cubic components were determined as 50, 120 and 170dB, respectively. Each TPI frame was computed using 4 frames, with a parameter $\gamma = 0.75$. The TPI maximum projections overlaid on B-mode images are shown in Figure 6.15.

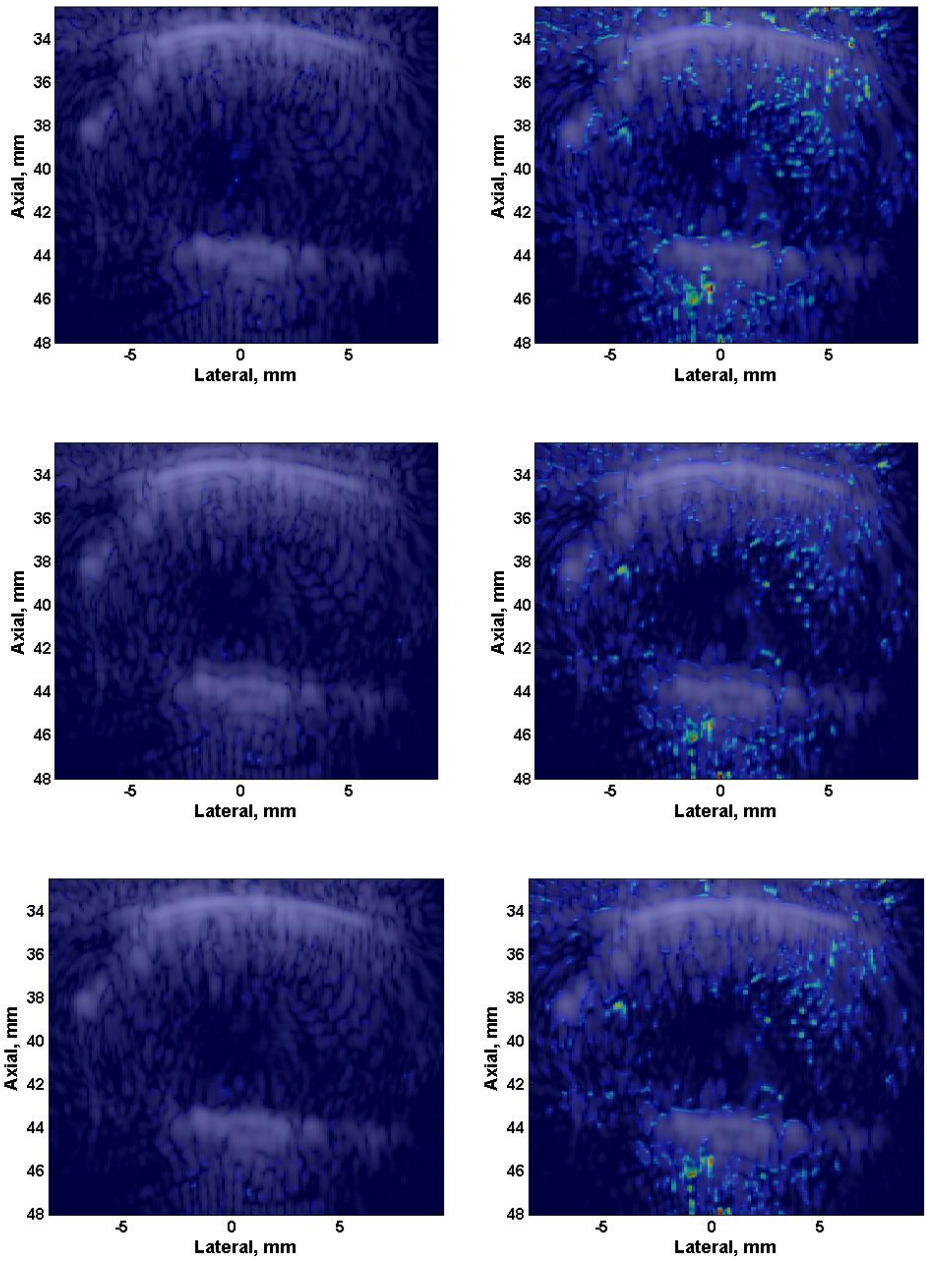

Figure 6.15: The TPI maximum projection over B-mode images using linear (top), quadratic (center), and cubic (bottom) components, before (left) and after (right) UCA injection. The dynamic ranges for TPI computation using linear, quadratic, and cubic components were 50, 120, and 170dB, respectively.

The observations from Figure 6.15 can be summarized as follows:

1. The method showed sensitivity to UCA oscillation using both linear and nonlinear components, even with the interference from the animal's breathing motion. The TPI maximum projections successfully detected numerous localized perfusion regions which contained in-plane and out-of-plane UCA motions and could be discerned on movies of QB-mode and CB-mode images.

2. While all three components exhibited TPI profiles consistent with the UCA activity, the nonlinear components exhibited better separations of the data sets acquired before and after UCA injection and improved SNR.

To test whether the derived dynamic range was the optimal choice, the TPI vales with different dynamic ranges with a step size of 10dB were computed, and the mean and standard derivation of normalized TPI results over frames are shown in Figure 6.16. The results were plotted using a representative vessel region (approximately 39mm axially and 2mm laterally) with a window size of $N' \times M' = 31 \times 3$ (0.4×0.35 mm^2 in axial and lateral directions). The information drawn from Figure 6.16 can be summarized as follows:

- Nonlinear components extended the dynamic range significantly.

- The choice of dynamic range to compute TPI was not too critical. Clear separation before and after UCA injection can be observed in the ranges linear 50 ± 10 dB, quadratic 125 ± 15 dB and cubic 180 ± 20 dB.

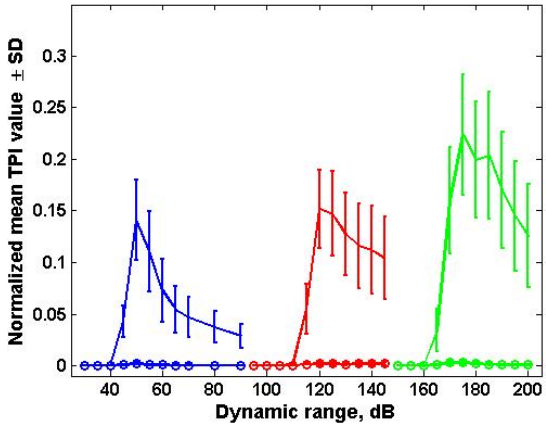

Figure 6.16: The mean and standard derivation normalized TPI value with different dynamic ranges from linear (blue), quadratic (red), and cubic (green) components, before (circle) and after (solid) UCA injection.

To further demonstrate the transient behavior of the TPI, Figure 6.17 shows the temporal profiles of the TPI at the same representative region as the one used to plot Figure 6.16. A clear separation of TPI values can be observed for all three components and nonlinear components showed relatively better separation than linear ones.

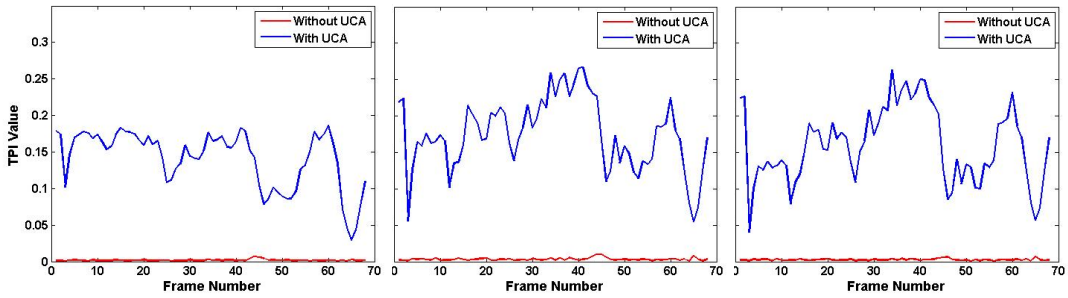

(a) Linear Components (b) Quadratic Components (c) Cubic Components

Figure 6.17: Normalized TPI trace over frames using linear, quadratic, and cubic components, before (red) and after (blue) UCA injection.

6.4 Conclusion and Discussion

The *in vivo* transcranial experiments were performed on multiple animals. The experimental results have proved that the TVF and TPI are able to enhance UCA activity with high spatial resolution and also provide qualifications at heterogeneous perfusion regions due to the pixel-wise nature of the processing and uniform excitation from the DMUA. Moreover, the motion-trigger TPI is capable of imaging brain perfusion with pronounced animal's breathing motion present, by determining the time interval of a breathing cycle, N_t frames, to cancel out the breathing motion's effect.

There some factors that may affect the imaging performance. The first factor is the DMUA focal zone noise. Transcranial perfusion imaging is more sensitive to DMUA focal zone noise, due to its low SNR resulting from the presence of skull. The discussion on reducing DMUA focal zone noise will be provided in Section 8.2.1. The second factor is the amount of UCA microbubbles which were actually injected into the animal's tail vein. In some experiments, it was difficult to tell whether UCA microbubbles were successfully injected. Catheter injection is proposed to improve the accuracy of the UCA injection. Meanwhile, it can limit animal's position change during the injection. This is highly recommended for future transcranial experiments.

Chapter 7

Preliminary Study on Perfusion Imaging for Sickle Cell Disease

7.0 Introduction: Sickle Cell Disease

Sickle cell disease (SCD) is a genetic disorder which affects more than 13 million people worldwide and is a life-threatening disease associated with many acute and chronic complications [72, 73]. SCD is caused by genetically abnormal β-globin which changes the way that hemoglobin works and extends gels upon deoxygenation [72]. Two recommended treatments include hydroxyurea and long-term blood transfusions [73], both of which are invasive and involve side effects.

Researches have shown that contrast-enhanced ultrasound can provide imaging guidance and potential treatment for SCD [74, 75, 76]. The key idea of the treatment is to achieve reoxygenation by carrying the deoxygenated sickle cells to where they can be more exposed to oxygen and therefore reverse the abnormality.

In this chapter, the preliminary feasibility study on perfusion imaging with DMUA is presented. The UCA perfusion imaging was performed on a $15\mu m$ channel embedded in a micro-fluidic device which was designed to mimic SCD environment. Discussions and suggestions for future work are also given.

7.1 Preliminary Feasibility Study on Sickle Cell Disease

7.1.1 Experiment Setup

A micro-fluidic device (in Figure 7.1) was designed to mimic the sickle cell environment and was used for the experiment. The device was made of the polydimethylsiloxane (the blue layer on the top) and bonded to the polystyrene (the grey layer at the bottom). Three 15μm micro-channels were embedded at the bottom of polydimethylsiloxane layer to mimic the microvessels. There was a gas layer approximately 150μm above the micro-channels with a size of 1.5mm $\times$ 150μm. Metal pores were embedded in each side of the channel and could connect the channels to syringes which pumped solution through during the experiment.

The experimental setup is shown in Figure 7.1. The device was submerged in the degassed water and placed in the DMUA imaging plane. Three channels in the device were connected to syringes through the metal pores. A micropump (NE-4000, New Era Pump Systems, Inc, Farmingdale, NY) was used to pump saline and contrast agents at a rate of 300μL/h. The imaging system was described in Section 1.3.2. Real-time synthetic aperture (SA) beamforming was performed on a GPU at a frame rate of approximately 23 fps.

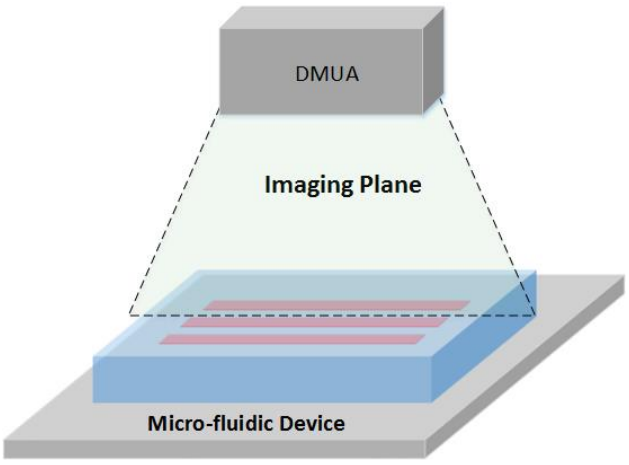

Figure 7.1: The sickle cell experimental setup. The device was submerged in the degassed water and placed in the DMUA imaging plane.

The experiment started with locating the three channels. The metal pores, which were easy to detect in ultrasound images, were used as markers to locate the channels. Longitudinal imaging data collection was carried out using the following procedures:

1. Adjust the position of the device so that the channels were in parallel with the imaging plane.

2. Move the device until one metal pore was placed in the center of the imaging slice. Because the channels were in parallel with the imaging plane, the channel connected to the metal pore was within the imaging plane and in the lateral direction. This position was recorded as the initial position. To double check if the channel was within the imaging plane, the device was moved longitudinally 20mm along the channel's axis to the other side. Another metal pore connected with the same channel appeared in the ultrasound B-mode image.

3. Move the device back to the initial position. SA beamformed frames were collected while water was being pumped through the channel at a rate of 300μL/h (the same speed for the following steps). This data set is referred to as "baseline".

4. The device was moved longitudinally 12mm along the channel's axis. At the new location, the center of the channel was within the DMUA focal zone. SA beamformed frames were collected while water was being pumped through. This data set is referred to as "target".

5. At the same location, UCA solution with a concentration of 8.2×10^8 microbubbles per mL (1 : 2.5 UCA to saline) replaced water. SA beamformed frames were collected while UCA solution was being pumped through. This data set is referred to as "target with UCA".

The B-mode (45dB) images of the device are shown in Figure 7.2. The device was moved approximately 2mm closer to the transducer when switching water to the UCA solution. The echogenicities in the channel slightly increased with UCA, but this may also be due to reverberation.

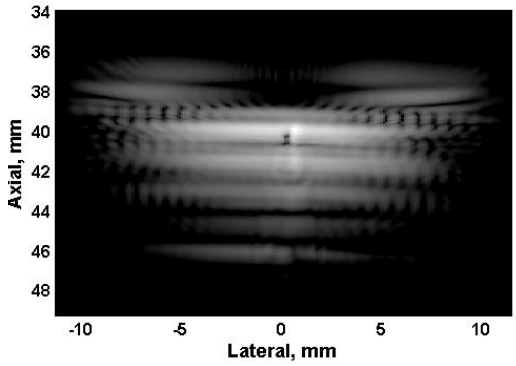

(a) Longitudinal Baseline Image

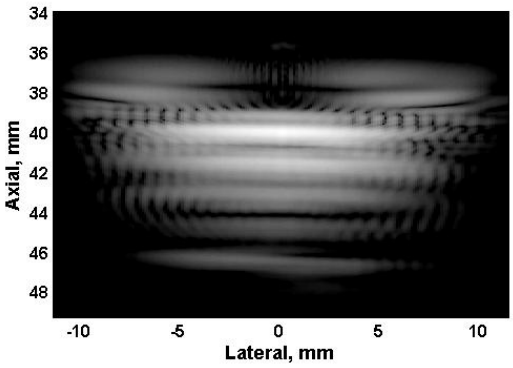

(b) Longitudinal Target Image

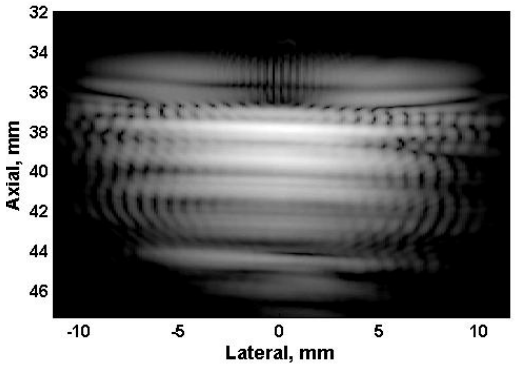

(c) Longitudinal Target Image with UCA

Figure 7.2: B-mode (45dB) images of a micro-fluidic device. One metal pore connected to the channel was clearly observed in the baseline B-mode image.

7.1.2 UCA Imaging

Motion Correction: During the data acquisition, device motion resulting from pumping was observed mainly in the axial direction. Therefore, the motion correction algorithm stated in Section 3.4 was adopted to improve the TPI performance. One dimensional motion correction algorithm is derived from Equation 3.7 and is formed as:

$$\rho(i) = \frac{\sum_{i=1}^{M}(S_0(z) - \bar{S_0})(S_1(z+i) - \bar{S_1})}{\sqrt{\sum_{z=1}^{M}\left(S_0(z) - \bar{S_0}\right)^2 \sum_{z=1}^{M}\left(S_1(z+i) - \bar{S_1}\right)^2}}, \tag{7.1}$$

where the parameters stand for the same contents as those in Equation 3.7. One dimensional motion correction algorithm was only applied to the axial direction.

In the axial direction, the distance between two successive samples (one sample step size) was approximately 0.02mm. However, the axial displacements in this experiment were smaller than 0.02mm. Therefore, spline interpolation was employed before applying the motion correction algorithm to achieve better alignment. Figure 7.3 shows the plot of one RF lateral line with different frames. The left image is the one before motion correction and the right one is after the correction. One can tell the proper alignment was successfully achieved. Meanwhile, the lateral line in Figure 7.3 passed through the channel with UCA. The UCA activity was clearly observed between laterally -5mm and 5mm and from frames 90 to 150.

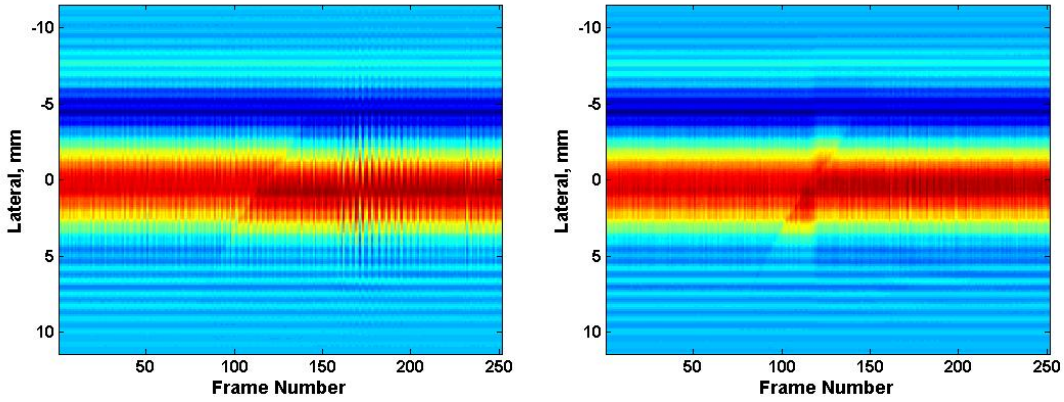

(a) Before Motion Correction (b) After Motion Correction

Figure 7.3: The images of one raw RF lateral line with different frames, before (left) and after (right) motion correction.

Temporal Perfusion Index: The TPI was applied to the data after the motion correction. Because of reverberation, nonlinear filtering was not employed. The dynamic range for TPI computation was determined as 15dB. Figure 7.4 shows multiple TPI frames overlaid on the B-mode images. One can see that microbubbles came from the right side at frame 91, gradually flowed through the channel, and disappeared from the left side at frame 150.

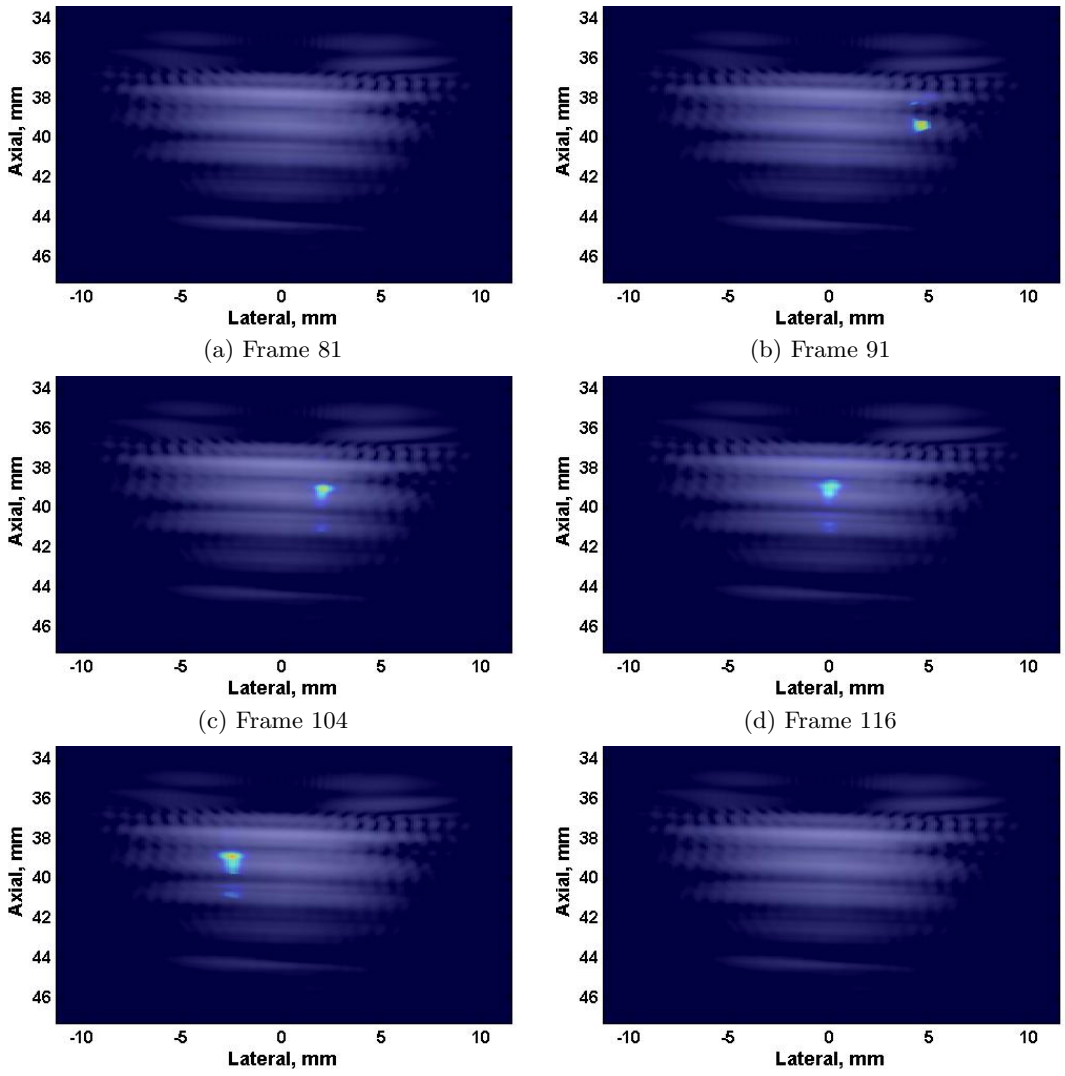

(a) Frame 81 (b) Frame 91

(c) Frame 104 (d) Frame 116

(e) Frame 131 (f) Frame 150

Figure 7.4: Six TPI images overlaid on standard B-mode images. The dynamic range for TPI computation was determined as 15dB.

The conclusions drawn from Figure 7.4 can be summarized as follows:

1. The TPI was able to capture and track the UCA activity within a 15μm microchannel, even with the presence of reverberation.

2. The channel location captured by the TPI was consistent with the tube location shown in the baseline B-mode image in Figure 7.2.

3. The light blue shade which was observed above and below the micro-channel in the images (Figure 7.4b to Figure 7.4e) was artifacts due to reverberation.

7.1.3 Discussion

The SCD research on contrast-enhanced ultrasound is still in its early stages. The preliminary results shown in this section provide the feasibility test of imaging UCA flow within a 15μm channel with the presence of reverberation. The suggestions for future research are proposed as follows:

1. Reverberation needs to be reduced or removed either by applying de-reverberation algorithms or using more-acoustically-absorbing materials. Strong reverberation resulted in artifacts in both B-mode and TPI images. Reducing reverberation will improve the imaging quality and specificity.

2. Apply nonlinear Volterra filters to improve the image resolution. Volterra filters were not applied to the current data set because of strong reverberation. If dereverberation is employed, Volterra filters should be applied afterwards to further improve the imaging specificity and sensitivity.

3. UCA solution should contain blood samples. In the experiments which have been done so far, the UCA microbubbles were dissolved in the water. To better mimic the SCD environment, blood samples should be used. This may bring in new challenges to the UCA microflow imaging.

4. Therapeutic ultrasound should be applied. In [75], a brief high-power destructive pulse sequence was used to activate the microbubbles to carry the blood cells for the purpose of SCD treatment. Therapeutic ultrasound is proposed to be adopted after the feasibility test of UCA microflow imaging with a blood sample.

Chapter 8

Conclusions and Future Studies

8.1 Conclusions

From the work presented in this dissertation, two main conclusions can be drawn. First, compared to other more widely used nonlinear methods such as pulse inversion (PI), the advantages of using the Volterra filter (VF) have been experimentally demonstrated in terms of improved spatial specificity and contrast-to-tissue ratio (CTR). Second, the temporal perfusion index (TPI) has been introduced and experimentally approved that it is capable of providing a qualitative measure of microbubble perfusion density by accounting for UCA dynamics due to pulsation and blood circulation.

Volterra Filters

The performance of the VF was first tested on *in vitro* UCA microflow within 200μm cellulose tube(s) embedded in tissue-mimicking phantoms. The results have demonstrated that the nonlinear VF components can achieve similar or higher levels of sensitivity and spatial specificity than multipulse methods such as PI. The longitudinal perfusion imaging results presented in the later section have shown that the VF has the sensitivity to heterogeneous UCA perfusion and different UCA events while PI is not able to achieve.

Later, the VF was applied to *in vivo* heterogeneous tumor perfusion imaging with a clinical linear probe. The results have established that the VF can provide an important tool for imaging UCA activity in regions with heterogeneous perfusion as is the case in some tumors and ischemic tissues.

Last but not least, the VF was applied to both *in vitro* and *in vivo* transcranial brain perfusion imaging, which is one of the most significant application in perfusion imaging. The results have once again approved that the VF processing is capable of improving imaging spatial specificity and contrast-to-tissue ratio (CTR).

Temporal Perfusion Index

The TPI was first tested on *in vitro* in tissue-mimicking phantoms with 200μm cellulose tube(s) embedded. The results have demonstrated that the TPI is capable of providing a qualitative measure of microbubble perfusion density, without or with the presence of high specular reflections from the channel walls. The TPI value reflects the microbubble perfusion density.

Later, the TPI was adopted to image heterogeneous tumor perfusion *in vivo*. The TPI is able to measure of microbubble perfusion density in both homogeneous and heterogeneous perfusion regions by accounting for different UCA events.

The TPI were also applied to both *in vitro* and *in vivo* transcranial brain perfusion imaging. For this application, the dual-mode ultrasound array (DMUA) and synthetic aperture (SA) imaging were adopted to provide uniform excitation with distortions present due to the skull. The TPI is able to enhance UCA activity with high spatial resolution due to the pixel-wise nature of the processing and also provide qualifications at heterogeneous perfusion regions. Moreover, motion-trigger TPI is capable of imaging brain perfusion with pronounced animal's breathing motion present, by determining the time interval of a breathing cycle to cancel out the breathing motion's effect.

The TPI was also employed to image perfusion within a 15 μm channel embedded in a micro-fluidic device which was used to mimic sickle cell disease (SCD) environment. The results proved that the TPI was able to track UCA perfusion in the micro-channel. The potential of providing imaging and treatment for SCD will be further investigated in future studies.

Summary

Collectively, both *in vitro* and *in vivo* results have demonstrated that the VF can achieve high sensitivity and specificity to both homogeneous and heterogeneous perfusion imaging and the TPI is able to provide a qualitative measure of microbubble perfusion density.

8.2 Future Studies

8.2.1 DMUA Focal Zone Denoising

The *in vitro* results from Chapter 6 have revealed artifacts near the geometric center of the transducer. This type of artifact results from the electronic noise due to the power supply switching. The noise is time-varying nonstationary and appears highest around the geometric center. The variance pattern of the noise is shown in Figure 8.1. The data were acquired in the degassed deionized water with no imaging target present.

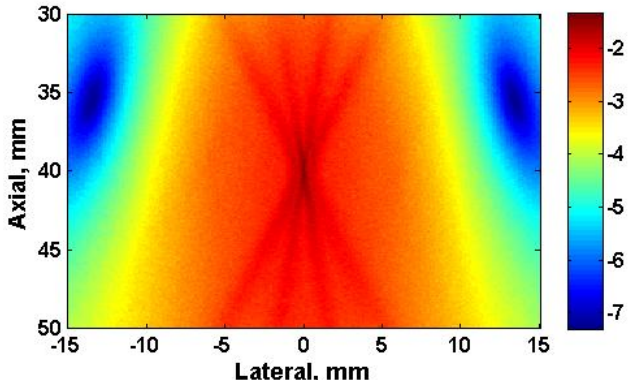

Figure 8.1: The variance of the DMUA noise over 251 frames.

Denoising using Pre-beamformed Data: The DMUA focal zone denoising may be achieved using pre-beamformed data. One frame of pre-beamformed data acquired with a wire target in the focal zone is shown in Figure 8.2. The image is displayed using log-compression. The strong signals in the center of the image resulted from the wire target and exhibited high repeatability among the different transmit elements.

Except for the signal reflected from the wire target, the spikes corresponding to the

noise in the focal zone were sparsely distributed in the pre-beamformed data with a certain pattern which was highlighted using the white circle at the lower left corner of the image. The spikes were highly correlated between the receive elements 1 to 8 and 17 to 24, and also between the elements 9 to 16 and 25 to 32.

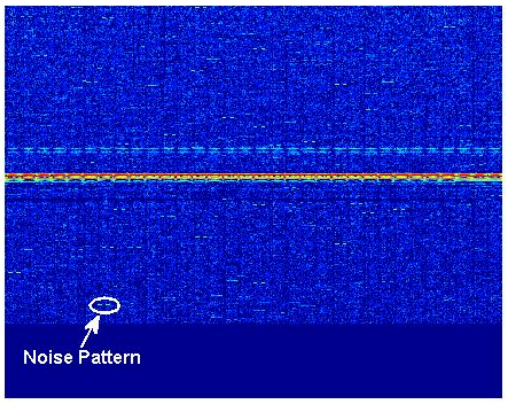

Figure 8.2: One frame of pre-beamformed data acquired with a wire target in the geometric focus of the DMUA.

Theoretically, denoising methods can be applied to remove the spikes in order to improve the SNR in the focal zone. However, the main difficulties in implementing denoising methods are: the random and sparse distribution of spikes and their time-varying nature, and the correlations between different array elements. How to properly remove the spikes to improve SNR and perfusion imaging performance will be further investigated in the future studies.

8.2.2 Tissue VF AND UCA VF

In Section 2.4, it was stated that a VF is not necessarily derived from the UCA data; it can also be derived from tissue-only data due to the existence of tissue nonlinearity resulting from nonlinear distortion from the clinical transducer [48]. A combination of UCA TVF and tissue TVF may provide an opportunity to better separate tissue and UCA nonlinearities.

In Section 2.4.1, the difference of the power of the UCA signal using outputs from different UCA TVFs and tissue TVFs was presented. Figure 8.3 shows spectrograms

of quadratic components from Figure 2.2. One can tell that both UCA and tissue TVFs were capable of capturing UCA nonlinearity. However, the quadratic components derived using the UCA filter exhibited the highest value and widest bandwidth of UCA nonlinearity when compared to those from tissue filters. On the other hand, the quadratic components derived using tissue filters focused on different frequency bands. The CTR ratio may even be higher at a certain frequency band such as between 5 - 7 MHz for the quadratic components derived from tissue TVFs.

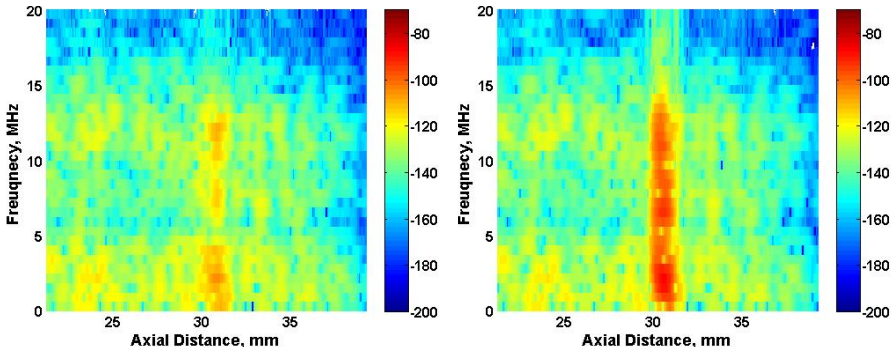

(a) Quadratic w/o UCA, U-TVF (b) Quadratic w/ UCA, U-TVF

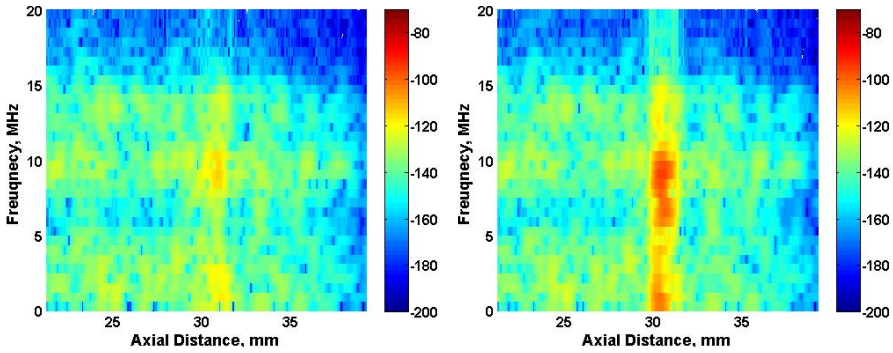

(c) Quadratic w/o UCA, T1-TVF (d) Quadratic w/ UCA, T1-TVF

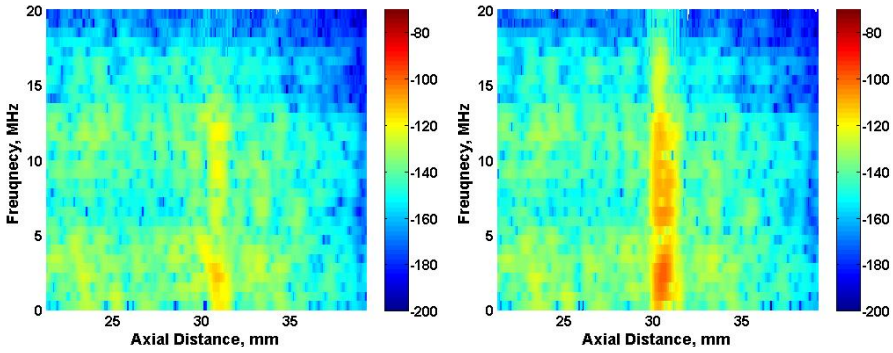

(e) Quadratic w/o UCA, T2-TVF (f) Quadratic w/ UCA, T2-TVF

Figure 8.3: Spectrograms of the A-line through the cellulose channel while pumping saline (left) and UCA (right). The spectrograms were plotted with quadratic components derived using the UCA filter and tissue filters from Figure 2.2.

A combination of the outputs of tissue filters and UCA filters may be able to achieve higher contrast-to-tissue ratio. A diagram of a proposed combination is shown in Figure 8.4 for future studies.

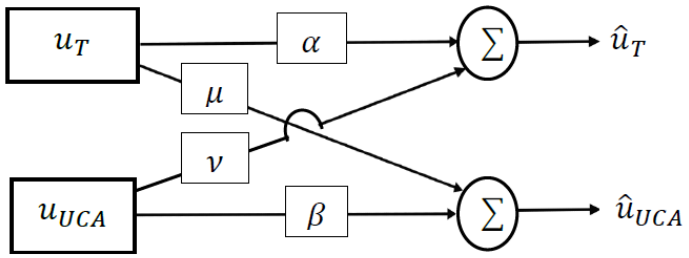

Figure 8.4: A proposed implementation by combining a tissue TVF and UCA TVF.

8.2.3 Global TPI and Localized TPI

As stated in Sections 5.1.4, different dynamic ranges and values of γ can benefit different high/low/none perfused regions. Generally speaking, small dynamic range and γ reward high-echogenicity perfused regions and reduce artifacts from noise, while large dynamic range and γ reward low-echogenicity perfused regions and suppress the animal's breathing motion effect. The results presented in this dissertation were computed using a global dynamic range and γ. However, to maximize perfusion imaging performance and minimize the artifacts from noise and animal's motion, localized dynamic range and γ are recommended for future studies. Their value should be partially determined by the local echogenicity.

8.2.4 Incoherent SA Beamforming with DMUA

All DMUA data in this dissertation were beamformed coherently using Equation 1.3. However, it may be beneficial to beamformed DMUA data incoherently, due to the inconsistent UCA nonlinearity captured within a single pre-beamformed frame. Simple coherent SA beamform may lose information on UCA nonlinearity. Studies need to be done to improve the beamforming method by accounting for incoherency.

References

[1] John A. Detre, John S. Leigh, Donald S. Williams, and Alan P. Koretsky. Perfusion imaging. *Journal of Magnetic Resonance in Medicine*, 23:37–45, 1992.

[2] Paul G. Krause, Ahmed H. Tewfik, and James F. Greenleaf. Detection of blood perfusion. *International Conference on Image Processing*, 2:192–196, 1999.

[3] Song Hu and Lihong V. Wang. Photoacoustic imaging and characterization of the microvasculature. *Journal of Biomedical Optics*, 15(1):011101, 2010.

[4] H.N. Wagner Jr., B.A. Rhodes, Y. Sasaki, and J.P. Ryan. Studies of the circulation with radioactive microspheres. *Journal of Investigative Radiology*, 4:374–386, 1969.

[5] D. Norman, L. Axel, W.H. Berninger, M.S. Edwards, C.E. Cann, R.W. Redington, and L. Cox. Dynamic computed tomography of the brain: Techniques, data analysis, and applications. *American Journal of Roentgenology*, 136(4):759–770, 1981.

[6] K. A. Miles, M. Hayball, and A. K. Dixon. Colour perfusion imaging: A new application of computed tomography. *The Lancet*, 337(8742):643–645, 1991.

[7] Matthias Koenig, Ernst Klotz, Barbara Luka, Derk J. Venderink, Johann F. Spittler, and Lothar Heuser. Perfusion CT of the brain: Diagnostic approach for early detection of ischemic stroke. *Journal of Radiology*, 209(1):85–93, 1998.

[8] A. A. Konstasa, G. V. Goldmakhera, T.-Y. Leeb, and M. H. Leva. Theoretic basis and technical implementations of CT perfusion in acute ischemic stroke, part 1: Theoretic basis. *American Journal of Neuroradiology*, 30(5):662–668, 2009.

[9] Jeffrey R. Petrella and James M. Provenzale. MR perfusion imaging of the brain: Techniques and applications. *American Journal of Roentgenology*, 175(1):207–219, 2000.

[10] Marco Essig, Mark S. Shiroishi, Thanh Binh Nguyen, Marc Saake, James M. Provenzale, David Enterline, Nicoletta Anzalone, Arnd Drfler, lex Rovira, Max Wintermark, and Meng Law. Perfusion MRI: The five most frequently asked technical questions. *American Journal of Roentgenology*, 200(1):24–34, 2013.

[11] David C. Alsop, John A. Detre, Xavier Golay, Matthias GUunther, Jeroen Hendrikse, Luis Hernandez-Garcia, Hanzhang Lu, Bradley J. MacIntosh, Laura M. Parkes, Marion Smits, Matthias J.P. van Osch, Danny J.J. Wang, Eric C. Wong, and Greg Zaharchuk. Recommended implementation of arterial spin-labeled perfusion MRI for clinical applications: A consensus of the ISMRM perfusion study group and the European consortium for ASL in dementia. *Journal of Magnetic Resonance in Medicine*, 73:102–116, 2015.

[12] Telli Faez, Marcia Emmer, Klazina Kooiman, Michel Versluis, Antonius van der Steen, and Nico de Jong. 20 years of ultrasound contrast agent modeling. *IEEE Trans Ultrason Ferroelectr Freq Control*, 60(1):7–20, Jan 2013.

[13] Peter N. Burns and Stephanie R. Wilson. Microbubble contrast for radiological imaging: 1. principles. *Ultrasound Q*, 22(1):5–13, Mar 2006.

[14] Xinghua Wang, Hai-Dong Liang, Baowei Dong, Qi-Long Lu, and Martin J K. Blomley. Gene transfer with microbubble ultrasound and plasmid DNA into skeletal muscle of mice: comparison between commercially available microbubble contrast agents. *Radiology*, 237(1):224–229, Oct 2005.

[15] Joo Ha Hwang, Andrew A. Brayman, Michael A. Reidy, Thomas J. Matula, Michael B. Kimmey, and Lawrence A. Crum. Vascular effects induced by combined 1-mhz ultrasound and microbubble contrast agent treatments in vivo. *Ultrasound Med Biol*, 31(4):553–564, Apr 2005.

[16] J. R. Eisenbrey, O Mualem Burstein, R. Kambhampati, F. Forsberg, J-B. Liu, and M. A. Wheatley. Development and optimization of a doxorubicin loaded

poly(lactic acid) contrast agent for ultrasound directed drug delivery. *J Control Release*, 143(1):38–44, Apr 2010.

[17] Ross Williams, John M. Hudson, Brendan A. Lloyd, Ahthavan R. Sureshkumar, Gordon Lueck, Laurent Milot, Mostafa Atri, Georg A. Bjarnason, and Peter N. Burns. Dynamic microbubble contrast-enhanced US to measure tumor response to targeted therapy: a proposed clinical protocol with results from renal cell carcinoma patients receiving antiangiogenic therapy. *Radiology*, 260(2):581–590, Aug 2011.

[18] Christopher R. Anderson, Xiaowen Hu, Hua Zhang, Jose Tlaxca, Anne-Emilie Decleves, Robert Houghtaling, Kumar Sharma, Michael Lawrence, Katherine W. Ferrara, and Joshua J. Rychak. Ultrasound molecular imaging of tumor angiogenesis with an integrin targeted microbubble contrast agent. *Invest Radiol*, 46(4):215–224, Apr 2011.

[19] J.R. Lindner. Microbubbles in medical imaging: current applications and future directions. *Nature Review: Drug Discovery*, 3(6):527–532, 2004.

[20] T.G. Leighton. *The Acoustic Bubble*. Academic Press, 1994.

[21] Karen E. Morgan, John S. Allen, Paul A. Dayton, James E. Chomas, Alexander L. Klibanov, and Katherine W. Ferrara. Experimental and theoretical evaluation of microbubble behavior: Effect of transmitted phase and bubble size. *IEEE Transactions on Ultrasonics, Ferroelectrics, and Frequency Control*, 47(6):14941509, 2000.

[22] Pornchai Phukpattaranont. *Quadratic B-mode(QB-mode) Ultrasounic Imaging: A New Method for Imaging Quadratic Signal Components*. PhD thesis, University of Minnesota, Minneapolis, MN, USA, Oct. 2004.

[23] Barry B. Goldberg, Ji-Bin Liu, and Flemming Forsberg. Ultrasound contrast agents: A review. *Ultrasound in Medicine and Biology*, 20(4):319–333, 1994.

[24] V. Uhlendorf. Physics of ultrasound contrast imaging: scattering in the linear range. *Ultrasonics, Ferroelectrics, and Frequency Control, IEEE Transactions on*, 14(1):70–79, Jan. 1994.

[25] P.A Dijkmans, L.J.M Juffermans, R.J.P Musters, A. van Wamel, F.J. ten Cate, W. van Gilst, C.A Visser, N. de Jong, and O. Kamp. Microbubbles and ultrasound: from diagnosis to therapy. *European Heart Journal, Cardiovascular Imaging*, 5(4):245–256, Aug. 2004.

[26] B. Haider and R.Y. Chiao. Higher order nonlinear ultrasonic imaging. *IEEE Ultrasonics Symposium Proceedings*, 2:1527–1531, Oct. 1999.

[27] F. Forsberg, W. T. Shi, and B. B. Goldberg. Subharmonic imaging of contrast agents. *Ultrasonics*, 38:93–98, Mar. 2000.

[28] E. Stride and N. Saffari. Microbubble ultrasound contrast agents: a review. *Proc Inst Mech Eng H*, 217(6):429–447, 2003.

[29] Verya Daeichin, Johan G. Bosch, Andrew Needles, F Stuart Foster, Antonius van der Steen, and Nico de Jong. Subharmonic, non-linear fundamental and ultraharmonic imaging of microbubble contrast at high frequencies. *Ultrasound Med Biol*, 41(2):486–497, Feb 2015.

[30] G. Brock-Fisher, M. Poland, and P. Rafter. Means for increasing sensitivity in nonlinear ultrasound imaging systems. *The Journal of the Acoustical Society of America*, Jan. 1997.

[31] D. H. Simpson, C. T. Chin, and P. N. Burns. Pulse inversion doppler: a new method for detecting nonlinear echoes from microbubble contrast agents. *IEEE Trans Ultrason Ferroelectr Freq Control*, 46(2):372–382, 1999.

[32] Robert J. Eckersley, Chien Ting Chin, and Peter N. Burns. Optimising phase and amplitude modulation schemes for imaging microbubble contrast agents at low acoustic power. *Ultrasound Med Biol*, 31(2):213–219, Feb 2005.

[33] Charles Tremblay-Darveau, Ross Williams, Laurent Milot, Matthew Bruce, and Peter N. Burns. Combined perfusion and doppler imaging using plane-wave nonlinear detection and microbubble contrast agents. *IEEE Trans Ultrason Ferroelectr Freq Control*, 61(12):1988–2000, Dec 2014.

[34] Juan Du, Dalong Liu, and Emad Ebbini. Nonlinear imaging of microbubble contrast agent using the Volterra filter: In vivo results. 2016.

[35] Johan Kirkhorn, Sigmund Frigstadt, and Hans Top. Comparison of pulse inversion and second harmonic for ultrasound contrast imaging. *IEEE Internatioal Ultrasound Symposium*, 2:1897–1901, 2000.

[36] Pornchai Phukpattaranont, Mamoun F. Al-Mistarihi, and Emad S. Ebbini. Post-beamforming Volterra filters for contrast-assisted ultrasonic imaging: In-vivo results. *IEEE Internatioal Ultrasound Symposium*, 2:1191–1194, 2003.

[37] B.D. Van Veen and K.M. Buckley. Beamforming: A versatile approach to spatial filtering. *IEEE ASSP Magazine*, 5(2):4 – 24, 1988.

[38] E.S. Ebbini, H. Yao, and A. Shrestha. Dual-mode ultrasound phased arrays for image-guided surgery. *Ultrasonic Imaging*, 28(2):65–82, 2006.

[39] Andrew J. Casper, Dalong Liu, John R. Ballard, and Emad S. Ebbini. Real-time implementation of a dual-mode ultrasound arrays system: *In vivo* results. *IEEE Transcations on Biomendical Engineering*, 60(10):2751–2759, 2013.

[40] Pornchai Phukpattaranont and Emad S. Ebbini. Post-beamforming second-order volterra filter for pulse-echo ultrasonic imaging. *IEEE Trans Ultrason Ferroelectr Freq Control*, 50(8):987–1001, Aug 2003.

[41] T. Koh and E.J. Powers. Second-order Volterra filtering and its application to nonlinear system identification. *Acoustics, Speech and Signal Processing, IEEE Transactions on*, 33(6):1445–1455, Dec 1985.

[42] G.L. Sicuranza. Quadratic filters for signal processing. *Proceedings of the IEEE*, 80(8):1263–1285, Aug 1992.

[43] Davide Mattera and Luigi Paura. Exploitation of cyclostationarity for identifying nonlinear volterra systems by input-output noisy measurements. In *Conference Record of the Thirtieth Asilomar on Signals, Systems and Computers*, volume 1, pages 166–170, Nov 1996.

[44] M. B. Meenavathi and K. Rajesh. Volterra filtering techniques for removal of Gaussian and mixed Gaussian-impulse noise. *International Journal of Electrical, Computer, Energetic, Electronic and Communication Engineering*, 1(2):176–182, 2007.

[45] M. F. Al-Mistarihi, Pornchai Phukpattaranont, and E.S. Ebbini. Post-beamforming third-order Volterra filter (ThOVF) for pulse-echo ultrasonic imaging. In *Acoustics, Speech, and Signal Processing, 2004. Proceedings. (ICASSP '04). IEEE International Conference on*, volume 3, pages iii–97–100 vol.3, May 2004.

[46] Simon O. Haykin. *Adaptive Filter Theory.* Prentice Hall, fourth edition, Jan. 2001.

[47] M. Mischi, N.G. Rognin, and M.A. Averkiou. Ultrasound imaging modalities. *Reference Module in Biomedical Sciences: Comprehensive Biomedical Physics*, 2:361–385, 2014.

[48] M.A. Averkiou, D.N. Roundhill, and J.E. Powers. A new imaging technique based on the nonlinear properties of tissues. *IEEE Ultrasonics Symposium*, 2:1561–1566, 1997.

[49] William T. Shi and Flemming Forsberg. Ultrasonic characterization of the nonlinear propoerties of contrast microbubbles. *Ultrasound in Medicine and Biology*, 26(1):93–104, 2000.

[50] Yayun Wan, R. Visaria, J.C. Bischof, and E.S. Ebbini. Quadratic B-mode and pulse inversion imaging of perfusion defects in vivo. In *Life Science Systems and Applications Workshop, 2007. LISA 2007. IEEE/NIH*, pages 237–240, Nov 2007.

[51] Torsten Mller Hamid Younesy and Hamish Carr. Visualization of time-varying volumetric data using differential time-histogram table. *Fourth International Workshop on Volume Graphics*, pages 21–29, 2005.

[52] K.R. Nightingale, M.L. Palmeri, R.W. Nightingale, and G.E. Trahey. On the feasibility of remote palpation using acoustic radiation force. *J Acoust Soc Am*, 110(1):625–634, Jul 2001.

[53] R. F. Wagner, M. F. Insana, and S. W. Smith. Fundamental correlation lengths of coherent speckle in medical ultrasonic images. *IEEE Trans Ultrason Ferroelectr Freq Control*, 35(1):34–44, 1988.

[54] Alan V. Oppenheim and Ronald W. Schafer. *Discrete-time Signal Processing*. Prentice Hall, 2010.

[55] G.M. Tozer. Measuring tumour vascular response to antivascular and antiangiogenic drugs. *The British Institute of Radiology*, 76:S23–35, 2003.

[56] Luigi Solbiati, Tiziana Ierace, Massimo Tonolini, and Luca Cova. Guidance and monitoring of radiofrequency liver tumor ablation with contrast-enhanced ultrasound. *Journal of the American College of Cardiology*, 51S:S19–23, 2004.

[57] G.T. Clement and K. Hynynen. A noninvasive method for focusing ultrasound through the human skull. *Physics in Medicine and Biology*, 47(8):1219–1236, 2002.

[58] G.T. Clement. Perspectives in clinical uses of high-intensity focused ultrasound. *Ultrasonics*, 42(10):1087–1093, 2004.

[59] William J. Tyler. Noninvasive neuromodulation with ultrasound? A continuum mechanics hypothesis. *The Neuroscientist*, 17(1):25–36, 2011.

[60] G.N. Hounsfield. Computerized transverse axial scanning (tomography): Part I. description of system. *The British Institute of Radiology*, 46(552):1016–1022, 1973.

[61] J. Ambrose. Computerized transverse axial scanning (tomography): Part II. clinical application. *The British Institute of Radiology*, 46:1023–1047, 1973.

[62] R.S. Frackowiak, G.L. Lenzi, and J.D. Heather T. Jones. Quantitative measurement of regional cerebral blood flow and oxygen metabolism in man using ^{15}O and positron emission tomography: Theory, procedure, and normal values. *Journal of Computer Assisted Tomography*, 4(6):727–736, 1980.

[63] F. Sakai, K. Nakazawa, Y. Tazaki, K. Ishii, H. Hino, H. Igarashi, and T. Kanda. Regional cerebral blood volume and hematocrit measured in normal human volunteers by single-photon emission computed tomography. *Journal of Cerebral Blood Flow and Metabolism*, 5(2):207–213, 1985.

[64] F.F. Jbsis. Noninvasive, infrared monitoring of cerebral and myocardial oxygen sufficiency and circulatory parameters. *American Association for the Advancement of Science*, 198(4323):1264–1267, 1977.

[65] Elizabeth M.C. Hillman. Optical brain imaging in vivo: Techniques and applications from animal to man. *Journal of Biomedical Optics*, 12, 2007.

[66] Ali Yousefi, David E. Goertz, and Kullervo Hynynen. Transcranial shear-mode ultrasound: Assessment of imaging performance and excitation techniques. *IEEE Transcations on Medical Imaging*, 28(5):763–774, 2009.

[67] Thomas Deffieux and Elisa E. Konofagou. Numerical study of a simple transcranial focused ultrasound system applied to blood-brain barrier opening. *IEEE Transactions on Ultrasonics, Ferroelectrics, and Frequency Control*, 57(12):2637–2653, 2010.

[68] Brooks D. Lindsey, Edward D. Light, Heather A. Nicoletto, Ellen R. Bennett, Daniel T. Laskowitz, and Stephen W. Smith. The ultrasound brain helmet: New transducers and volume registration for in vivo simultaneous multi-transducer 3-D transcranial imaging. *IEEE Transactions on Ultrasonics, Ferroelectrics, and Frequency Control*, 58(6):1189–1202, 2011.

[69] E. Mace, G. Montaldo, B.F. Osmanski, I. Cohen, M. Fink, and M. Tanter. Functional ultrasound imaging of the brain: Theory and basic principles. *IEEE Transcations on Ultrasonics, Ferroelctrics and Frequency Control*, 60(3):492–506, 2013.

[70] Alyona Haritonova, Dalong Liu, and Emad S. Ebbini. In vivo application and localization of rranscranial focused ultrasound using dual-mode ultrasound arrays. *IEEE Transactions on Ultrasonics, Ferroelectrics, and Frequency Control*, 62(12):20312042, 2015.

[71] Jerome M.G. Borsboom, Chien Ting Chin, Ayache Bouakaz, Michel Versluis, and Nico de Jong. Harmonic chirp imaging method for ultrasound contrast agent. *IEEE Transactions on Ultrasonics, Ferroelectrics and Frequency Control*, 52(2):241–249, 2005.

[72] David K. Wood, Alicia Soriano, L. Mahadevan, John M. Higgins, and Sangeeta N. Bhatia. A biophysical marker of severity in sickle cell disease. *Science Translational Medicine*, 4(123):93–104, 2012.

[73] Barbara P. Yawn, George R. Buchanan, Araba N. Afenyi-Annan, Samir K. Ballas, Kathryn L. Hassell, Andra H. James, Lanetta Jordan, Sophie M. Lanzkron, Richard Lottenberg, William J. Savage, Paula J. Tanabe, Russell E. Ware, M. Hassan Murad, Jonathan C. Goldsmith, Eduardo Ortiz, Robinson Fulwood, Ann Horton, and Joylene John-Sowah. Management of sickle cell disease: Summary of the 2014 evidence-based report by expert panel members. *Journal of the American Medical Association*, 312(10):1033–1048, 2014.

[74] J.T. Lindner, M. Widlansky, M.D. Wu, J. Dargatz, L.M. Harmann, T. Belcik, D.S. Neuberg, D.G. Nathan, J. Linden, and J.J. Field. Contrast-enhanced ultrasound detects differences in microvascular blood flow in adults with sickle cell disease administered regadenoson. *Journal of the American Society of Echocardiography*, 124, 2014.

[75] Melinda D. Wu, J. Todd Belcik, Yue Qi, Yan Zhao, Cameron Benner, Hong Pei, Joel Linden, and Jonathan R. Lindner. Abnormal regulation of microvascular tone in a murine model of sickle cell disease assessed by contrast ultrasound. *Journal of the American Society of Echocardiography*, 28(9):1122–1128, 2015.

[76] M. Wu, J.T. Belcilt, Y. Oi, H. Pei, Y. Zhao, J. Linden, and J. Lindner. Contrast enhanced ultrasound imaging to detect abnormaloties of microvascular blood flow in murine models of sickle cell disease. *Pediatric Blood and Cancer*, 62(S2):54–54, 2015.

Appendix A

Acronyms

Table A.1: Acronyms

Acronym	Meaning
CEUS	Contrast-enhanced Ultrasound
UCA	Ultrasound Contrast Agent
TVF	Third-order Volterra Filter
TPI	Temporal Perfusion Index
MI	Mechanical Index
DMUA	Dual-mode Ultrasound Array
SA	Synthetic Aperture
RLS	Recursive Least Squares
RF	Radio Frequency
PDF	Probability Distribution Function
LB-mode	Linear B-mode
QB-mode	Quadratic B-mode
CB-mode	Cubic B-mode
LM-mode	Linear M-mode
QM-mode	Quadratic M-mode
CM-mode	Cubic M-mode

Continued on next page

Table A.1 – continued from previous page

Acronym	Meaning
fps	Frame per Second
SVF-QK	Second-order Volterra Filter Quadratic Kernels
TVF-QK	Third-order Volterra Filter Quadratic Kernels
SD	Standard Derivation
tFUS	Transcranial Focused Ultrasound
SCD	Sickle Cell Disease